



Chemistry modeling and inverse reconstruction of emissions with a Lagrangian transport model

Dissertation

submitted in fulfilment of the requirements
for the degree of Doctor of Natural Science (Dr. rer. nat.)

by
Mingzhao Liu

in October, 2024

at
the Faculty of Mathematics and Natural Science
of the University of Wuppertal

Zusammenfassung

Die genaue Simulation der Ausbreitung von Spurengasen in der Atmosphäre ist sowohl für die Klimaforschung als auch für praktische Anwendungen von entscheidender Bedeutung, z. B. für die Vorhersage der Auswirkungen von Vulkanausbrüchen, Waldbränden und industriellen Verschmutzungen auf Umwelt und Gesundheit. Diese Arbeit konzentriert sich auf die Weiterentwicklung des Lagrange'schen Ausbreitungsmodells MPTRAC (Massive-Parallel Trajectory Calculations) zur genauen Simulation des Transports und der chemischen Umwandlung reaktiver Spurengase in der Atmosphäre. Die Arbeit entwickelt und implementiert chemische Schemata in das Lagrange-Transportmodell MPTRAC, um die Genauigkeit der Simulation dieser Prozesse zu verbessern.

Eine der größten Herausforderungen bei der Lagrangeschen Modellierung des chemischen Transports ist die genaue Darstellung der Quellen und Senken von Schadstoffen. Ein wichtiger Teil dieser Arbeit umfasst die Entwicklung sowohl expliziter als auch impliziter chemischer Schemata innerhalb des MPTRAC-Modells. Das explizite chemische Schema behandelt Reaktionen erster Ordnung, was es für groß angelegte Langzeitsimulationen rechnerisch effizient macht, während das implizite chemische Schema komplexe nichtlineare chemische Mechanismen mit flexiblen Benutzerdefinitionen behandelt. Darüber hinaus wird ein einfaches Mischungsschema implementiert und durch Hinzufügen eines Relaxationsterms getestet.

Das explizite Schema wird verwendet, um langlebige Tracer wie Distickstoffoxid (N_2O), FCKW-11 und FCKW-12 zu simulieren, die für Studien zum Klimawandel und Ozonabbau (O_3) entscheidend sind. In diesem Zusammenhang wird eine Fallstudie durchgeführt, um die Fähigkeit des Modells zu bewerten, die globale Verteilung und den Transport dieser langlebigen Tracer über einen mehrjährigen Zeitraum genau zu simulieren. Die Ergebnisse werden anhand von Satellitenbeobachtungen validiert. Der Vergleich zeigt, dass das MPTRAC-Modell, ausgestattet mit den neuen Chemie- und Mischungsschemata, die beobachteten globalen Muster dieser Tracer effektiv reproduzieren kann.

Darüber hinaus konzentriert sich die Arbeit auf die komplexen chemischen Wechselwirkungen, die beim vulkanischen Transport und Abbau von SO_2 beteiligt sind, vor allem durch die Oxidation mit Hydroxylradikalen (OH) in der Gasphase und Wasserstoffperoxid (H_2O_2) in der wässrigen Phase sowie durch feuchte Deposition. Diese Arbeit umfasst Fallstudien zu zwei großen Vulkanausbrüchen – dem Ambae-Ausbruch 2018 und dem Raikoke-Ausbruch 2019 – um die entwickelten Modelle zu validieren. Der Ambae-Ausbruch, der in der tropischen Region stattfand, injizierte große Mengen an SO_2 in die obere Troposphäre und die untere Stratosphäre (UT/LS), was zu einer erheblichen Oxidation in der Flüssigphase und feuchter Deposition führte. Im Gegensatz dazu wies der Raikoke-Ausbruch in den mittleren Breiten eine längere Lebensdauer von SO_2 auf, wobei Verluste hauptsächlich durch chemische Reaktionen in der Gasphase verursacht wurden. Durch die Analyse der Empfindlichkeit dieser Prozesse gegenüber verschiedenen meteorologischen und chemischen Faktoren liefert die Arbeit Einblicke in die Variabilität der SO_2 -Lebensdauer in verschiedenen Höhenlagen und atmosphärischen Bedingungen. Es werden sowohl explizite als auch implizite chemische Schemata getestet und durch Vergleich mit Satellitenmessungen bewertet. Die Ergebnisse zeigen auch, dass der vulkanische SO_2 -Zerfall einen starken nichtlinearen Effekt hat.

Um die Fähigkeit des Modells zur Schätzung vulkanischer SO_2 -Emissionen weiter zu verbessern, wird in dieser Arbeit ein inverser Modellierungsansatz unter Verwendung eines Partikelfilter-Algorithmus entwickelt, der den nichtlinearen Zerfall von SO_2 berücksichtigt und eine genauere Schätzung der Emissionsquellen im Vergleich zu herkömmlichen Rückwärts-Trajektorien-Methoden ermöglicht. Durch die Kopplung der inversen Modellierungstechnik mit den entwickelten chemischen Schemata verbessert die Arbeit die Fähigkeit, die zeit- und höhenaufgelösten Quellenparameter von Vulkanausbrüchen zu schätzen. In dieser Arbeit wird auch der Einfluss der Senkenmodellierung auf die rekonstruierten Emissionen untersucht, was zeigt, wie wichtig eine genaue Senkenmodellierung für die Quellenabschätzung ist.

Abstract

Accurate simulation of atmospheric pollutant dispersion is critical for both climate research and practical applications, such as predicting the environmental and health impacts of volcanic eruptions, wildfires, and industrial pollution events. This thesis focuses on the further development of the Lagrangian dispersion model MPTRAC (Massive-Parallel Trajectory Calculations) to accurately simulate the transport and chemical transformation of reactive trace gases in the atmosphere. The research develops and implements chemistry schemes in MPTRAC to improve the accuracy of the simulation of these processes.

One of the major challenges in Lagrangian chemical transport modeling is the accurate representation of the pollutant sources and sinks. An important part of this work involves the development of both explicit and implicit chemistry schemes within the MPTRAC model. The explicit chemistry scheme handles first-order reactions, making it computationally efficient for large-scale, long-term simulations, while the implicit chemistry scheme handles complex non-linear chemical mechanisms with flexible user definitions. In addition, a simple mixing scheme is implemented and tested by adding a relaxation term.

The explicit scheme is used to simulate long-lived tracers such as nitrous oxide (N_2O), CFC-11, and CFC-12, which are critical for climate change and ozone (O_3) depletion studies. In this context, a case study is conducted to evaluate the ability of the model to accurately simulate the global distribution and transport of these long-lived tracers over a multi-year period. The results are validated against satellite observations. The comparison shows that the MPTRAC model, equipped with the new chemistry and mixing schemes, can effectively reproduce the observed global patterns of these tracers.

In addition, the thesis focuses on the complex chemical interactions involved in volcanic SO_2 transport and depletion, primarily through oxidation with hydroxyl radicals (OH) in the gas phase and hydrogen peroxide (H_2O_2) in the aqueous phase, as well as wet deposition. This work includes case studies of two major volcanic eruptions—the 2018

Ambae eruption and the 2019 Raikoke eruption to validate the developed models. The Ambae eruption, situated in the tropical region, injected large amounts of SO₂ into the upper troposphere and lower stratosphere (UT/LS), resulting in significant cloud phase oxidation and wet deposition. In contrast, the Raikoke eruption in the mid-latitudes showed a longer SO₂ lifetime, mainly driven by gas-phase chemical reactions. By analyzing the sensitivity of these processes to various meteorological and chemical factors, the thesis provides insights into the variability of the SO₂ lifetime across different altitudes and atmospheric conditions. Both explicit and implicit chemistry schemes are tested and evaluated through comparison with satellite retrievals. The results also show that the volcanic SO₂ decay has a strong non-linear effect.

To further improve the ability of the model to estimate volcanic SO₂ emissions, this thesis develops an inverse modeling approach using a particle filter algorithm, that accounts for the non-linear decay of SO₂ and provides a more accurate estimation of emission sources compared to traditional backward trajectory methods. By coupling the inverse modeling technique with the developed chemistry schemes, the work enhances the ability to estimate the time and altitude-resolved source parameters of volcanic eruptions. This thesis also examines the influence of the sink modeling on the reconstructed emissions, demonstrating the importance of the accurate sink modeling for source estimation.

Contents

1	Introduction	1
1.1	Lagrangian chemical transport modeling	3
1.2	Volcanic sulfur dioxide transport modeling	7
1.3	Inverse modeling on atmospheric source reconstruction	9
1.4	Structure of the thesis	13
2	Lagrangian chemical transport modeling	17
2.1	Overview on the MPTRAC model	17
2.2	Exponential decay processes	19
2.2.1	Wet deposition	19
2.2.2	Hydroxyl radical oxidation in the gas phase	21
2.2.3	Hydrogen peroxide oxidation in the aqueous phase	23
2.2.4	Long-lived tracer chemistry	23
2.3	Implicit chemistry scheme	24
2.4	Inter-parcel mixing algorithm	27
3	Case study of long-lived tracers	28
3.1	Data and method	29
3.1.1	Lagrangian chemical transport simulations of long-lived tracers	29
3.1.2	ECMWF reanalysis	29
3.1.3	SPARC Data Initiative	30
3.1.4	MIPAS satellite observations	30
3.1.5	Model initialization and setup	30

3.2	Results	31
3.2.1	Sensitivity of meteorological data	31
3.2.2	Evaluation of the photolysis data	32
3.2.3	Sensitivity on mixing parameters	32
3.2.4	Model results across different potential temperatures	36
3.3	Discussion	40
4	Case study of Ambae eruption	41
4.1	Data and Method	41
4.1.1	Lagrangian transport of volcanic sulfur dioxide plume	41
4.1.2	AIRS sulfur dioxide index	42
4.1.3	TROPOMI SO ₂ measurements	42
4.2	Results	43
4.2.1	Baseline simulation	43
4.2.2	Sensitivity test on SO ₂ release height	46
4.2.3	Sensitivity tests on OH chemistry	48
4.2.4	Sensitivity tests on wet deposition	51
4.2.5	Impact of the extreme convection parameterization	52
4.3	Discussion	53
5	Case study of Raikoke eruption	56
5.1	Model initialization	57
5.2	Results	58
5.2.1	Sulfur dioxide chemical lifetime analysis	58
5.2.2	Correction for the simplified explicit scheme	61
5.2.3	Evaluation of the simulated OH field	63
5.2.4	Selection of the chemistry time step	64
5.2.5	Assessment of computational costs	66
5.3	Discussion	67

6 Inverse source estimation with a particle filter	70
6.1 Particle filter algorithm	71
6.2 Ambae case study	74
6.2.1 Simulation setup	74
6.2.2 Particle filter versus backward trajectory method	74
6.2.3 Sensitivity of reconstructed emissions to sink modeling	78
6.3 Raikoke case study	78
6.3.1 Simulation setup	78
6.3.2 Results	80
6.4 Discussion	83
7 Summary	85
A Validation of OH fields with diurnal variability	87
List of figures	87
List of tables	95
Bibliography	96

Chapter 1

Introduction

Simulating the transport and dispersion of the atmospheric pollutants has been a focus of climate research for decades. A model that can quickly and accurately predict the dispersion of pollutants can provide crucial information for scientific evaluation and policy decisions when facing natural disasters or industrial pollution events such as volcanic eruptions, nuclear accidents or wildfires, which have a major impact on both human health and the economy. Understanding the interaction between pollutants and climate processes is essential for climate change studies. Lagrangian models play an important role in the simulation and prediction of atmospheric transport and diffusion of natural and anthropogenic pollutant emissions. Lagrangian models can simulate the feedback mechanisms between pollutant emissions and climate variables, such as temperature, precipitation, and atmospheric circulation patterns. This helps in assessing the long-term impacts of pollutants on climate.

Modeling sources and sinks is a critical component in the Lagrangian model, enhancing its capability to simulate atmospheric transport and diffusion of pollutants with high accuracy. By effectively representing sources and sinks, Lagrangian models can provide a comprehensive understanding of pollutant dynamics, which is essential for both scientific research and practical applications. For accurate emission representation, proper modeling of pollution sources, such as industrial emissions, vehicle exhaust, agricultural activities, and natural sources such as wildfires and volcanic eruptions, is crucial for reli-

able predictions. Sink modeling refers to the processes that remove pollutants from the atmosphere, such as deposition to the surface (dry and wet deposition), chemical reactions, and interactions with other atmospheric components. By accurately modeling these sinks, Lagrangian models can simulate the decay of pollutant concentrations over time and space. This is vital for predicting the lifetime and environmental impact of pollutants, especially for long-range transport scenarios.

Sulfur dioxide (SO₂) is a key magmatic volatile for volcanic geochemical analysis due to its significant presence in volcanic plumes. The lifetime of SO₂ varies from hours to months with altitude, especially in the presence or absence of clouds. The sensitivity of the SO₂ lifetime to altitude causes a large variation in the total lifetime for different volcanic eruptions. For example, the Ambae eruption case in 2018 located in the tropical region, has an e-folding lifetime of 4 ~ 5 days (Malinina et al., 2021). The Raikoke eruption case in 2019, located in the mid latitudes has an e-folding lifetime of about 20 days (Cai et al., 2022). For Lagrangian transport modeling of volcanic SO₂, chemical sink modeling is significant for the lifetime prediction. In the gas phase, SO₂ mainly decays by oxidation with hydroxyl radicals (OH). In the presence of clouds, the SO₂ will be taken up by cloud water and decays with wet deposition by precipitation and aqueous phase oxidation (Khokhar et al., 2005; Pattantyus et al., 2018).

For accurate forecasts of the pollutant dispersion, the key information of the source term such as strength, location, height and time of the emission are also essential. Due to limitations of the existing observational techniques, e.g., remote sensing satellite observations, such information is often only partially known. Satellite instruments such as the TROPOspheric Monitoring Instrument (TROPOMI) SO₂ retrieval (Veefkind et al., 2012) are able to provide high-resolution column density distributions, but still lack information on the height distribution. It is of great significance to develop estimation techniques to determine the source information in order to achieve a high-accuracy transport simulation. Uncertainties introduced by chemical sinks can strongly influence the top-down source estimation (Stavrakou et al., 2013). It is also an interesting point to investigate the effects between SO₂ lifetime modeling and the SO₂ emission reconstruction. With

different lifetime representations, the resulting source reconstruction from observations will also vary. This discrepancy arises because the modeled behavior of trace gases or aerosols, including their decomposition and interaction rates, directly influences the derived strength of emission sources. Consequently, accurate representation of the chemical lifetimes of pollutants is crucial for reliable source attribution and for understanding the broader impacts on air quality and climate.

In this thesis, we mainly focus on the development of chemistry schemes for the Lagrangian dispersion model for Massive-Parallel Trajectory Calculations (MPTRAC) to solve the transport and chemical transformation of reactive trace gases in the free troposphere and stratosphere. MPTRAC is particularly optimized for computational efficiency on high performance computing (HPC) systems with CPU and GPU devices. We aim to use the chemistry modeling of the Lagrangian transport model to investigate the decay processes of volcanic SO₂ and its lifetime altitude dependence. Another objective is to develop an inverse modeling approach for volcanic SO₂ emission reconstruction with the Lagrangian chemical transport model to investigate the effects between SO₂ lifetime modeling and the SO₂ emission reconstruction.

In the remainder of this chapter, a brief review of Lagrangian chemistry transport modeling and related studies with the Lagrangian transport model MPTRAC are given in Section 1.1. Section 1.2 reviews some recent work on volcanic SO₂ transport modeling and lifetime modeling. Section 1.3 reviews the research background and progress in atmospheric inverse modeling for source estimation. Section 1.4 presents the structure of this thesis.

1.1 Lagrangian chemical transport modeling

Lagrangian transport models represent atmospheric transport based on trajectories of atmospheric pollutants. Unlike Eulerian models, which focus on fixed spatial coordinates to calculate changes in pollutant concentrations over time, Lagrangian models track individual trajectories of air parcels according to the input meteorological data. This approach provides several key advantages that make Lagrangian models highly effective in various

scenarios:

1. Ability to represent complex flows: The Lagrangian model allows for a more accurate and flexible representation of transport processes at different space and time scales. It has the ability to better resolve some small-scale features such as elongated filaments in tropospheric and stratospheric flows (Hoffmann et al., 2016). Lagrangian models are employed to capture complex atmospheric dynamics, such as shedding of low-potential vorticity cutoffs (Clemens et al., 2022). Some phenomena exist in atmospheric flows that are not resolved in meteorological data such as turbulence and convection which can be approximated by parameterized stochastic perturbations.
2. No numerical diffusion: Unlike the Eulerian model, a Lagrangian model does not have information transfer between grid cells and maintains isolation between individual air parcels. While Eulerian models usually suffer from numerical diffusion, especially in the stratosphere, Lagrangian models need to include parameterized numerical diffusion to represent real atmospheric diffusion (Konopka et al., 2012; Wohltmann and Rex, 2009).
3. Ability for real-time application: Lagrangian models are often computationally cheaper compared to Eulerian models because they do not require the costly solution of continuity equations. The trajectory calculations for individual air parcels are usually based on explicit numerical integration according to the motions of the input meteorological fields. These trajectory calculations can be processed in parallel and have a huge scalability potential. With the fast development of HPC hardware, it is possible to conduct large-scale and long-range real-time simulations and quickly generate forecasts of pollutant dispersion, enabling timely decision-making for emergency response and public safety measures.

In the past, Lagrangian models have generally been used to qualitatively identify the source and reproduce the spatial content of the moving cloud for trace gases, e.g. tracking the air parcels backwards in time from receptors to sources to reconstruct emission

sources (Wu et al., 2017; Pardini et al., 2017). These reconstruction studies usually ignore the effects of SO₂ lifetime variations with altitude. However, Lagrangian models have the potential to be more quantitative. The essential step is to model the physical and chemical processes for accurate prediction of the species lifetime. For atmospheric species such as SO_x, NO_x, hydrocarbons and halocarbons, the chemical reactions significantly influence their sources and sinks. Uncertainties introduced by chemical sinks can strongly influence the top-down source estimation (Stavrakou et al., 2013).

In the Lagrangian framework, the species motion is reduced to the time integration along the trajectories calculated with meteorological data. The mass is always conserved within each air parcel. The modeling of the species sink is separated from the trajectory calculation and conducted in each individual air parcel. In a rigorous Lagrangian manner, the time derivative of the mass or mixing ratio of each species is prescribed with an explicit rate. This approach can be used to model the processes of dry/wet deposition, sedimentation and first-order chemical reactions. In the study of Liu et al. (2023), the evolution of SO₂ mass burden from the 2018 Ambae volcanic eruption case is simulated with an explicit rate, including wet deposition, gas phase and aqueous phase reactions, and the height sensitivity of the SO₂ loss rates, which is strongly related to cloud distributions, is discussed. To solve second-order chemical reactions which are related to the concentration of the species, the loss rate is expressed by prescribing the OH radical and H₂O₂ using a monthly zonal mean climatology. However, this approach is more suitable for simulating long-lived tracers with low concentrations. In concentrated SO₂ plumes, the OH and atmospheric H₂O₂ concentrations may decrease and even be depleted by reaction with SO₂. For a more accurate prediction, the higher-order reaction solution should be considered.

To model non-linear chemical processes, an implicit chemical solver and atmospheric mixing should be considered (Brunner, 2012). In recent years, there have been three main types of mixing schemes on Lagrangian models. One uses a dynamically adaptive grid algorithm to mimic the stretching and distortion of air, such as the Chemical Lagrangian Model of the Stratosphere (CLaMS) (McKenna et al., 2002) and the Alfred

1.1. Lagrangian chemical transport modeling

Wegener Institute Lagrangian Chemistry/Transport System (ATLAS) (Wohltmann and Rex, 2009). The second one implements the chemistry scheme on a fixed 3-D grid assuming uniform mixing of individual species within the grid, such as the U.K. Met Office's Next-Generation Atmospheric Dispersion Model (NAME) (Redington et al., 2009) and the hybrid single-particle Lagrangian integrated trajectory (HYSPLIT) model (Stein et al., 2000). The third one implements the chemistry scheme on the Lagrangian air parcels, but uses a parameter to control the degree of mixing by adding a term to relax the concentration in the air parcels to the background averaged from the fixed 3-D grid, which is applied by the UK Meteorological Office (UKMO) chemistry transport model STOCHEM (Stevenson et al., 1998). This scheme is easily implemented in parallel. It also allows the chemistry calculation to be performed separately in each of the air parcels, which is naturally suitable for parallel implementation on HPC systems.

The Lagrangian transport model MPTRAC is designed for large-scale atmospheric applications on HPC systems (Hoffmann et al., 2022). It has been implemented with a hybrid Message Passing Interface (MPI) - Open Multi-Processing (OpenMP) – Open Accelerator (OpenACC) parallelization scheme, which has been tested to show good performance and scalability on CPUs (Liu et al., 2020) and GPUs (Hoffmann et al., 2022, 2024). MPTRAC has been used in several case studies of volcanic eruptive SO₂ emissions with a backward trajectory approach (Wu et al., 2017, 2018; Cai et al., 2022) and a more advanced inverse modeling approach (Heng et al., 2016). In these studies, the height-dependent lifetime of SO₂ was not considered as an influencing factor since previous versions of MPTRAC were not equipped with a chemistry scheme. Some other simulation applications regarding to forest fire CO₂ (Liao et al., 2024) and stratospheric ice clouds (Zou et al., 2021) were also conducted without chemistry. In this thesis, we developed a chemistry module that has been implemented in the new version of MPTRAC to enable applications on reactive tracer transport simulations, especially for volcanic SO₂.

1.2 Volcanic sulfur dioxide transport modeling

Volcanic eruptions have a strong impact on human living by causing various hazards and destructive impacts on human beings' living conditions. At the ground, SO₂ and acid aerosols from eruption gases cause health hazards and increase respiratory morbidity and mortality (Hansell and Oppenheimer, 2004; Schmidt et al., 2011). The wet deposition of SO₂ leads to acid precipitation, which has a destructive effect on the ecosystem and environment, including acidification of soils, contamination of water sources and damage to vegetation (Delmelle et al., 2002). In the UT/LS, sulfate aerosol formed by SO₂ oxidation have a significant impact on the radiative forcing and energy balance of the Earth by scattering solar radiation and by absorbing and re-emitting thermal emissions (Robock, 2000; Kloss et al., 2020; Malinina et al., 2021). Satellite observations and atmospheric chemistry transport models allow us to monitor the transport of volcanic ash and SO₂ and to better plan for evacuation and hazard mitigation. Studies of the SO₂ long-range transport and dispersion can also help to better understand atmospheric dynamics, such as the impact of the Asian monsoon on aerosol transport (Wu et al., 2017).

In most of these studies, the lifetime of SO₂ was given as a constant empirical value. However, the lifetime of SO₂ varies from hours to weeks, depending on whether or not liquid or ice clouds are present (Eatough et al., 1994; McGonigle et al., 2004; Khokhar et al., 2005). Carn et al. (2016) showed the strong correlation between altitude and SO₂ lifetime for removal from volcanic plumes based on Infrared Atmospheric Sounding Interferometer (IASI) measurements, and also found large variability in the lower tropospheric plumes. Due to the variability of the atmospheric background conditions, it is hard to find a specific number to represent the local SO₂ residence time. Different total lifetimes have been found in different volcanic cases, e.g., the Ambae eruption case in July 2018 had an e-folding lifetime of SO₂ of ~4 days (Malinina et al., 2021), and the Raikoke eruption case in June 2019 had an e-folding lifetime of ~19 days. These two cases are the main focus of this thesis. The chemical transformations and wet deposition are the main factors to model the variability of the SO₂ lifetime. In the gas phase, SO₂ is mainly depleted by reaction with OH, whereas in the presence of clouds SO₂ is dissolved in cloud droplets and

1.2. Volcanic sulfur dioxide transport modeling

removed by precipitation and aqueous phase oxidation. For the aqueous phase oxidation, the reaction with H_2O_2 is considered to be the most important pathway when $\text{pH} < 5$ (Pattantyus et al., 2018; Rolph et al., 1992).

Ambae Island (15.39°S , 167.84°E), located in the South Pacific in Vanuatu, contributed the largest volcanic eruption in the year 2018. Among four major eruption phases during 2017 and 2018, the most intensive one in July 2018 injected at least 400 kt of SO_2 to a peak altitude of ~ 17 km (Moussallam et al., 2019). The volcanic SO_2 injected into the UT/LS formed aerosol particles which have a significant impact on atmospheric radiative forcing and global climate (Kloss et al., 2020; Malinina et al., 2021). Local reports of acid rain suggest that the eruption was accompanied by strong wet deposition, which means that the released SO_2 encountered significant wet removal. As we aim to better understand and represent these processes in the MPTRAC model, the Ambae eruption in July 2018 is selected as a case study for this work.

The Raikoke (48.17°N , 152.15°E) eruption in 2019 was a remarkable event that has been widely discussed in the literature. The eruption on 21-22 June was characterized by a series of explosive events that emitted SO_2 and volcanic ash into the lower stratosphere, impacting the stratospheric aerosol layer (Gorkavyi et al., 2021; Kloss et al., 2021). Cai et al. (2022) used MPTRAC to estimate the SO_2 emissions and to investigate the effects of the injection height and time and diffusion parameters. With an estimated amount of 1.5 ± 0.2 Tg of SO_2 , the eruption was notable for being the largest SO_2 injection into the upper troposphere and lower stratosphere since the 2011 Nabro eruption (Cai et al., 2022). Additionally, the hazard posed by volcanic SO_2 to aircraft occupants was quantified following the Raikoke eruption, with the SO_2 hazard area extending over a vast region and exceeding WHO concentration values for an extended period (Kristiansen et al., 2023). This eruption is also considered as an important case study in this thesis because of its characteristics of long-lasting and wide-spreading.

1.3 Inverse modeling on atmospheric source reconstruction

In the application of a Lagrangian model, the source estimation is a major issue. For an accurate simulation, key information on the source term such as strength, location, height and time of the emission will largely determine the results. Due to the limitation of the existing observational techniques, e.g., remote sensing satellite observations or in-situ measurements, such information is often partially known. The identification of the source information combining a dispersion model, limited concentration measurements and available a priori information is considered as an ill-posed inverse problem. Gerbig (2012) pointed out that a Lagrangian model has its advantages and potential in the inverse source estimation applications, including numerical efficiency for retrieving the transport adjoint (source-receptor relationships), scalability, and suitability for implementing stochastic processes. Lagrangian models, when applied to inverse dispersion, can account for flow disturbances and provide a more accurate representation of atmospheric dynamics, leading to improved source estimation (Wilson et al., 2010).

For a long-range transport simulation of a volcanic eruption, the altitude- and time-resolved emission data are crucial for accurate and reliable transport simulations. In order to estimate the source information, there are two ways to describe the functional relationship between the unknown source and observations, which is source-oriented (forward simulation) and receptor-oriented (backward simulation) (Singh et al., 2015). The source-oriented approach integrates the tracers forward in space and time to compare with the observations to find the optimized parameters. The receptor-oriented approach initializes the trajectories at the observations and integrates the advection of the tracers backward in time using the wind field in the reverse direction. This backward trajectory approach is simple but limited by the accuracy and resolution of the meteorological data (Singh et al., 2015; Hutchinson et al., 2017). In the previous MPTRAC applications, the backward trajectory approach has been widely employed in several case studies of volcanic SO₂ emission estimation with MPTRAC, e.g. Nabro, Grímsvötn, Puyehue (Hoffmann et al., 2016), Sarychev (Wu et al., 2017) Merapi (Wu et al., 2018) and Raikoke (Cai et al., 2022). The main idea is to release the air parcels proportional to the satellite observa-

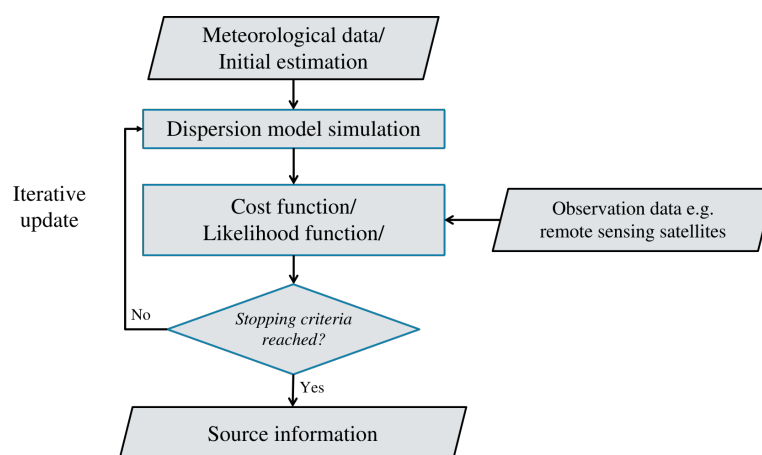


Figure 1.1: Diagram of the inverse modeling strategy.

tion signals. The trajectories are calculated in backward direction and collected at the volcano location. The source-oriented source term estimation requires more advanced inverse modeling techniques, which can be generally defined in terms of least square error (LSE), least absolute error (LAE), or maximum likelihood estimation (MLE), as illustrated in Fig. 1.1. The overall objective of these methods is to identify the most probable source term parameters that align with the predicted and observed data. In a previous study using MPTRAC, Heng et al. (2016) used an inversion approach based on the concept of sequential importance sampling combined with different resampling strategies to estimate the distribution of the volcanic SO₂ emissions. The critical success index (CSI) (Schaefer, 1990) was used to evaluate the agreement of the SO₂ plume spatial extent and adjust the importance weight of each discretized time- and altitude-dependent sub-domain. All of these approaches in the previous studies using MPTRAC reproduced the spatial extent well compared to the satellite observations, however they omitted the chemistry processes. Developing a new inverse estimation approach that takes into account the chemical changes, which is also the main objective of this thesis, should be able to improve the reconstruction results.

In the context of estimating altitude- and time-resolved volcanic emissions, there are previous studies (Eckhardt et al., 2008; Kristiansen et al., 2010, 2012, 2015) based on Seibert (2000) using a linear source-receptor relationship calculated with the Lagrangian

model Flexible Particle (FLEXPART), which is formulated as

$$\mathbf{y} = M\mathbf{x}. \quad (1.1)$$

Here \mathbf{y} denotes the observed vector, \mathbf{x} denotes the model source vector, and M is the matrix of the linear source-receptor relationship. The deviation of the linear model from the observations is minimized with a Tikhonov regularization constraint to handle the ill-posed problem. Similar methods are applied in the Inversion Technique for Emissions Modelling (InTEM) with Met Office's atmospheric dispersion model Numerical Atmospheric-Dispersion Modelling Environment (NAME) in the case of Grímsvötn (Webster and Thomson, 2022) and Raikoke (Harvey et al., 2022) for volcanic ash prediction. Such a source-receptor relationship is based on the assumption of linearity and does not require further model runs, which can yield model predictions for any arbitrary emission profile described on the height-time grid. However, in our cases with chemistry modeling of SO_2 , it is found that the non-linearity of SO_2 decay cannot be ignored. Therefore, full simulations with non-linear chemistry should be considered in the inverse model. Additionally, the studies of SO_2 emission reconstruction in the references Eckhardt et al. (2008) and Kristiansen et al. (2010) do not consider the SO_2 aqueous phase oxidation. In this thesis, it is shown that the wet deposition and aqueous phase reactions of SO_2 will significantly affect the SO_2 lifetime in the troposphere, which is expected to have an influence on the inverse reconstruction.

Besides optimization approaches, another category of inverse modeling techniques is Bayesian inference, which provides source estimation along with a probability distribution function (PDF) within a certain confidence level. The Bayesian inference method introduces probabilistic considerations to the problem to incorporate model and observation uncertainties. Based on the Bayes theorem, posterior probability $p(\mathbf{x}|\mathbf{y})$ is presented by combination of prior probability $p(\mathbf{x})$ and the likelihood function $p(\mathbf{y}|\mathbf{x})$:

$$p(\mathbf{x}|\mathbf{y}) = \frac{p(\mathbf{y}|\mathbf{x})p(\mathbf{x})}{\int p(\mathbf{y}|\mathbf{x})p(\mathbf{x})d\mathbf{x}}, \quad (1.2)$$

where $p(\cdot)$ denotes the probability density function, \mathbf{y} the observations vector, and \mathbf{x} the model input vector.

Monte Carlo sampling methods are usually utilized to draw random samples to estimate the posterior PDF, which has the advantage of not being constrained by the linearity or Gaussianity of the model (Doucet et al., 2001). In this thesis, we adopted a particle filter approach, also called sequential Monte Carlo methods, to explore the altitude- and time-dependent state space of volcanic SO₂ emissions (Doucet et al., 2001). The particle filter method was developed by Gordon et al. (1993), and has been applied to numerous high-dimensional non-linear geoscience systems (van Leeuwen, 2009; van Leeuwen et al., 2019). The particle filter is usually applied in dynamic systems, but its application is also possible for static state estimation (Chopin, 2002). In recent years, some studies applied the particle filter for Lagrangian modeling of volcanic eruptions. Franke et al. (2022) developed a particle-filter-based volcanic ash emission inversion method to estimate volcanic ash emissions and their uncertainty from column mass loading observations. The particle filter is used to assimilate the new observations to update the emissions. Capponi et al. (2022) use the particle filter to estimate the injection parameters of volcanic ash forecasts using satellite retrievals.

The particle filter approach is inherently parallel and allows to run the forward simulations simultaneously, which is considered to be computational efficient (Doucet et al., 2001; Hutchinson et al., 2017). The main idea of the particle filter is to use a set of weighted samples (particles) to approximate a posterior distribution. By introducing N independent random samples (particles), the density $p(\mathbf{x})$ can be expressed as

$$p(\mathbf{x}) = \frac{1}{N} \sum_{i=1}^N \delta(\mathbf{x} - \mathbf{x}_i), \quad (1.3)$$

where $\delta(\cdot)$ denotes the Dirac delta function and \mathbf{x}_i is the model state of sample i . The posterior PDF can be approximated by

$$p(\mathbf{x}|\mathbf{y}) = \sum_{i=1}^N w_i \delta(\mathbf{x} - \mathbf{x}_i), \quad (1.4)$$

where w_i is the so-called "normalized importance weight" (Doucet et al., 2001) given by

$$w_i = \frac{p(\mathbf{y}|\mathbf{x}_i)}{\sum_{j=1}^N p(\mathbf{y}|\mathbf{x}_j)}, \quad (1.5)$$

in which the likelihood function $P(\mathbf{y}|\mathbf{x}_i)$ is often taken as Gaussian (van Leeuwen, 2009):

$$p(\mathbf{y}|\mathbf{x}_i) = \exp\{-0.5[\mathbf{y} - H(\mathbf{x}_i)]^T \mathbf{R}^{-1}[\mathbf{y} - H(\mathbf{x}_i)]\}, \quad (1.6)$$

where $H(\mathbf{x}_i)$ is the model operator to produce results equivalent to the observations \mathbf{y} with input \mathbf{x}_i , and \mathbf{R} is the error covariance of the observations and model. Each particle member is weighted by the normalized likelihood of its model input. As a result, the distribution of importance weights approximates the posterior probability density function (PDF) (Fig. 1.2). In particle filters, to avoid filter degeneracy in high-dimensional problems where almost all of the importance weights are close to zero and only a small number of particles account for most of the weight, resampling procedure need to be introduced (Doucet et al., 2001; van Leeuwen, 2009; Wawrzynczak et al., 2014). The main idea is to eliminate samples with small normalized importance weights and reproduce new samples according to the importance weight.

This thesis uses the particle filter to develop an algorithm to solve the inversion reconstruction of the altitude- and time- resolved volcanic SO_2 release with the Lagrangian chemical transport model MPTRAC with non-linear chemistry processes on the HPC system. For this purpose, an efficient solution of the forward model $H(\mathbf{x})$ and satellite retrieval dataset \mathbf{y} should be introduced to formulate the likelihood function and importance weights.

1.4 Structure of the thesis

The main objective of this thesis is to focus on the development and applications of the chemistry module in the Lagrangian model MPTRAC. The rest of this thesis is divided into 6 chapters.

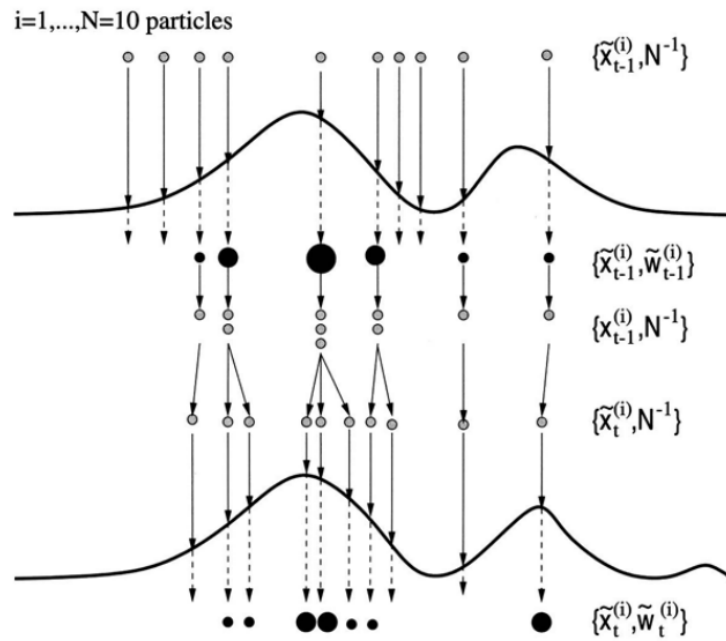


Figure 1.2: Diagram for illustration of particle filter cited from Doucet et al. (2001). The diagram illustrates the process of particle resampling, propagation, and weight update in particle filtering. It shows how particles evolve over time, with resampling based on weights and how the distribution is represented by the particles.

Chapter 2 gives an overview of the Lagrangian model MPTRAC and introduces the physical and chemistry modules developed in this thesis. The chemistry modules include an explicit scheme that can be used to solve some simplified first-order or pseudo-first-order reactions, and an implicit scheme that is capable of solving complex user-defined chemical mechanisms. An inter-parcel mixing algorithm implemented in MPTRAC is also introduced.

Chapter 3 discusses a case study of long-lived tracer simulations with the simplified explicit chemistry scheme. Three typical long-lived tracer N_2O , CFC-11 and CFC-12 are simulated globally in the period from 2002 to 2012. The results are compared with the climatologies and satellite retrievals to test the implemented photolysis and mixing scheme.

Chapter 4 discusses a volcanic SO_2 simulation case study of the Ambae case in July 2018, using the simplified chemistry scheme for gas and aqueous phase oxidation and applying the wet deposition module for precipitation removal. Based on a baseline simulation, the sensitivity tests on the SO_2 release height and the control parameters in

the wet deposition and the convection modules are discussed.

Chapter 5 discusses another volcanic SO₂ simulation case study of the Raikoke case in June 2019, comparing the simplified explicit chemistry scheme and the implicit chemistry scheme. A parameterization correction applied to the explicit scheme is proposed to model the non-linearity of the SO₂ chemistry changes, which provides a solution of the SO₂ chemical lifetime with balance of efficiency and accuracy.

In Chapter 6, an inverse modeling approach with a particle filter algorithm is proposed for the source reconstruction of volcanic SO₂ emissions, which is able to account for the non-linear decay of SO₂. Using the case study of the 2018 Ambae eruption and the 2019 Raikoke eruption, the reconstruction results are compared with the backward trajectory approach. The sensitivity of sink modeling to the reconstructed emissions is also discussed.

Finally, a summary of this thesis is given in Chapter 7.

This main part of this thesis contains two articles for peer-reviewed scientific journals. One article has already been published and the second is under review.

- Liu, M., Hoffmann, L., Griessbach, S., Cai, Z., Heng, Y., and Wu, X.: Improved representation of volcanic sulfur dioxide depletion in Lagrangian transport simulations: a case study with MPTRAC v2.4, *Geoscientific Model Development*, 16, 5197–5217, doi: 10.5194/gmd-16-5197-2023, 2023 (Published)
- Liu, M., Hoffmann, L., Grooß, J.-U., Cai, Z., Griessbach, S., and Heng, Y.: Technical note: A comparative study of chemistry schemes for volcanic sulfur dioxide in Lagrangian transport simulations: a case study of the 2019 Raikoke eruption, *EGUsphere*, 2024, 1–25, doi: 10.5194/egusphere-2024-2596, 2024 (his preprint is open for discussion and under review for *Atmospheric Chemistry and Physics (ACP)*.)

Furthermore, the following papers were published or submitted during the PhD period and are related to the Lagrangian model development:

- Hoffmann, L., Baumeister, P. F., Cai, Z., Clemens, J., Griessbach, S., Günther, G., Heng, Y., Liu, M., Haghghi Mood, K., Stein, O., Thomas, N., Vogel, B., Wu, X., and Zou, L.: Massive-Parallel Trajectory Calculations version 2.2 (MPTRAC-2.2): Lagrangian transport simula-

1.4. Structure of the thesis

tions on graphics processing units (GPUs), *Geoscientific Model Development*, 15, 2731–2762, doi: 10.5194/gmd-15-2731-2022, 2022

- Hoffmann, L., Haghighi Mood, K., Herten, A., Hrywniak, M., Kraus, J., Clemens, J., and Liu, M.: Accelerating Lagrangian transport simulations on graphics processing units: performance optimizations of Massive-Parallel Trajectory Calculations (MPTRAC) v2.6, *Geoscientific Model Development*, 17, 4077–4094, doi: 10.5194/gmd-17-4077-2024, 2024
- Liao, Y., Deng, X., Huang, M., Liu, M., Yi, J., and Hoffmann, L.: Tracking Carbon Dioxide with Lagrangian Transport Simulations: Case Study of Canadian Forest Fires in May 2021, *Atmosphere*, 15, doi: 10.3390/atmos15040429, 2024

Chapter 2

Lagrangian chemical transport modeling

2.1 Overview on the MPTRAC model

Massive-Parallel Trajectory Calculations (MPTRAC) is a Lagrangian transport model, which is designed for the heterogeneous CPU/GPU HPC systems and particularly suitable for large-scale and long-term atmospheric simulations in the free troposphere and stratosphere (Hoffmann et al., 2016, 2022). MPTRAC has a hybrid Message Passing Interface (MPI) - Open Multi-Processing (OpenMP) - Open Accelerator (OpenACC) parallelization scheme implemented, which provides an efficient solution for large-scale and compute-intensive applications. The model requires meteorological input fields, in particular the horizontal wind and vertical velocity fields for the trajectory calculations, the temperature field for the chemistry calculations and the cloud water content fields for wet deposition and aqueous phase chemistry. Primarily, trajectories of air parcels are calculated from the horizontal winds and vertical velocities of the meteorological input data with additional stochastic perturbations being added to simulate diffusion and subgrid-scale wind fluctuations. Letting $\mathbf{x}(t)$ be the position of an air parcel and $\mathbf{v}(\mathbf{x}(t), t)$ be the three-dimensional wind field, the advection of air parcels is given as

$$\frac{d\mathbf{x}}{dt} = \mathbf{v}(\mathbf{x}(t), t). \quad (2.1)$$

The explicit mid-point method is applied to solve Eq. (2.1) to maintain a balance between

2.1. Overview on the MPTRAC model

computational efficiency and accuracy (Rößler et al., 2018):

$$\mathbf{x}(t + \Delta t) = \mathbf{x} + \Delta t \mathbf{v} \left\{ \mathbf{x}(t) + \frac{\Delta t}{2} \mathbf{v}(\mathbf{x}, t), t + \frac{\Delta t}{2} \right\}. \quad (2.2)$$

Besides advection according to wind field, other unresolved processes such as mesoscale wind perturbations, turbulent diffusion and convection are implemented with parameterized stochastic representation. Following Stohl et al. (2005), diffusion is represented via stochastic perturbations added to the position of the air parcels \mathbf{x} ,

$$\Delta \mathbf{x}(t + \Delta t) = \mathbf{x}(t) + \sqrt{2\mathbf{D}\Delta t} \boldsymbol{\xi}. \quad (2.3)$$

Here the vector \mathbf{D} includes the diffusivity of horizontal and vertical components. The vector $\boldsymbol{\xi} = (\xi_x, \xi_y, \xi_z)$ is randomly drawn from the standard normal distribution. The subgrid-scale wind fluctuations are modelled as a Markov process using the Langevin equation,

$$\Delta \mathbf{v}(t + \Delta t) = r \Delta \mathbf{v}(t) + \sqrt{1 - r^2} (f\sigma)^2 \boldsymbol{\xi}, \quad (2.4)$$

$$r = 1 - 2 \frac{\Delta t}{\Delta t_{met}}. \quad (2.5)$$

This represents a Markov chain or a random walk adding temporally correlated stochastic perturbations to the winds over time. For each air parcel, the grid-scale variance σ^2 is calculated from the neighboring eight grid points between two time steps of the meteorological data. The factor f is a control parameter to be specified, which by default is set to 40%, following Stohl et al. (2005).

The subgrid-scale convection is modeled via the extreme convection parameterization (Gergig et al., 2003; Hoffmann et al., 2023) in order to represent the effects of convective up- and downdrafts being unresolved in the meteorological input data. The extreme convection parameterization requires the convective available potential energy (CAPE) and the height of the equilibrium level (EL) for input. CAPE represents the vertical atmospheric instability by integrating the local buoyancy of an air parcel from the level of free convection (LFC) to the EL,

$$\text{CAPE} = \int_{z_{\text{LFC}}}^{z_{\text{EL}}} g \left(\frac{T_{v,ap} - T_{v,env}}{T_{v,env}} \right) dz, \quad (2.6)$$

where $T_{v,ap}$ is the virtual temperature of the air parcel and $T_{v,env}$ is the virtual temperature of the environment. If the CAPE value is larger than a given threshold CAPE_0 , an air parcel will be randomly redistributed between the surface and the equilibrium level, weighted by density.

In the following section, we will introduce the physical and chemical modules implemented in the model in detail, especially the chemistry implementation, which is the main focus in this thesis.

2.2 Exponential decay processes

In a Lagrangian model, linear decay processes over time t can be expressed as

$$\frac{dy}{dt} = ky, \quad (2.7)$$

where y represents the mass or volume mixing ratio (VMR) of a species of an air parcel. For a constant loss rate k , this ordinary differential equation is solved explicitly using the exponential equation,

$$y(t + \Delta t) = y(t)e^{-k\Delta t}. \quad (2.8)$$

In MPTRAC, the rate coefficient k can be prescribed as a model input. It can be simply defined as constant e-folding lifetime of the tracer specified separately in the troposphere and stratosphere. Alternatively, it can also be formulated with the meteorological data to model the physical and chemical evolution of the tracer. In MPTRAC, various loss processes like wet/dry deposition or sedimentation are modelled in this way. When solving first-order chemical reactions, e.g., photolysis, the explicit solution has good computational efficiency as it does not require numerical integration. The reactions of long-lived tracers with short-lived radicals can also be treated as pseudo-first-order reactions, assuming that production and loss of the radicals are in equilibrium and the k can be expressed as the product of the second-order rate coefficient k_{2nd} with the concentration $[X]$ of the oxidant, $k = k_{2nd}[X]$. MPTRAC has been implemented with several pseudo-first-order chemistry schemes, the SO₂ chemistry of gas phase OH oxidation, aqueous phase H₂O₂ oxidation, and long-lived tracer chemistry of N₂O/CFC-11/CFC-12 photolysis and O(¹D) oxidation.

2.2.1 Wet deposition

In-cloud and below-cloud wet removal processes of trace gases need to be treated separately. In MPTRAC, the cloud liquid water content (CLWC) and the cloud ice water content (CIWC) of the meteorological input data are used to determine whether an air parcel is located within or below a cloud. For the modeling of in-cloud wet deposition, a similar exponential removal as in Eq. (2.8) is used with a scavenging coefficient Λ (in units of s^{-1}). The in-cloud wet deposition process

2.2. Exponential decay processes

is implemented with two schemes for a choice. The first scheme is based on the rain-out rate of cloud water, which determines the removal of a soluble trace gas taken up by cloud droplets and removal by precipitation according to the solubility of the trace gas. The in-cloud scavenging coefficient is calculated by multiplying the partition ratio of the species in the aqueous phase versus the gas phase α with the cloud water removal rate (Slinn, 1974; Levine and Schwartz, 1982; Garrett et al., 2006),

$$\Lambda = \alpha \frac{P}{LZ}, \quad (2.9)$$

where P is the precipitation rate (in units of $\text{mm} \cdot \text{h}^{-1}$), L is the volume liquid water content of the cloud (in units of $\text{m}^3 \cdot \text{m}^{-3}$), Z is the depth of the cloud layer determined by the pressure of cloud top and cloud bottom as taken from the meteorological input data, and α is defined by the partition ratio of solution gas in liquid and gas phase:

$$\alpha = \frac{N_l}{N_g} = \frac{HP_x L}{P_x / RT}, \quad (2.10)$$

according to the ideal gas law, where N_l and N_g represent the amount of solution gas in liquid and gas phase, H is Henry's law coefficient, R is the universal gas constant, and P_x is the partial pressure of species x .

Combining Eq. (2.9) and (2.10), a formula similar to the approach of the HYSPLIT model (Draxler and Hess, 1998) is obtained,

$$\Lambda = \eta H R T P Z^{-1}. \quad (2.11)$$

The factor η represents a temperature dependent retention coefficient in cloud versus equilibrium concentration in liquid water. The default value of η is set following Webster and Thomson (2014), assuming the cloud between 238.15 K to 273.15 K to be in the mixed phase, and a retention ratio in ice clouds to be 0.15:

$$\eta = \begin{cases} 1, & \text{if } T \geq 273.15 \text{ K} \\ 0.15, & \text{if } T \leq 238.15 \text{ K} \\ 0.15 + \frac{T - 238.15 \text{ K}}{273.15 \text{ K} - 238.15 \text{ K}} (1 - 0.15), & \text{if } 238.15 \text{ K} < T < 273.15 \text{ K} \end{cases} \quad (2.12)$$

SO_2 is a moderate soluble gas with a Henry's Law constant of 1.3 Matm^{-1} at 298 K (Sander, 2015). However, the solubility of SO_2 strongly depends on the pH value because it undergoes dissociation. In the simulations for SO_2 , the partition of SO_2 in clouds is represented by an effec-

tive Henry's law constant related to the pH value to account for the dissolution and dissociation of SO₂ in cloud water (Berglen et al., 2004),

$$H_{\text{eff}}(\text{SO}_2) = H(\text{SO}_2) \times \left[1 + K' / [\text{H}^+] + K'K'' / [\text{H}^+]^2 \right]. \quad (2.13)$$

Here K' and K'' are the first and second dissociation constants of SO₂, using the formulation of Berglen et al. (2004), and $H(\text{SO}_2)$ is the Henry's law constant (Sander, 2015). With this method, the pH value becomes a control parameter of the model affecting the wet deposition, for which we assumed a default value of 4.5, following the earlier work (Berglen et al., 2004; Koch et al., 1999).

For comparison, we also implemented another in-cloud wet deposition scheme applying an empirical scavenging coefficient given by

$$\Lambda = \eta a P^b. \quad (2.14)$$

The choice of the parameters a and b follows the NAME model (Webster and Thomson, 2014). The below-cloud wet deposition is a washout process through impact or diffusion with raindrops. With respect to SO₂, the washout rate has a typical magnitude of $\sim 10^{-5} \text{s}^{-1}$ (Maul, 1978; Martin, 1984; Elperin et al., 2015). Here, we set the parameters for SO₂ to $a = 2 \times 10^{-5}$ and $b = 0.616$, which follows the settings in the FLEXPART model (Pisso et al., 2019).

2.2.2 Hydroxyl radical oxidation in the gas phase

The hydroxyl radical (OH) is an important oxidant in the atmosphere, which causes rapid decay of many gas phase species. Assuming that the concentration of OH is in near steady-state, the reaction rate coefficient k in Eq.(2.8) is simplified as pseudo first-order reaction coefficient:

$$k = k_f \times [\text{OH}] \quad (2.15)$$

with an effective second-order coefficient k_f and a prescribed monthly zonal mean OH field. The oxidation of SO₂ with OH is a termolecular reaction,



2.2. Exponential decay processes

where the excited intermediate $[\text{HOSO}_2]^*$ requires an inert molecule M (e. g., N_2 or O_2) to remove the energy and stabilize it into sulfate aerosol. In the high-pressure limit, the rate-limiting step is the production of $[\text{HOSO}_2]^*$, while in the low-pressure limit, the reaction rate depends on the abundance of M and the production of HOSO_2 . Thus, the effective second-order rate coefficient of the SO_2 -OH oxidation process is temperature- and pressure-dependent, which is described here by using a formula given by the NASA Jet Propulsion Laboratory (JPL) data evaluation (Burkholder et al., 2020) as

$$k_f(T, [M]) = \frac{k_0(T) [M]}{1 + \frac{k_0(T) [M]}{k_\infty(T)}} 0.6 \left\{ 1 + \left[\log_{10} \left(\frac{k_0(T) [M]}{k_\infty(T)} \right) \right]^2 \right\}^{-1}. \quad (2.17)$$

The high-pressure limit rate $k_\infty = 2.9 \times 10^{-31} \times \left(\frac{T}{298}\right)^{-4.1} \text{ cm}^3 \text{ molecule}^{-1} \text{ s}^{-1}$ and the low-pressure limit rate $k_0 = 1.7 \times 10^{-12} \times \left(\frac{T}{298}\right)^{0.2} \text{ cm}^6 \text{ molecule}^{-2} \text{ s}^{-1}$ were also obtained from the JPL evaluation. Note that all the rate coefficient regarding the gas phase chemistry in MPTRAC, including the other chemical mechanisms introduced below, are taken from the JPL evaluation data (Burkholder et al., 2020).

In MPTRAC, prescribed radical species concentrations of OH are taken from the monthly zonal mean climatology of Pommrich et al. (2014), which has been prepared with the Chemical Lagrangian Model of the Stratosphere (CLaMS) model. The formation of OH is driven by the photolysis of ozone in the troposphere and H_2O in the stratosphere, which causes a strong correlation with diurnal variations (Minschwaner et al., 2011). In contrast to previous versions of MPTRAC, which did not take diurnal variability into account, the mean OH climatology concentration $[\text{OH}]_0$ is multiplied here by a scaling factor depending on the solar zenith angle θ_{SZA} as proposed by Minschwaner et al. (2011) to model the diurnal variations,

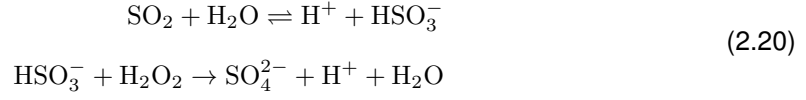
$$f(\theta_{\text{SZA}}) = \exp[-\beta \sec(\theta_{\text{SZA}})]. \quad (2.18)$$

The term $\sec(\theta_{\text{SZA}})$ is the approximate air mass factor which represents the ratio of the optical slant path to the effective vertical path. The parameter β represents the vertical optical depth. Based on Minschwaner et al. (2011), a β value of 0.6 is used for simulations covering the UT/LS region. To maintain the same mean values of the scaled data as the monthly OH field, the factor is divided by a normalization factor obtained by integrating the correlation factor f over longitude λ . The final OH concentration is calculated as

$$[\text{OH}] = \frac{[\text{OH}]_0 f(\theta_{\text{SZA}})}{\int_{-180}^{180} f(\theta_{\text{SZA}}(\lambda)) d\lambda / 360^\circ}. \quad (2.19)$$

2.2.3 Hydrogen peroxide oxidation in the aqueous phase

The in-cloud oxidation pathway of SO₂ is mainly dominated by the reaction with hydrogen peroxide (H₂O₂),



Another oxide of SO₂ in liquid phase, O₃, is not considered here because its effects are expected to be negligible when pH ≤ 5 (Rolph et al., 1992; Pattantyus et al., 2018). The concentration of the SO₂ in the aqueous phase is converted into a mass concentration in the air by multiplying the cloud water volume content L , thus the oxidation rate of SO₂ by H₂O₂ is formulated as (Rolph et al., 1992):

$$\frac{d[\text{SO}_2]_{aq}}{dt} = \frac{d[\text{SO}_2]_g/L}{dt} = -k_{\text{H}_2\text{O}_2} H_{\text{H}_2\text{O}_2} [\text{H}_2\text{O}_2] K' H_{\text{SO}_2} [\text{SO}_2]_g. \quad (2.21)$$

Here, $H_{\text{H}_2\text{O}_2}$ and H_{SO_2} represent the Henry's law constants of H₂O₂ and SO₂ (Sander, 2015). K' is the first dissociation constant of H₂SO₃ (Berglen et al., 2004) and L is the volume liquid water content of the clouds. The monthly zonal mean H₂O₂ background field was obtained from the Copernicus Atmosphere Monitoring Service (CAMS) reanalysis (Inness et al., 2019) compiled into a monthly zonal mean climatology. Then the rate coefficient used in Eq. (2.8) of the H₂O₂ aqueous phase chemistry module is formulated as

$$k = k_{\text{H}_2\text{O}_2} H_{\text{H}_2\text{O}_2} [\text{H}_2\text{O}_2] K' L H_{\text{SO}_2}. \quad (2.22)$$

The reaction rate coefficient $k_{\text{H}_2\text{O}_2}$ is formulated following Maaß et al. (1999)

$$k_{\text{H}_2\text{O}_2} = 9.1 \times 10^7 \times \exp \left[29700/R_i \times \left(\frac{1}{T} - \frac{1}{298.15} \right) \right], \quad (2.23)$$

in unit of (mol/L)⁻²s⁻¹. Here R_i denotes the ideal gas constant. When the air parcel is located inside a grid box where the cloud water content is non-zero, the H₂O₂ oxidation scheme is activated to contribute to the depletion of SO₂.

2.2.4 Long-lived tracer chemistry

Lagrangian transport models are particularly useful for modeling stratospheric long-lived tracer, such as Chlorofluorocarbons (CFCs) and N₂O, since they are less diffusive than Eulerian models (Hoppe et al., 2014). Stratospheric loss of the long-lived tracers is mainly due to photolysis

2.3. Implicit chemistry scheme

reactions, which is influenced by seasonal cycles and the Quasi-Biennial Oscillation, affecting surface variability through stratosphere-troposphere exchange (Ruiz et al., 2021). The accurate representation of these long-lived tracers is crucial for understanding their environmental impact and predicting O₃ layer recovery (Chipperfield et al., 2014). In MPTRAC, we have implemented the explicit first-order scheme with simplified chemistry mechanisms following (Pommrich et al., 2014), including photolysis reaction and O(¹D) oxidation. The O(¹D) reaction uses the monthly zonal mean climatology data modeled by the CLaMS model (Pommrich et al., 2014), to form the pseudo first order reaction rate.

For photolysis modeling, we created 3-D photolysis rate look-up tables for the different species, $J = J(\theta_s, \text{TCO}, p)$, where θ_s is the solar zenith angle, TCO is the total column O₃, and p is the pressure. The photolysis rate look-up tables cover 33 solar zenith angles from 0 to 96°, 8 total column O₃ levels from 100 to 450 DU, and 66 pressure levels from 1013.25 to 0.1 hPa. The look-up tables were generated using the DISSOC photolysis module of CLaMS, originally based on Lary and Pyle (1991) and improved over time in several studies (Becker et al., 2000; Hoppe et al., 2014; Pommrich et al., 2014). Note that for the DISSOC photochemistry model, we established the relationship between pressure, temperature, and O₃ via the U.S. Standard Atmosphere, 1976. The MPTRAC chemistry code determines θ_s , TCO, and p for each air parcel and linearly interpolates the corresponding J values from the look-up tables. The look-up table approach has the advantage of high computational efficiency and easy implementation on both GPUs and CPUs.

2.3 Implicit chemistry scheme

The simplified pseudo first order chemistry scheme is based on the assumption that the oxidant (e.g. OH, O¹D or H₂O₂ as introduced in the previous section) is in equilibrium state, where its production and loss rates are balanced. This assumption allows for an efficient explicit solution with an exponential formulation applied to the mass or VMR of air parcels. However, this simplified chemistry scheme comes with its limitations and assumptions that need careful consideration. The assumption that the oxidant remains in a constant equilibrium state may not hold in all scenarios. In conditions where the pollutant levels suddenly change, such a balance may be disrupted. Moreover, this approach might oversimplify the interactions in systems where multiple pathways exist. In such cases, assuming a single pseudo-first-order process might not capture the full dynamics of the whole system. For this reason, an implicit chemistry scheme is implemented in MPTRAC for further investigations.

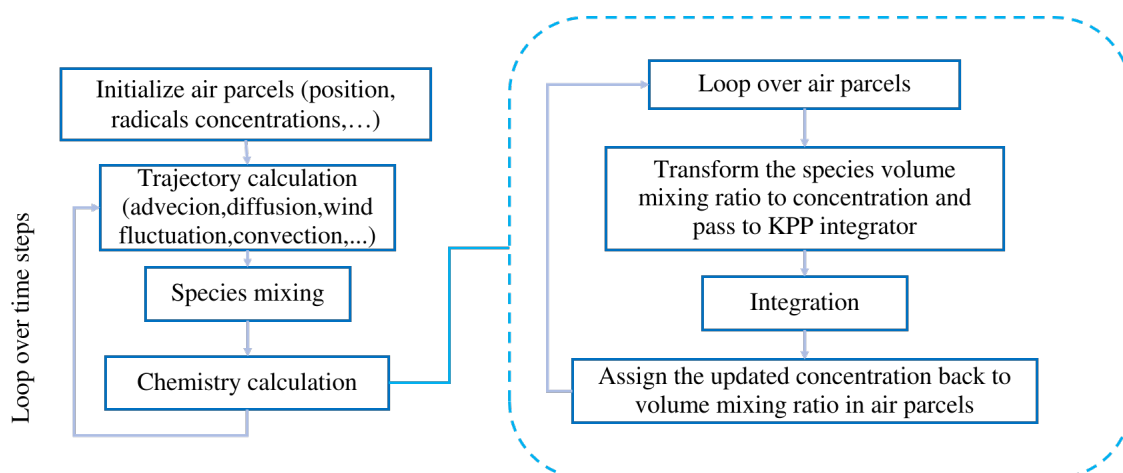


Figure 2.1: Simplified flow chart of the Massive-Parallel Trajectory Calculations (MPTRAC) Lagrangian chemistry-transport model.

A flow chart of the chemistry implementation in MPTRAC is shown in Fig. 2.1. The chemistry calculation follows the trajectory calculations and the mixing process. At each chemistry time step, the species VMRs of each air parcel are multiplied by the molecular density of air to convert them into concentration units (molecules/cm³). The chemical solver was built using the Kinetic Preprocessor (KPP) software package (Damian et al., 2002; Sandu and Sander, 2006). The KPP software provides a framework to automatically generate a Rosenbrock integrator for solving the stiff ordinary differential equations with specification of a chemical mechanism, including the chemical equations, species, and rate coefficients. The KPP has been widely used in atmospheric chemical modeling, for instance in GEOS-CHEM (Henze et al., 2007) and MECCA (Sander et al., 2019). After numerical integration of the chemical mechanism with the KPP integrator, the updated concentrations evolved in time are converted back to VMRs and assigned back to each air parcel. The chemical processes of different air parcels are calculated independently of each other, making this an high-throughput parallel compute problem, which is particularly suitable for parallelization. The package provides a robust and flexible platform for generating integrators based on user-defined kinetic mechanisms. It can generate an integrator from a kinetic description file, which includes the involved species, chemical equations, and rate coefficients. Users have the flexibility to input the necessary chemical mechanisms according to their specific requirements.

In this work, our proposed chemistry mechanism for volcanic SO₂ in the UT/LS region includes 31 reactions and 12 species, detailed in Table 2.1. This mechanism models the dynamic production and loss of the OH and H₂O₂ concentration to further simulate SO₂ oxidation in both gas and aqueous phases, which are major loss mechanisms (Pattantyus et al., 2018; Rolph et al., 1992). OH production mainly occurs via the reaction of H₂O with the excited oxygen radical O(¹D)

2.3. Implicit chemistry scheme

Table 2.1: Proposed chemistry scheme for volcanic SO₂ oxidation in the UT/LS region.

Index	Reaction	Index	Reaction
R1	$O(^3P) + O_2 \longrightarrow O_3$	R17	$H + HO_2 \longrightarrow H_2 + O_2$
R2	$O(^3P) + O_3 \longrightarrow 2O_2$	R18	$OH + O_3 \longrightarrow HO_2 + O_2$
R3	$O(^3P) + OH \longrightarrow O_2 + H$	R19	$OH + OH \longrightarrow H_2O + O(^3p)$
R4	$O(^3P) + HO_2 \longrightarrow OH + O_2$	R20	$OH + OH \longrightarrow H_2O_2$
R5	$O(^3P) + H_2O_2 \longrightarrow OH + O_2$	R21	$OH + HO_2 \longrightarrow H_2O + O_2$
R6	$O(^1D) + O_2 \longrightarrow O(^3P) + O_2$	R22	$OH + H_2O_2 \longrightarrow H_2O + HO_2$
R7	$O(^1D) + O_3 \longrightarrow O(^3P) + O_2$	R23	$HO_2 + O_3 \longrightarrow OH + 2O_2$
R8	$O(^1D) + H_2 \longrightarrow OH + H$	R24	$HO_2 + HO_2 \longrightarrow O_2 + H_2O_2$
R9	$O(^1D) + H_2O \longrightarrow 2OH$	R25	$O_2 + hv \longrightarrow 2O(^3P)$
R10	$O(^1D) + N_2 \longrightarrow O(^3P) + N_2$	R26	$O_3 + hv \longrightarrow O(^1D)$
R11	$O(^1D) + N_2 \longrightarrow N_2O$	R27	$O_3 + hv \longrightarrow O(^3P) + O_2$
R12	$O(^1D) + N_2O \longrightarrow \text{prod}$	R28	$H_2O + hv \longrightarrow H + OH$
R13	$H + O_2 \longrightarrow HO_2$	R29	$H_2O_2 + hv \longrightarrow 2O(^3P)$
R14	$H + O_3 \longrightarrow OH + O_2$	R30	$SO_2 + H_2O_2(\text{aq}) \longrightarrow \text{prod}$
R15	$H + HO_2 \longrightarrow 2OH$	R31	$SO_2 + OH \longrightarrow \text{prod}$
R16	$H + HO_2 \longrightarrow O(^3P) + H_2O$		

(Reaction R9). Its concentration exhibits a clear diurnal variation due to the strong relationship with solar radiation and photolysis, and its short lifetime from self-reaction and reactions with O₃ (Reaction R9) and HO₂ (Reaction R21) (Minschwaner et al., 2011; Tan et al., 2019). H₂O₂ is primarily produced through the self-reaction of hydroperoxyl radicals (HO₂) (Reaction R24), which are mainly produced via H and O₂ (Rieger et al., 2018).

Regarding the SO₂ chemical reactions, the gas phase oxidation with OH and the aqueous phase oxidation with H₂O₂ are considered. In the cloud aqueous phase, H₂O₂ oxidation is the predominant pathway when pH<5 (Seinfeld and Pandis, 2016; Rolph et al., 1992; Pattanyus et al., 2018). Other aqueous phase oxidation pathways such as O₃ oxidation and catalyzed oxidation via Fe(III) and Mn(II) are neglected because of low pH values in highly concentrated SO₂ volcanic plumes. Note that this scheme for the oxidation of SO₂ was not designed for application in the boundary layer and lower troposphere, as it excludes nitrogen oxides (NO_x), hydrocarbons, and carbon monoxide emissions and reactions. Furthermore, to simplify and constrain the chemistry calculations, each air parcel's O₃ VMR is updated at every chemistry time step using ERA5

reanalysis data. Water vapor is also updated using ERA5 reanalysis data. The rate coefficients of all chemical reactions were also taken from the NASA JPL evaluation (Burkholder et al., 2020), except for the R30 reaction, which is taken from Maaß et al. (1999).

2.4 Inter-parcel mixing algorithm

Atmospheric mixing is particularly important for properly modeling chemistry and transport in Lagrangian models (Brunner, 2012). The Lagrangian method inherently avoids numerical diffusion. Some form of mixing needs to be included to simulate transport and chemistry in realistic manners. Here, we adapted the inter-parcel mixing scheme of Collins et al. (1997). This mixing scheme has the advantage of simple implementation and being well suited to CPU and GPU parallelization.

Following Collins et al. (1997), a relaxation term $d(c - \bar{c})$ is added to bring the VMR value c of each air parcel closer to the average value \bar{c} within fixed grid boxes. A mixing parameter of $d = 0$ means there is no mixing whereas a mixing parameter of $d = 1$ means the species VMR is fully relaxed to the grid box mean. The parameter d controls the degree of mixing. Default values of d are taken from Stevenson et al. (1998) to be 10^{-3} in the troposphere and 10^{-6} in the stratosphere. The grid box size was set to $5^\circ \times 5^\circ \times 1$ km (longitude \times latitude \times log-pressure height). Mixing was conducted at every time step of the model. Sensitivity tests with the mixing scheme are discussed in Chapter 3.

Chapter 3

Case study of long-lived tracers with the simplified explicit chemistry scheme

Nitrous oxide (N_2O) and chlorofluorocarbons (CFCs) are two critical long-lived tracers in atmospheric studies due to their significant impacts on climate change and stratospheric O_3 depletion (Solomon, 1999; Ravishankara et al., 2009). Understanding and accurately modeling these long-lived tracers is essential for predicting future atmospheric conditions and developing effective environmental policies. Modeling long-lived tracers in the atmosphere provides valuable insights into global transport processes and contributes to our understanding of global distributions, trends, and budgets. N_2O is a potent greenhouse gas with a global warming potential. It also plays a crucial role in the stratosphere, where it contributes to O_3 layer depletion through photochemical reactions (Prather et al., 2015). The primary sources of N_2O are agricultural activities, industrial processes, and fossil fuel combustion, making its modeling vital for addressing both climate change and O_3 depletion (Tian et al., 2020). CFCs are synthetic compounds once widely used as refrigerants, solvents, and in foam production. Their long atmospheric lifetimes mean that they continue to affect the stratospheric O_3 layer and contribute to greenhouse warming. Understanding the transport, distribution, and degradation of these compounds is essential for assessing the long-term recovery of the O_3 layer and the ongoing impacts on climate.

Photolysis in the stratosphere is identified as the primary removal mechanism for these gases. Accurate representation of photochemical processes and transport in models is crucial for determining the atmospheric lifetimes of these gases, which has implications for their global budgets and potential impacts on O_3 depletion and climate change (Ko et al., 1991). This section aims to evaluate the simplified first-order explicit chemistry scheme (especially the photochemical processes) and mixing scheme by comparing the simulated global distributions of the long-lived trac-

ers N_2O , CCl_3F (CFC-11) and CCl_2F_2 (CFC-12) with observational data from the Stratosphere-troposphere Processes and their Role in Climate (SPARC) Data Initiative trace gas climatologies (Hegglin et al., 2021) and Michelson Interferometer for Passive Atmospheric Sounding (MIPAS) data (Fischer et al., 2008).

3.1 Data and method

3.1.1 Lagrangian chemical transport simulations of long-lived tracers

For the long-lived tracers, we implemented the simplified explicit chemistry scheme introduced in Chapter 2 for efficient global long-term integration. The photolysis rates of the long-lived tracers are prescribed with 3-D look-up tables as functions of solar zenith angle, total O_3 column and pressure, $J = J(\theta_s, \text{TCO}, p)$, prepared with the CLaMS model. For comparison, photolysis data from the Tropospheric Ultraviolet-Visible (TUV) model, as described by Madronich (1987) and Tie et al. (2003), were also utilized. The evaluation of these two photolysis rate data is discussed below in comparison to the measurements.

The inter-parcel mixing scheme implemented in MPTRAC, which was proposed by Collins et al. (1997), is also evaluated in this chapter. In each simulation time step of 360 seconds, a relaxation term $d(c - \bar{c})$ is added on each air parcel. This term helps to smooth the VMR of the tracers towards the mean value calculated within a grid of $5^\circ \times 5^\circ \times 1$ km. The parameter d can be tuned to control the mixing degree.

3.1.2 ECMWF reanalysis

In this chapter, the European Centre for Medium-Range Weather Forecasts (ECMWF) reanalyses are used as meteorological data to drive the Lagrangian transport model MPTRAC for simulation of the long-lived tracers. This includes the ERA-Interim (Dee et al., 2011) and the new generation product ERA5 reanalysis (Hersbach et al., 2020). Launched in 2006, ERA-Interim covers from 1979 to 2019, providing 6-hourly data in resolution of $0.75^\circ \times 0.75^\circ$ with 60 vertical levels up to 0.1 hPa. It has been widely used in climate research and provides a wide variety of atmospheric, oceanic, and land surface parameters. ERA5 is the successor to ERA-Interim and was introduced in 2016. It offers higher resolution and more accurate reanalysis data, covering the period from 1950 to the present. ERA5 provides hourly updates with a spatial resolution of 31 kilometers ($0.3^\circ \times 0.3^\circ$) with 137 vertical levels up to 0.01 hPa, significantly improving both the spatial and

temporal precision of the data. We did not use the full-resolution of ERA5 data because of the high computational cost and amount of reanalysis data needed in long-range simulations. Instead, reduced-resolution ERA5 reanalysis data are used, created by downscale the full-resolution ERA5 data to 6-hourly data with $1^{\circ} \times 1^{\circ}$ horizontal grid, keeping the vertical levels of ERA5 unchanged (Ploeger et al., 2021).

3.1.3 SPARC Data Initiative

The SPARC (Stratosphere-troposphere Processes And their Role in Climate) Data Initiative has conducted comprehensive assessments of stratospheric composition measurements from satellite limb sounders (Hegglin et al., 2021). This initiative compiled and compared time series of zonal monthly mean trace gas and aerosol fields, aiming at understanding and documenting the distribution and variability of trace gases in the stratosphere and upper troposphere. The initiative covers a variety of trace gases, including O_3 , H_2O , CH_4 , N_2O , CFCs, and other halogenated species. Key satellite instruments contributing to N_2O , CFC-11 and CFC-12 observations include the Atmospheric Chemistry Experiment-Fourier Transform Spectrometer (ACE-FTS), the Microwave Limb Sounder (MLS), and the Michelson Interferometer for Passive Atmospheric Sounding (MIPAS). Among these instrument, MIPAS covers all three species targeted in this work and covers a long period from 2002 to 2012, which are therefore the key measurements.

3.1.4 MIPAS satellite observations

Michelson Interferometer for Passive Atmospheric Sounding (MIPAS) was an instrument aboard the European Space Agency's ENVISAT satellite operated from 2002 to 2012, which measured the high-resolution limb emission spectra from the mid-troposphere to the mesosphere (Fischer et al., 2008). The MIPAS Level 2 (L2) product refers to the processed data derived from the instrument's radiance measurements (Level 1 data) that provides detailed information about atmospheric composition. For comparison with the MPTRAC simulations, we collect MIPAS data for a specific point in time, with a ± 3 -day and run the MPTRAC forward and backward simulations to obtain a more detailed tracer distribution, as shown in Fig. 3.5c.

3.1.5 Model initialization and setup

In this section, we describe the model settings and initialization approach. The simulations of the long-lived tracers' distribution is cover the period from 01/01/2003 to 12/31/2011, which matches

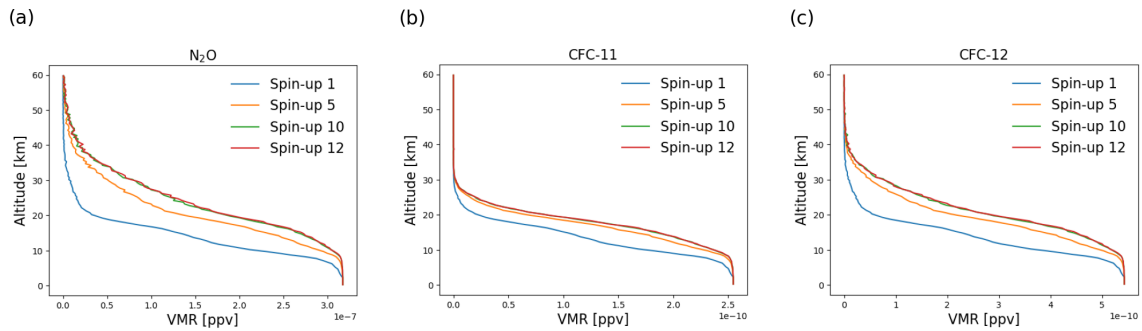


Figure 3.1: Global mean vertical VMR profiles of the long-lived tracer N_2O (a), CFC-11 (b), CFC-12 (c) in spin-up steps of 1, 5, 10 and 12.

the MIPAS observations. The simulation of the long-lived tracers uses a spin-up strategy to initialize the tracer concentrations of the air parcels. Specifically, the model is repeatedly run for an extended period of time to allow it to reach a quasi-equilibrium state before the actual simulation begins. By doing so, initial transient effects that could skew the results are minimized, ensuring that the tracer concentrations are representative of steady-state conditions. The spin-up period is selected as 01/01/2002 to 12/31/2003. We initialize the spin-up simulation of the tracers N_2O , CFC-11 and CFC-12 with MPTRAC by globally distributing air parcels from the surface up to 55 km with a model boundary layer depth of 2.5 km. The lower boundary conditions of the tracers are taken from the global monthly-mean data from in-situ measurements of the National Oceanic and Atmospheric Administration (NOAA) Global Monitoring Laboratory (GML) (Dutton et al., 2024a,b,c). Fig. 3.1 shows the vertical VMR distribution profiles of the long-lived tracers N_2O , CFC-11, CFC-12 in different spin-up steps. It is shown that the spin-up simulation converges after 10 years of spin-up iterations.

3.2 Results

In this section, simulation results will be compared with the climatologies of the SPARC Data Initiative, including the measurements of MIPAS, ACE-FTS and MLS instruments. MIPAS and ACE-FTS contain data of the three long-lived tracers, while MLS provides the N_2O data.

3.2.1 Sensitivity of meteorological data

First, we discuss the sensitivity of meteorological data to the long-lived tracer simulations. The simulation results with the reduced resolution ERA5 reanalysis and ERA-Interim reanalysis are compared with the monthly SPARC climatologies with the measurements of the the MIPAS and

ACE-FTS instruments in Fig. 3.2. The simulations generally show good agreement with the MIPAS and ACE-FTS measurements. The ERA5 simulations tend to show slightly higher concentrations of the long-lived tracers compared to ERA-Interim, especially at higher altitudes and higher latitudes. This is attributed to the stronger Brewer-Dobson circulation in the ERA5 reanalysis compared to the ERA-interim reanalysis. In the tropical regions, the difference between ERA5 and ERA-Interim simulations is small (Fig. 3.2a, d, g), which is resulted from the extreme convection parameterization scheme in MPTRAC (Hoffmann et al., 2023), which can better represent the effects of unresolved convective transport in the global meteorological reanalyses. In the mid-latitude and polar regions, the higher VMRs found in the ERA5 simulations are more consistent with the measurements (Fig. 3.2b, c). These discrepancies highlight the importance of accurate representation of meteorological fields in reanalyses, which affects the simulation of tracer distributions.

3.2.2 Evaluation of the photolysis data

Figure 3.3 shows that the photolysis rates derived from the TUV model are approximately 20% higher than those derived from the CLaMS model. Higher photolysis rates from the TUV model suggest a faster photodissociation process, leading to lower simulated concentrations of these tracers in the atmosphere (Fig. 3.3). This is particularly evident in the upper stratosphere, where the effect of photolysis is more pronounced. This discrepancy may be attributed to differences in the parameterizations and input data used by the two models, including factors like solar radiation intensity and atmospheric composition. Figure 3.4 shows the sensitivity tests of the photolysis data on the simulation results. Focusing on the altitudes where a steep gradient occurs (between 20 and 30 km) in the tropical (Fig. 3.4a, d, g) and mid-latitude (Fig. 3.4b, e, h) regions, the simulations with CLaMS photolysis data predict slightly higher tracer concentration values than the TUV photolysis data, which aligns more closely with the observations. In the polar regions (Fig. 3.4c, f, i), both schemes agree well with the observational data while the simulations with CLaMS photolysis show a slightly higher prediction of the tracer concentrations. Overall, the CLaMS photolysis performs better than the TUV photolysis.

3.2.3 Sensitivity on mixing parameters

In this section, we discuss the impact of the mixing module to the simulations of long-lived tracers. Figure 3.5 presents a comparison between the MPTRAC model outputs and MIPAS observations,

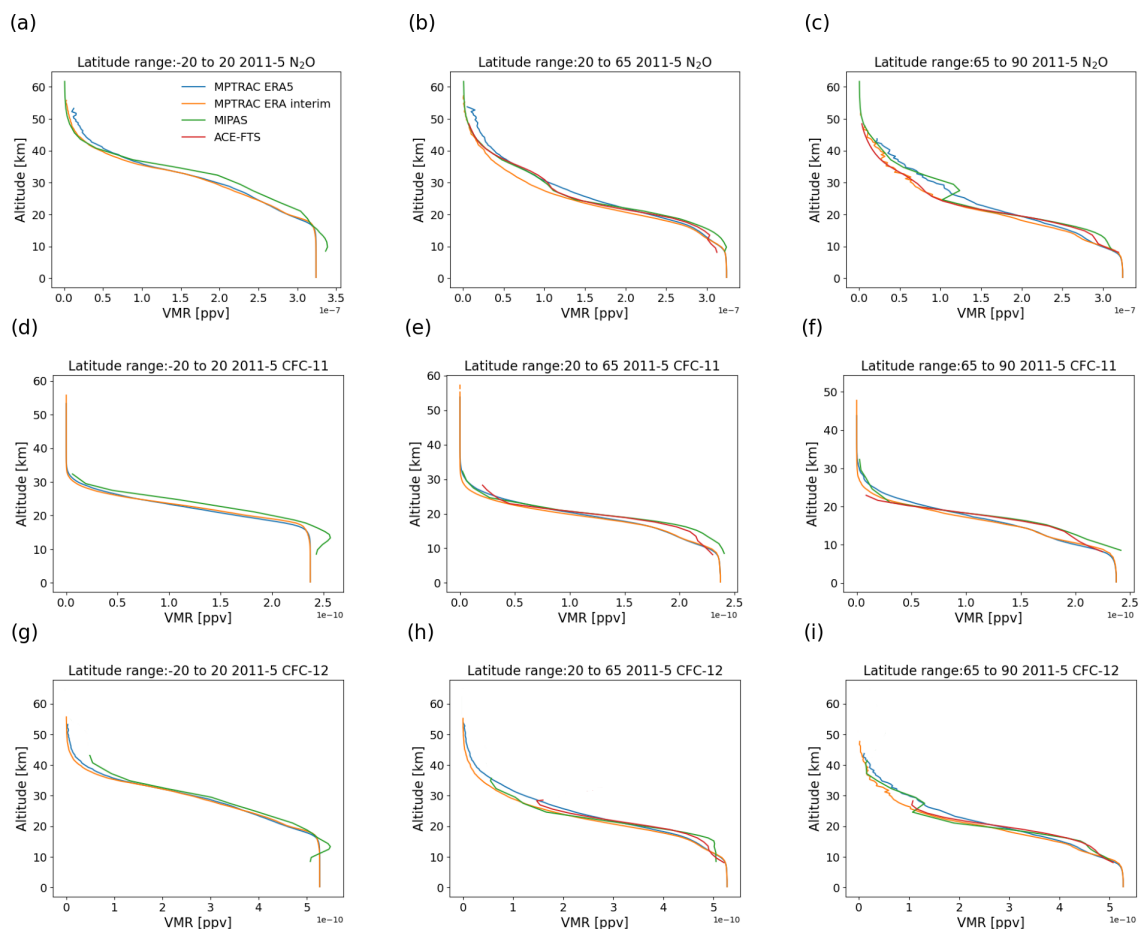


Figure 3.2: Vertical VMR profiles of the MPTRAC simulations for N_2O (panels a, b, c), CFC-11 (panels d, e, f), and CFC-12 (panels g, h, i) in May 2011 for three latitude ranges: -20 to 20, 20 to 65, and 65 to 90 degrees, with different meteorological data from ERA5 (blue curves) and ERA-Interim (orange curves) reanalyses, compared with measurements from MIPAS (green curves) and ACE-FTS (red curves).

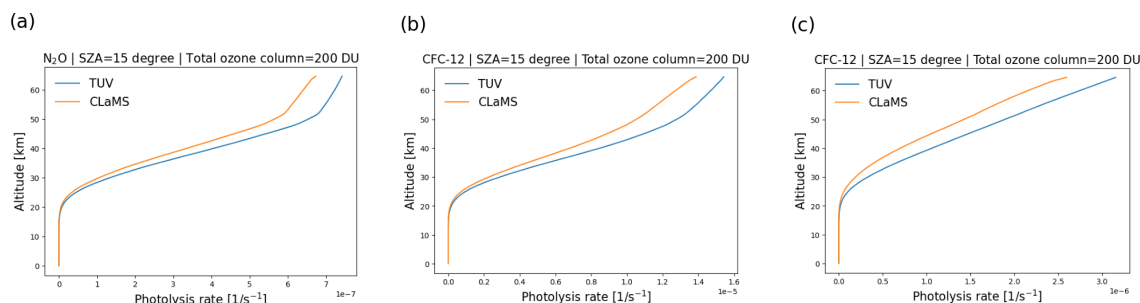


Figure 3.3: Vertical VMR profile of the long-lived tracer N_2O (a), CFC-11 (b), CFC-12 (c) in spin-up steps of 1, 5, 10 and 12.

3.2. Results

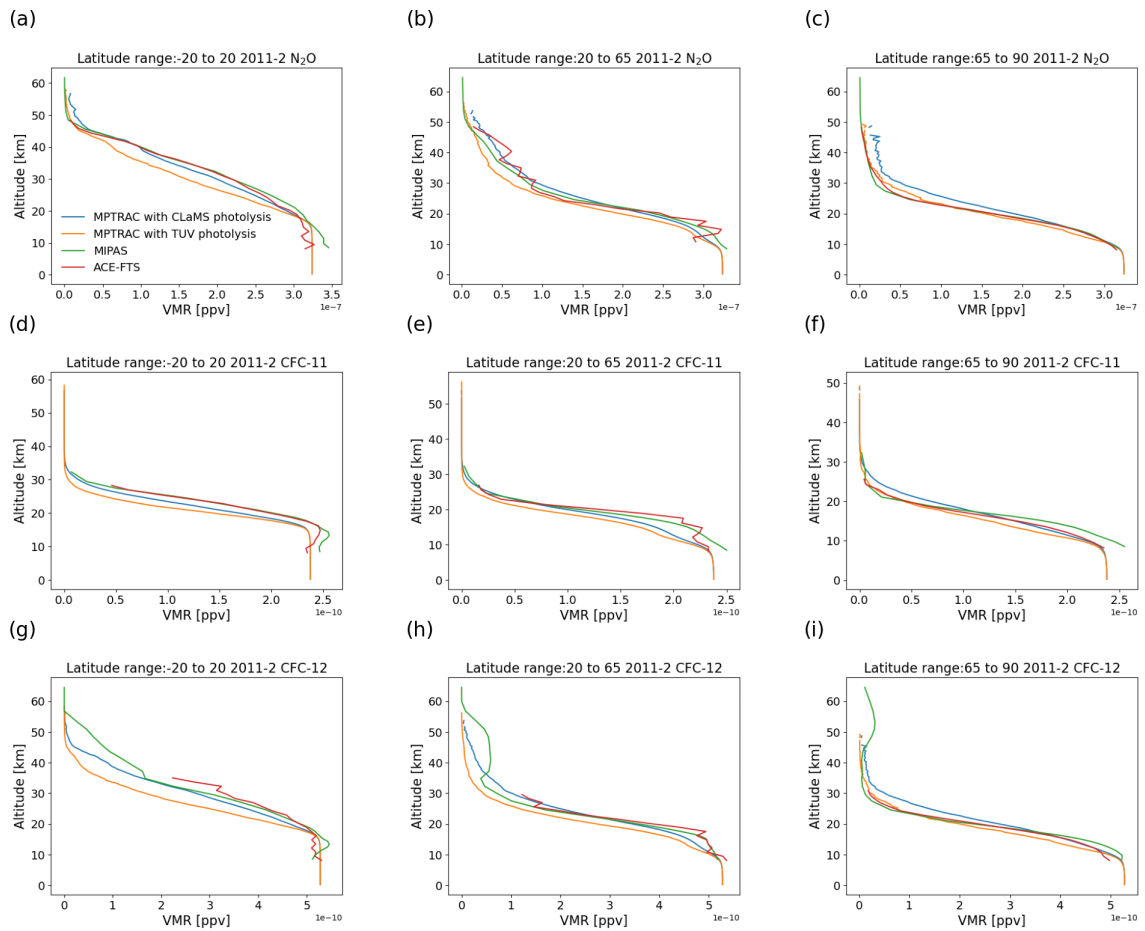


Figure 3.4: Vertical VMR profiles of the MPTRAC simulations for N_2O (panels a, b, c), CFC-11 (panels d, e, f), and CFC-12 (panels g, h, i) for three latitude ranges: -20 to 20, 20 to 65, and 65 to 90 degrees, with different photolysis rate modeled by CLaMS (blue curves) and TUV (orange curves), compared with measurements from MIPAS (green curves) and ACE-FTS (red curves).

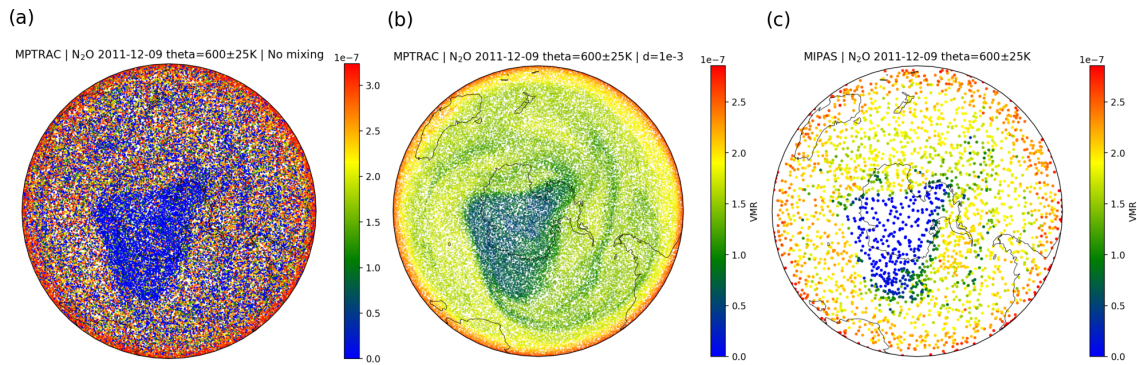


Figure 3.5: Comparison of simulated and observed VMR of N_2O at the $600\pm 25\text{K}$ potential temperature surface in the Antarctic region on December 9, 2011. Panel (a) and (b) shows the simulated distribution without and with mixing processes. Panel (c) shows the observed distribution of the MIPAS measurement.

demonstrating the influence of mixing processes on the spatial distribution of N_2O at a potential temperature of approximately 600 K. Figure 3.5a shows the N_2O distribution simulated by the MPTRAC model without the inclusion of mixing processes. The absence of mixing results in a highly noisy distribution, indicating that the tracer is poorly mixed. Since there is no numerical diffusion in a Lagrangian model, the lack of inter-parcel mixing leads to unrealistic distributions and sharp local gradients, which do not accurately represent the smoother transitions typically observed in the actual atmosphere as shown in the MIPAS observations (Fig. 3.5c). In contrast, Fig. 3.5b displays the N_2O distribution when the inter-parcel mixing is included in the MPTRAC model. As a result, the tracer distribution appears much smoother, with more gradual transitions between regions of varying concentrations. The inclusion of inter-parcel mixing significantly improves the realism of the simulation, producing a distribution pattern that better aligns with natural atmospheric mixing and the observed data. The simulated distribution with mixing in Fig. 3.5b shows a clear vortex in the Antarctic region with lower N_2O values, which is in good agreement with the MIPAS observations in 3.5c. Additionally, the simulation successfully captures smaller filamentary structures around the vortex region, further aligning with the observed patterns.

To analyze the influence of the mixing parameter d , we conducted sensitivity tests using different values of d and compared the simulated VMR standard deviations with MIPAS measurements, as shown in Fig. 3.6. The primary focus was on adjusting the mixing parameter d within the stratosphere, as the satellite measurements in the lower and mid troposphere are less reliable. In the tropics (Fig. 3.6c), a stratospheric mixing parameter with a value of 1×10^{-3} (blue curve) provides the best fit with the MIPAS data at most altitudes. This suggests that mixing processes in the equatorial stratosphere are more intense, requiring a higher value of d to accurately represent the tracer variability. The results in the polar regions and mid-latitude regions (Fig. 3.6a, b, d, e)

3.2. Results

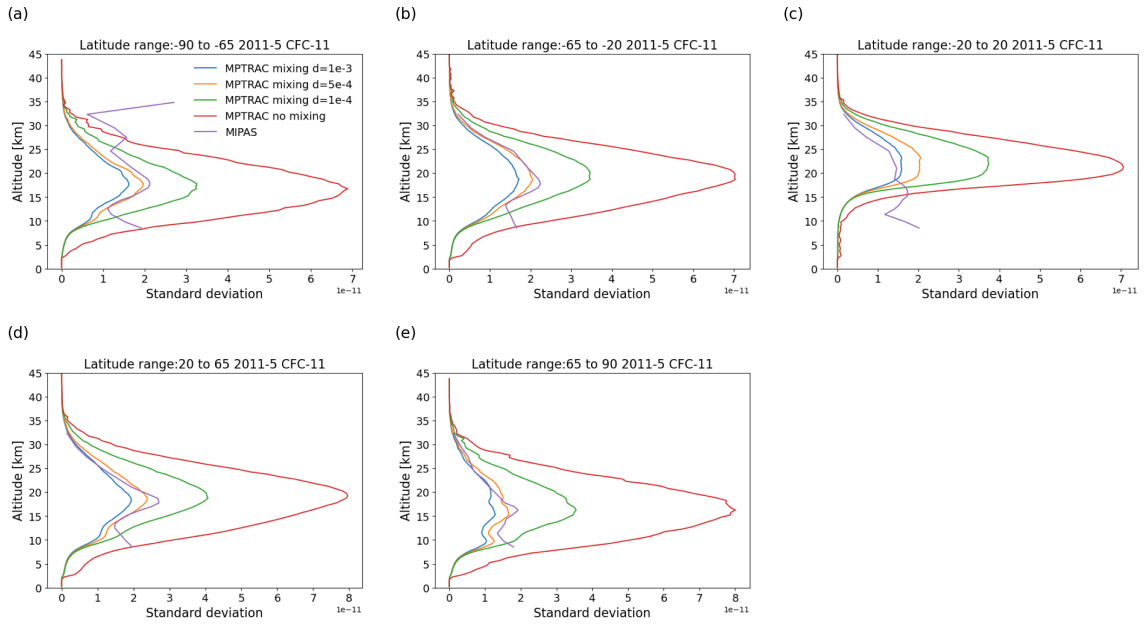


Figure 3.6: Vertical standard deviation profiles of the MPTRAC simulations for CFC-11 for five latitude ranges in May, 2011: -90 to -65 (a), -65 to -20 (b), -20 to 20 (c), 20 to 65 (d), and 65 to 90 (e) degrees, with different parameter d controlling the mixing degree, compared with measurements from MIPAS data (purple curves).

indicate that the optimal value of the mixing parameter d is 0.5×10^{-4} (shown as orange curves in Fig. 3.6).

3.2.4 Model results across different potential temperatures

Figure 3.7, 3.8 and 3.9 offer a comparative analysis between the satellite-observed (MIPAS) and model-simulated (MPTRAC) distributions of three long-lived tracers: N_2O , CFC-11, and CFC-12, across four different potential temperature levels (400 K, 500 K, 600 K, and 700 K).

For N_2O (Fig. 3.7), the MIPAS data (first row) show a higher concentration (red regions) around the outer edges, with lower concentrations (green to blue regions) towards the center, particularly near the South Pole. This gradient is consistent across all temperature levels. The MPTRAC simulation (second row) captures this gradient well, with a smoother transition between regions of high and low concentration, indicating a good representation of the spatial distribution of N_2O as observed by the satellite.

For CFC-12 (Fig. 3.8), the MIPAS observations (first row) show high concentrations at the edges, with a central area of low concentration that becomes more pronounced with increasing potential temperature. The MPTRAC simulation (second row) reflects this overall pattern but with less sharp transitions, indicating a general agreement but with some differences in the precise

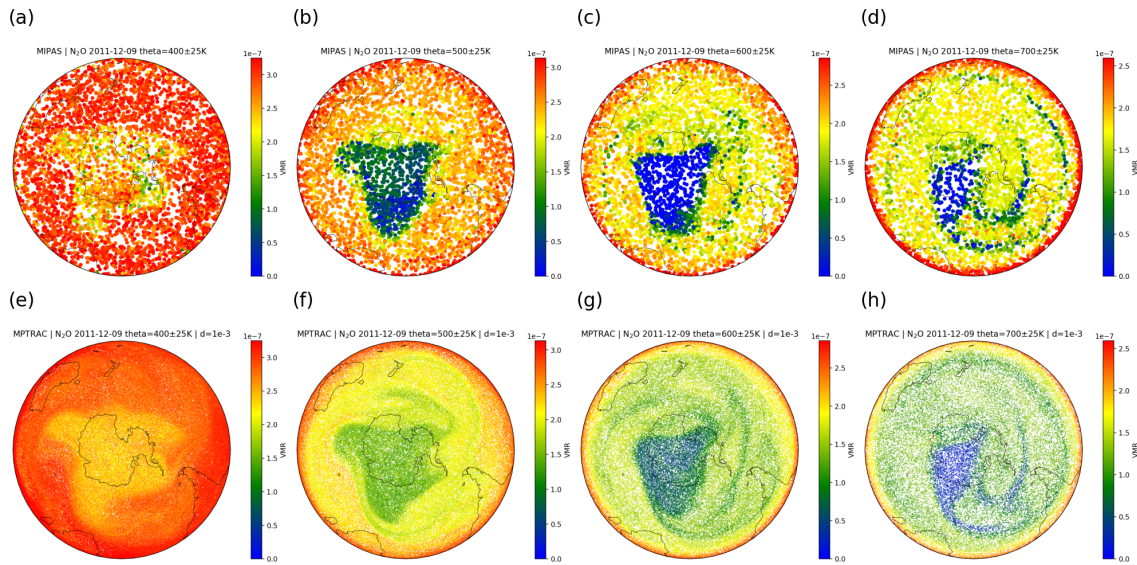


Figure 3.7: Comparison of MIPAS satellite-observed (first row) and MPTRAC model-simulated (second row) N_2O distributions at different potential temperature levels of 400, 500, 600 and 700 K.

spatial gradients. The simulation appears to slightly underestimate the central depletion in some layers.

For CFC-11 (Fig. 3.9), the MIPAS data (first row) also exhibit a distinct gradient, with higher concentrations at the edges and a pronounced drop towards the center, which becomes more evident at higher potential temperature levels. The MPTRAC simulation (second row) follows a similar pattern, though with a more diffuse transition between high and low concentration areas. The match between the observed and simulated data is reasonable, but there are slight discrepancies, especially at the higher potential temperature levels, where the simulated data show a more homogeneous distribution.

Fig. 3.10 shows the monthly mean concentration distribution of the MPTRAC-simulated and MIPAS-observed long-lived tracers in the 3rd, 6th, 9th and 12th month of 2011. Peak values are found in the tropical regions. Moving towards the poles, the tracer concentrations gradually decrease in both hemispheres. This is due to the Brewer-Dobson circulation, which transports air from the tropical lower atmosphere (where the tracer is abundant) upward and pole-ward, while tracers are gradually removed by photolysis reactions as it ascends. The color contour lines from the MPTRAC simulation closely follows the MIPAS observational data contours in black curves, especially the altitude that steep gradients occur. This suggests that MPTRAC successfully captures the broad distribution and transport of the long-lived tracers in the lower and middle atmosphere.

Overall, the simulated results consistently capture the broader patterns of high and low con-

3.2. Results

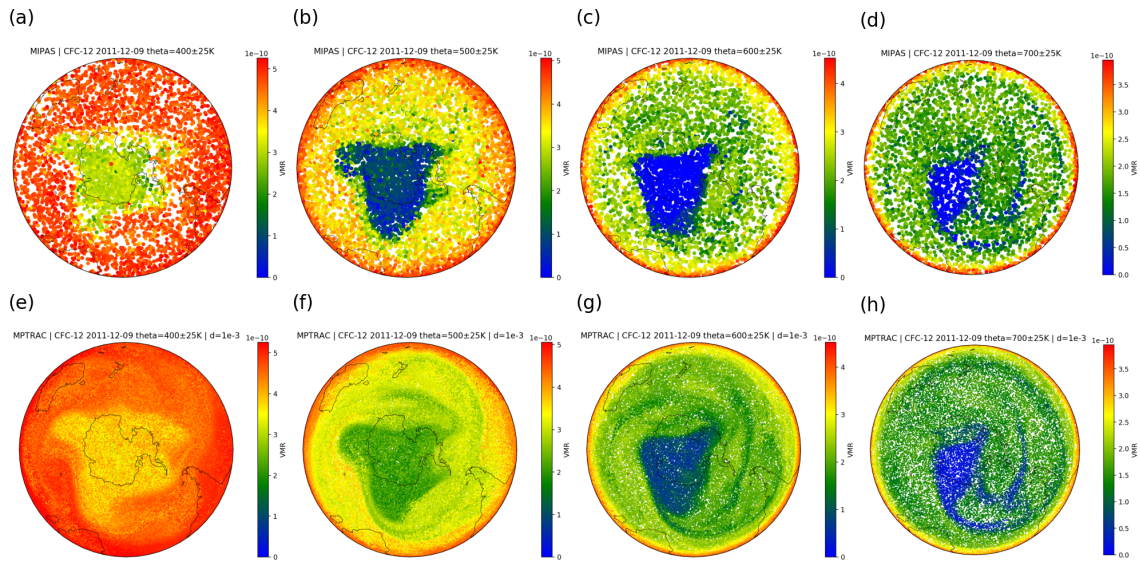


Figure 3.8: Comparison of MIPAS satellite-observed (first row) and MPTRAC model-simulated (second row) CFC-12 distributions at different potential temperature levels of 400, 500, 600 and 700 K.

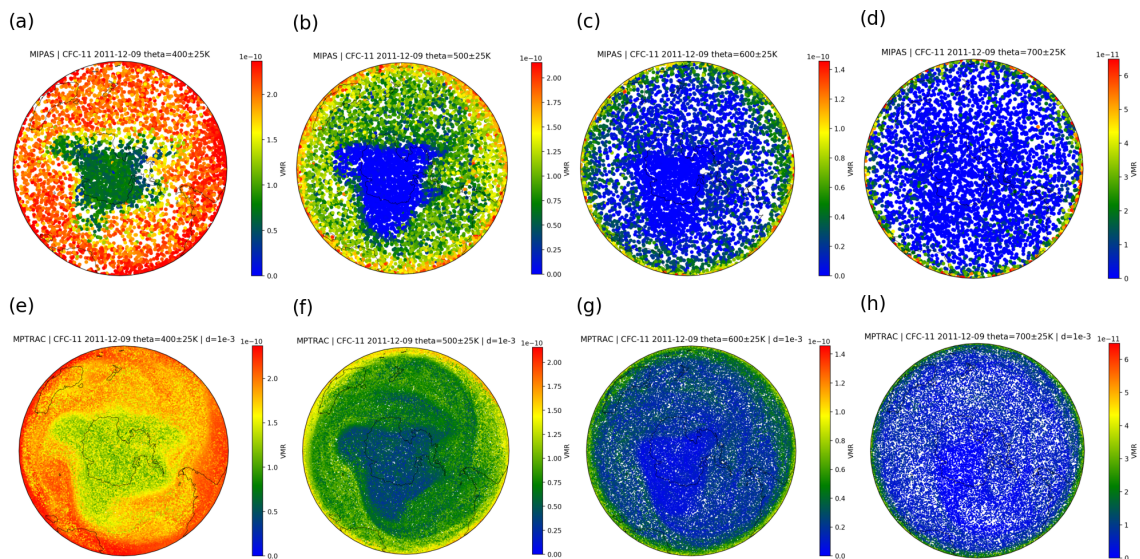


Figure 3.9: Comparison of MIPAS satellite-observed (first row) and MPTRAC model-simulated (second row) CFC-11 distributions at different potential temperature levels of 400, 500, 600 and 700 K.

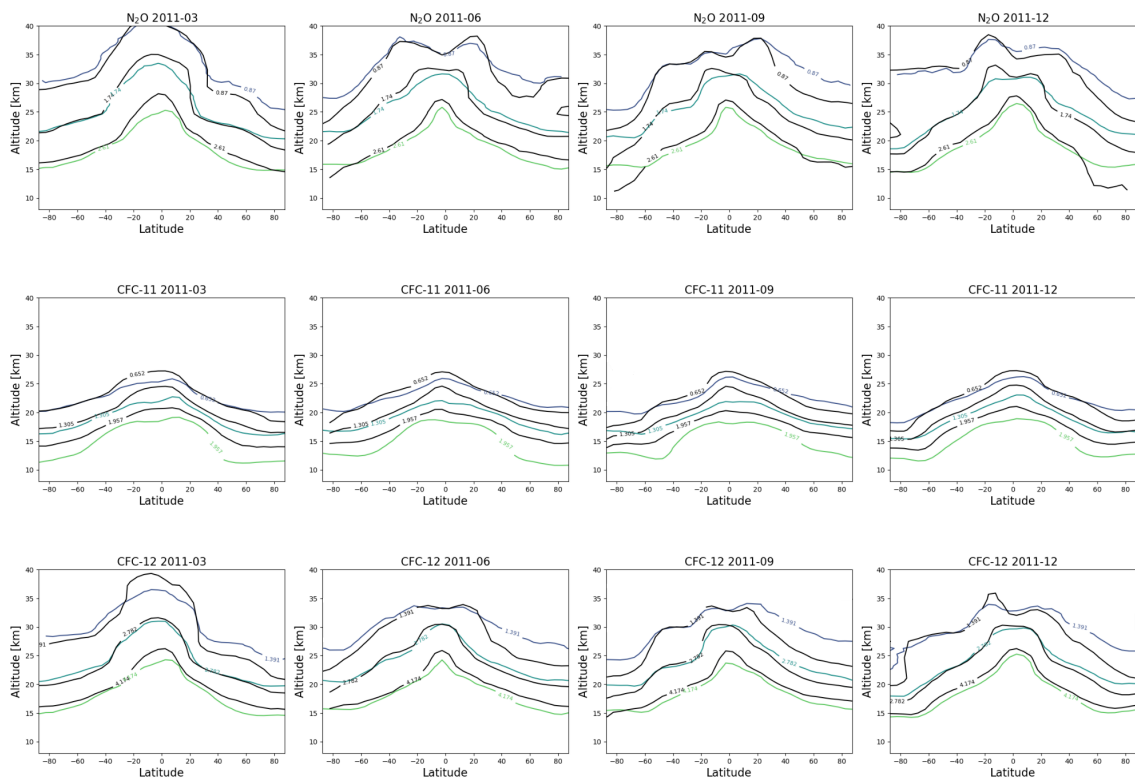


Figure 3.10: Contours of the MPTRAC-simulated and MIPAS-observed monthly mean long-lived tracer concentration distributions in 2011. The contour line value is the concentration in unit of 1×10^{-10} ppv. The black curves represent the MIPAS data and the color curves represent the MPTRAC simulated data.

centration regions, which validates the overall accuracy of the model. However, the finer details, such as the sharpness of concentration gradients, are less well-represented in the simulations. This could suggest that while the model is robust in capturing large-scale features, there may be uncertainties in its ability to simulate finer-scale dynamics or the impact of small-scale processes, such as mixing or localized chemical reactions.

3.3 Discussion

The application of a simplified explicit chemistry scheme, with photolysis data obtained from the CLaMS model, has proven to be highly effective in simulating long-lived tracers in the stratosphere. The close agreement between our model simulations and MIPAS satellite measurements, as well as the comparison with the SPARC Data Initiative climatologies, provides robust validation for both the photochemical and mixing schemes employed. The successful replication of long-lived tracer distributions indicates that the photochemical scheme accurately captures the key processes governing tracer behavior in the stratosphere. This agreement suggests that our simplified approach is sufficiently comprehensive for the accurate simulation of atmospheric chemistry, particularly for long-lived species.

The sensitivity tests conducted on the mixing parameter d have highlighted the importance of spatially and temporally variable mixing intensities in accurately simulating tracer distributions. As observed, different values of d are optimal depending on the latitude and altitude. For instance, stronger mixing is required in the tropical regions, especially in the stratosphere, to capture the observed variability, while in the polar regions, a lower mixing intensity provides a better match with observed data. These findings suggest that the mixing processes in the atmosphere are not uniform and that a dynamic adjustment of the mixing parameter could further enhance model accuracy.

Chapter 4

Case study of sulfur dioxide depletion from the Ambae eruption with the simplified explicit chemistry scheme

Ambae Island (15.39°S, 167.84°E), located in the South Pacific in Vanuatu, contributed the largest volcanic eruption in the year 2018. Among four main eruption phases during 2017 and 2018, the most intensive one in July 2018 injected at least 400 kt of SO₂ to a peak altitude of ~17 km (Moussallam et al., 2019). The volcanic SO₂ injected into the UT/LS formed aerosol particles which have a significant impact on atmospheric radiative forcing and global climate (Kloss et al., 2020; Malinina et al., 2021). Other cases, e. g., the Raikoke eruption in 2019 (Cai et al., 2022; de Leeuw et al., 2021), Kasatochi in August 2008, Sarychev in June 2009 (Wu et al., 2017), and Nabro in June 2011 (Höpfner et al., 2015) had lifetimes of about 14, 13, 24, and 32 days, and SO₂ mass releases of 1500, 2000, 1200, and 3650 kt, respectively. Compared to these cases, the Ambae case in July 2018 had a much shorter lifetime of ~4 days (Malinina et al., 2021). Local reports of acid rain suggest that the eruption was accompanied by strong wet deposition, which means that the released SO₂ encountered significant wet removal. As we aim to better understand and represent these processes in the MPTRAC model, we selected the Ambae eruption in July 2018 as a case study for this work.

4.1 Data and Method

4.1.1 Lagrangian transport of volcanic sulfur dioxide plume

For the simulation of the dispersion and depletion of SO₂ from the Ambae eruption, we applied the Lagrangian model MPTRAC described in Chapter. 2. The SO₂ mass of the air parcels is decomposed by gas phase OH oxidation, aqueous phase H₂O₂ oxidation and wet deposition

processes, instead of simply using an exponential decay with a fixed lifetime as applied in our earlier studies (Hoffmann et al., 2016; Heng et al., 2016; Wu et al., 2017). The detailed introduction of these module is presented in Sect. 2.2.

Due to the limited resolution of the global meteorological input data, neither ERA-Interim nor ERA5 are capable of resolving subgrid-scale convection processes. In MPTRAC, the extreme convection parameterization (Draxler and Hess, 1998; Gerbig et al., 2003) is used to represent the effects of convective up- and downdrafts being unresolved in the meteorological input data. The lifetime and depletion of SO₂ typically have a strong dependency on the atmospheric conditions at different altitudes. To test the impact of parameterized convection on the SO₂ transport simulations is part of the sensitivity tests presented in this work. The detailed description of the parameterization convection module is introduced in Section 2.1.

4.1.2 AIRS sulfur dioxide index

The Atmospheric InfraRed Sounder (AIRS) (Aumann et al., 2003) is an infrared spectrometer aboard the National Aeronautics and Space Administration's (NASA's) Aqua satellite. Aqua operates in a sun-synchronous low Earth orbit at orbit altitude of 705 km, providing nearly continuous measurements since September 2002. The AIRS instrument has across-track scanning capabilities. The swath width is 1780 km consisting of 90 footprints per scan with a footprint size of 13.5 km × 13.5 km at nadir. The measurements take place at about 01:30 and 13:30 local time for the descending and ascending sections of the orbits, respectively.

To detect the presence of volcanic SO₂ using the AIRS radiance measurements, an SO₂ index defined as the brightness temperature difference between 1407.2 cm⁻¹ and 1371.5 cm⁻¹ in the 7.3 μm SO₂ waveband is used (Hoffmann et al., 2014). The SO₂ index of Hoffmann et al. (2014) is most sensitive in the column density range of about 10 to 200 Dobson Units (DU) at altitudes of 8 to 13 km, which covers explosive volcanic eruptions with SO₂ injections into the UT/LS region. For SO₂ index values larger than 4 K, the SO₂ index is able to clearly detect volcanic plumes.

4.1.3 TROPOMI SO₂ measurements

The Tropospheric Monitoring Instrument (TROPOMI) (Veefkind et al., 2012) aboard the European Space Agency's Sentinel-5 Precursor satellite in a near-polar sun-synchronous orbit measures ultraviolet, visible, near-infrared, and shortwave infrared spectra at daytime. The TROPOMI instrument provides high spatial resolution with a pixel size of 7 km × 3.5 km over a swath width of

2600 km.

The TROPOMI products include volcanic SO₂ abundances for prescribed plume heights of 1, 7, and 15 km, based on a detection algorithm described by Brenot et al. (2014) which recognizes enhanced SO₂ values from volcanic eruptions as well as anthropogenic sources. In this study, we use the TROPOMI Level 2 product with a priori SO₂ profiles centered around 15 km (Theys et al., 2017) for the time period of 24 July to 11 August 2018 during the Ambae eruption.

The SO₂ total mass of the Ambae eruption was calculated using the TROPOMI data to compare with the simulation results. TROPOMI scans the Ambae region at around 00:00 UTC. A grid with resolution of 0.1° covering the longitude range from 120°E to 110°W and the latitude range from 50°S to 30°N was used to calculate the average mass of SO₂ in each grid box and to sum up the total mass. A filter of $\theta_{\text{SZA}} < 70^\circ$ and the detection flag to filter out anthropogenic SO₂ were used for the analysis of the TROPOMI volcanic SO₂ data product as described in (Theys et al., 2020). The derived SO₂ total mass curve is very similar to the result of Malinina et al. (2021).

4.2 Results

4.2.1 Baseline simulation

In this section, we present a baseline simulation of the dispersion and depletion of the volcanic SO₂ plume of the Ambae eruption in July 2018. In our initial tests, it was found that with only OH oxidation and wet deposition being considered, the simulations cannot fully explain the observed fast depletion of SO₂. Therefore, we newly implemented the process of in-cloud oxidation with H₂O₂. As the plume transport in this case occurs in a high-CAPE tropical region, the convection module was also included. A CAPE threshold of 1000 J kg⁻¹ was used to include moderate to strong subgrid-scale convection in the baseline simulation. The transport simulations with MPTRAC are driven by the ERA5 reanalysis. In the following sections, we will analyse the sensitivity of parameter choices for the above-mentioned chemistry and physics modules of MPTRAC with respect to the baseline simulation setup.

Figure 4.1a shows the SO₂ total mass curve calculated from the TROPOMI data. The total mass of SO₂ in the UT/LS region shows a strong increase on 26 July 2018, reaching a peak on 28 July, and decreases back to pre-eruption levels on 7 August 2018. According to different satellite instrument observations of the Support to Aviation Control Service (SACS, 2022), the volcanic plume is detected directly over the volcano from 26 to 27 July. The bulletin report of the Global Volcanism Program (GVP) (Krippner and Venzke, 2019) states that the main explosion

4.2. Results

occurred on 26 July and another two intense episodes, producing volcanic lightning, occurred on 27 July. Based on the different satellite measurements, observational reports as well as empirical testing, we initialized the MPTRAC baseline simulation for the Ambae case study by releasing 10^6 air parcels with a total mass of 450 kt starting on 26 July, 00:00 UTC over the time period of 36 h, assuming a Gaussian vertical profile with the maximum centered at 14 km and a full width at half maximum (FWHM) of 4 km. Although there are more advanced methods available to accurately estimate the timing and vertical distribution of volcanic emissions (Hoffmann et al., 2016; Wu et al., 2017; Cai et al., 2022), we did not apply these techniques in this study because these techniques do not fully account for SO_2 chemistry. This study focuses on testing the new and revised chemical and physical modules and on conducting sensitivity tests with respect to the parameter choices. As discussed below, the baseline simulation with constant emission rate and Gaussian vertical profile represents the Ambae case reasonably well so that meaningful testing and evaluation can be conducted.

To properly assess the total mass evolution and the SO_2 plume patterns of the baseline simulation, the model output was sampled at the exact time and location as the TROPOMI satellite footprints by calculating the column density of all parcels located within a horizontal search radius of 7 km, as introduced in Cai et al. (2022). Air parcels in data gaps of the satellite observations will be excluded in the evaluation of the simulation results. The model results are multiplied by an altitude-dependent sensitivity profile derived from TROPOMI averaging kernel data. The TROPOMI averaging kernel indicates full sensitivity above 10 km of altitude and the sensitivity only significantly decreases in the lower troposphere Cai et al. (2022). Since in this case most of the SO_2 injections and the plume height were located above 10 km, the inclusion of the averaging kernel does not significantly change the model results. A lower threshold of 1 Dobson units (DU) was applied to both the simulation data and the TROPOMI observations to eliminate the effects of noise. With this approach, the sample output of the model can be quantitatively analyzed and compared with the TROPOMI satellite observations. As shown in Fig. 4.1a, the MPTRAC baseline simulation yields good agreement with the total mass curve derived from the TROPOMI data. The overall SO_2 lifetime from the simulation is quite similar to the observational data.

Figure 4.1b shows the relative mass loss relative to the total emissions over time with regard to each module. At the end of the simulation, OH chemistry, H_2O_2 chemistry and wet deposition lead to a mass loss of 45%, 14%, and 21% of the total mass burden, respectively. The remaining mass loss in Fig. 4.1a is due to air parcels leaving the study region or having SO_2 mass below the filtering threshold so that they are not accounted for in the mass budget anymore. The loss rates

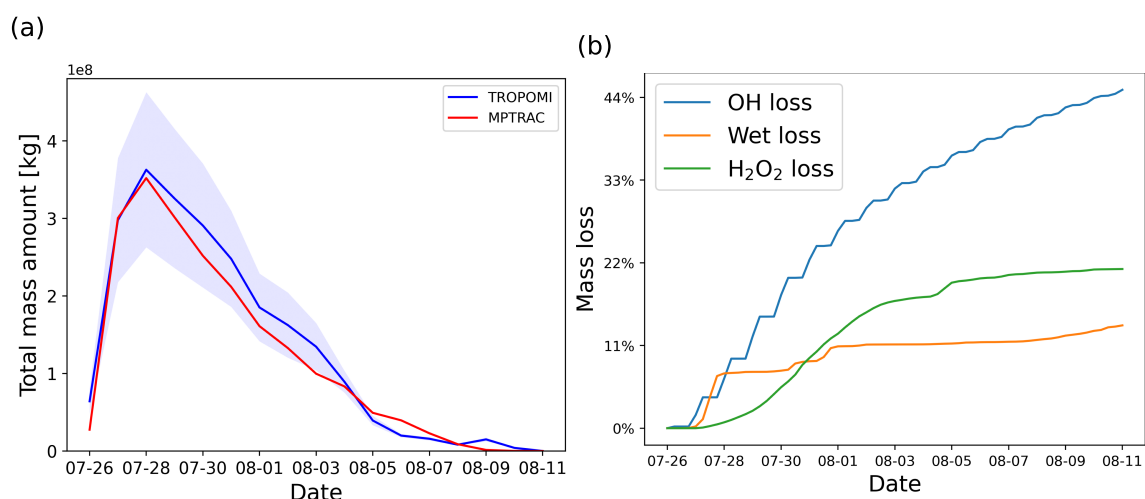


Figure 4.1: Observed (TROPOMI) and simulated (MPTRAC) SO₂ total mass curve (a) and mass loss (b) of the July 2018 Ambae eruption as a function of time. The blue shading represents the total error of the TROPOMI observations, combining random and systematic error components.

due to in-cloud removal processes, including wet deposition and the aqueous phase H₂O₂ oxidation, strongly depend on the location of the volcanic plume relative to the cloud fields. The loss due to OH oxidation is a step-shaped curve due to the diurnal variations of the OH concentration, leading to a faster loss rate at daytime and nearly zero loss at nighttime. Simulations using an OH field with diurnal variations will vary by 0.7% compared to using an OH field without diurnal variations. Differences are relatively low in this case because the observations occur at about 13:00 local time. Overall, the diurnal variations of the OH field have little effect on the SO₂ decay rates over the entire simulation period, because the observational time scale is over several days and the diurnal variations are averaging out.

Figure 4.2 shows comparisons of horizontal maps of the SO₂ plume from the baseline simulation with AIRS and TROPOMI measurements, respectively. The bulk of the Ambae plume moved eastwards, and the moving speed is faster at lower altitudes. A small plume at heights of 10 to 12 km moved northwards after 28 July at 160°W to 180°W, encountering strong wet deposition. The model results match the satellite observations qualitatively well with similar location and shape of the plume. At the end of the simulation the part of the plume below the cloud top is almost depleted and the remaining part of the plume above the cloud top somewhat shows deviations from the observations due to the unpolished temporal and vertical variations of the emission estimates. Nevertheless, we consider the baseline simulation in its present form to be suitable for further evaluation and sensitivity tests.

4.2. Results

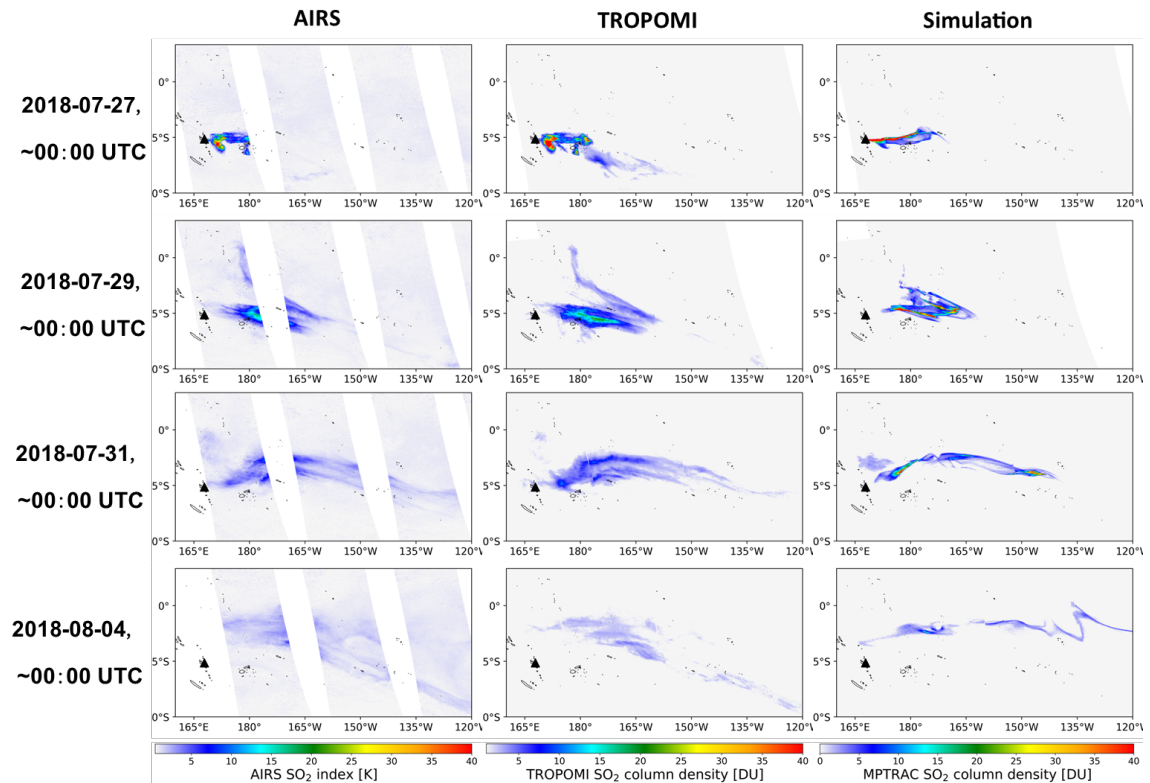


Figure 4.2: Evolution of the Ambae SO_2 plume in AIRS SO_2 observations (a) as well as column densities from TROPOMI observations (b) and MPTRAC simulation (c). The time of the satellite observations shown here was restricted to ± 3 h around 00:00 UTC. The black triangle shows the location of Ambae island. MPTRAC simulation results have been sampled on the TROPOMI footprints.

4.2.2 Sensitivity test on SO_2 release height

In this section, a series of simulations with air parcels released at different altitudes is presented to show the sensitivity of the plume injection height on the evolution of SO_2 total mass burden. The tests use different release heights centered at 11, 13, 15, 17, and 19 km with 2 km wide uniform vertical distribution. The convection module was not activated in this test to avoid vertical mixing of air parcels down to the surface during the simulations. As shown in Fig. 4.3, the SO_2 decay rate has an obvious dependency on release height. Releasing the volcanic SO_2 at different heights leads to rather different horizontal spread and different mass loss due to wet deposition, depending on whether the SO_2 plume encounters cloud regions or not.

As shown in Fig. 4.3b, the mass loss due to wet deposition shows particularly high sensitivity to the release height. Wet deposition occurs mainly on 27 to 28 July when releasing air parcels at altitudes below 14 km, while most of the wet deposition mass loss occurs around 1 August when releasing above 14 km. Almost no wet deposition occurs above 18 km because it is above

the tropopause and the maximum cloud top height. Aqueous phase H_2O_2 chemistry is most active at below 14 km, and has a strong sensitivity on release height, while above 14 km the H_2O_2 chemistry is very weak. The OH gas phase oxidation does not show a clear correlation with release height, with contributions to mass loss ranging from 30% to 60% of the total mass during the simulation. However, note that the OH concentrations and temperature- and pressure-dependent rate coefficients of the OH oxidation are not linearly increasing with altitude (compare Fig. 4.6) over heights from 10 to 20 km. Above 15 km, the OH oxidation rate decreases with height, while below 15 km, the decay rate is controlled mainly by in-cloud removal and the OH oxidation rate quickly decreases.

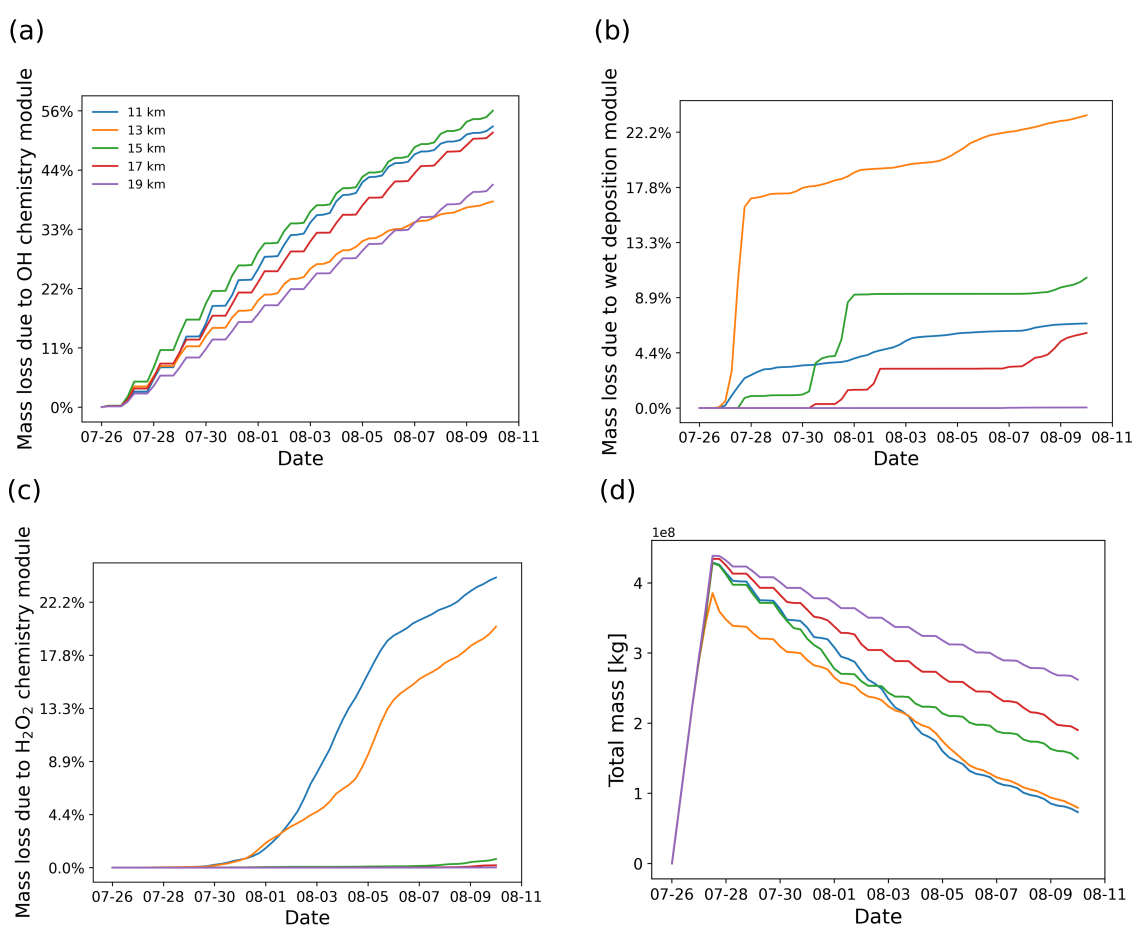


Figure 4.3: SO_2 mass loss relative to the total mass (in percent) due to OH chemistry (a), wet deposition (b), and H_2O_2 chemistry (c) as well as total mass curves (d) derived from simulations with different release heights centered at 11, 13, 15, 17 and 19 km.

Figures 4.4 and 4.5 show the cloud top height and CAPE distributions derived from the ERA5 meteorological data as well as the particles released at different altitudes, clearly indicating which part of the plume is affected by wet removal and sub-grid scale convection, as distinguished by

4.2. Results

yellow and blue color. The plume released at the location of Ambae Island is transported to a region with high CAPE values and abundant clouds. The wet removal and subgrid-scale convection mainly take effect at altitudes below 15 km. The maximum CAPE values range approximately from 1000 to 1600 J kg⁻¹. In simulations with higher injection altitudes, the air parcels are transported mainly above the cloud top and are barely influenced by wet deposition and convection.

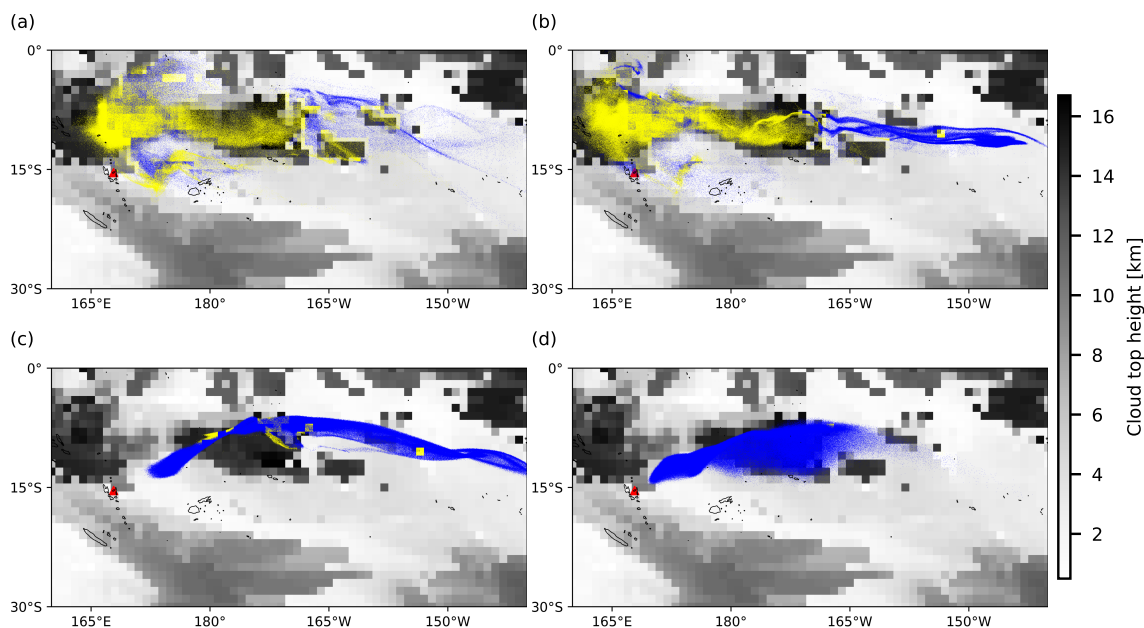


Figure 4.4: Background images represent the distributions of ERA5 cloud top height on 31 July 2018, 00:00 UTC. Dots represent air parcels released at altitudes of (a) 11 km, (b) 13 km, (c) 15 km, and (d) 17 km. A yellow dot indicates that the air parcel is below the cloud top height, triggering the wet deposition module, while a blue dot represents the opposite.

4.2.3 Sensitivity tests on OH chemistry

The SO₂ decay rate in the OH chemistry module is calculated by Eq. (2.15), which considers the temperature- and pressure-dependent reaction rate k_f and the OH concentration. The OH concentration is obtained from predefined monthly mean zonal mean data and the solar zenith angle correction to account for day- and nighttime conditions. The OH data used by default in MPTRAC is the monthly mean zonal mean climatology from Pommrich et al. (2014), which was calculated using the CLaMS model chemistry scheme. As another alternative, the CAMS global reanalysis provides 3-hourly OH data with a resolution of 0.75°x0.75°. To reduce memory needs and maintain consistency with the CLaMS data approach, the CAMS data are also converted into monthly mean zonal mean data. To verify the impact of inter-annual differences, we compared the results between the simulations with CAMS reanalysis data for the years 2005 (matching the

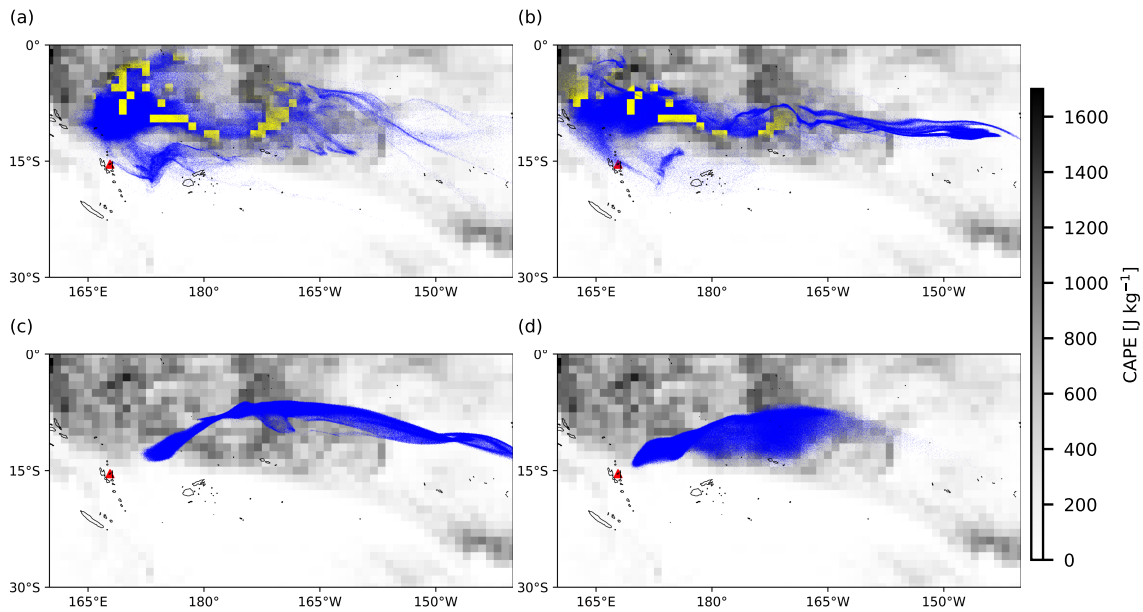


Figure 4.5: Same as Fig. 4.4, but background images represent the distribution of ERA5 CAPE values on 31 July 2018, 00:00 UTC. Yellow dots indicate air parcels below the equilibrium level and local CAPE values larger than 1000 J kg^{-1} , triggering the convection module, while blue dots represent the opposite.

CLaMS data) and 2018 (matching the Ambae eruption), respectively. For another test, simulations with regional CAMS OH data extracted from the longitude range from 160°E to 140°W are compared with global data.

Figure 4.6 shows average vertical profiles of the different OH data sets at tropical latitudes (from 23.5°S to 23.5°N). The CLaMS OH data (Pommrich et al., 2014), calculated using methane and ozone data taken from the HALOE climatology for the year 2005 (Grooß et al., 2005), are compared with the CAMS OH reanalysis data for the years 2005 and 2018, respectively. The differences in the CAMS mean profiles between 2005 and 2018 are found to be negligible. Comparing the CLaMS and CAMS OH data, these two datasets show similar concentrations in the troposphere while in the stratosphere, CLaMS OH concentrations are much larger than CAMS OH concentrations. To further evaluate the OH fields of the climatologies, we compared them to several NASA in-situ OH measurements in the troposphere at similar altitudes, solar zenith angles, and time periods and also to Microwave Limb Sounder (MLS) satellite data in the stratosphere. Both, CLaMS and CAMS data showed good agreement with the in-situ measurements in the troposphere. At altitudes above 20 km, CLaMS data show much better agreement with MLS observations than the CAMS reanalysis. Further details of the comparison are presented in the appendix chapter A.

As shown in Fig. 4.7, the inter-annual differences in the CAMS OH data are negligible (~ 1

4.2. Results

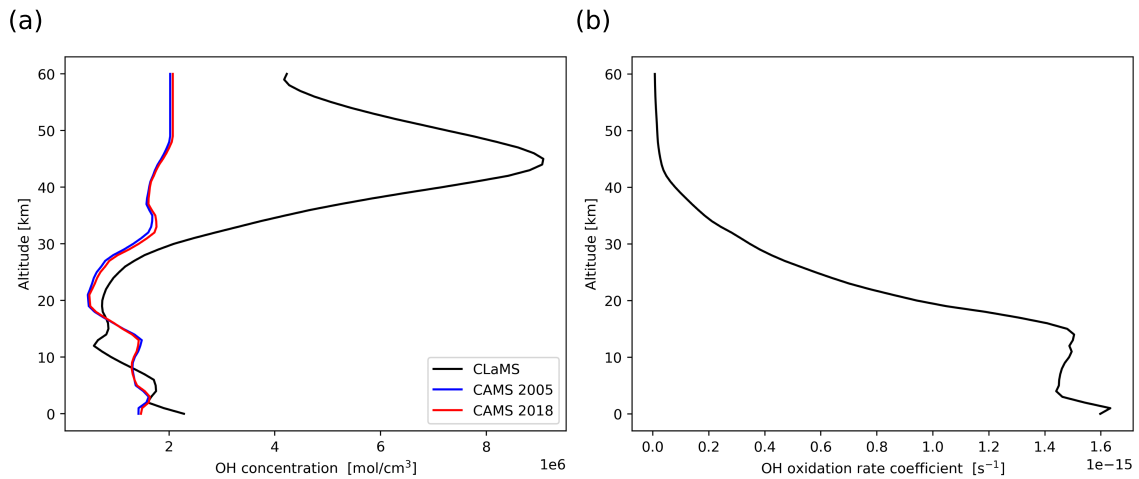


Figure 4.6: Vertical profiles of (a) OH concentrations over the tropics retrieved from CLaMS and CAMS climatology data, respectively, on 26 July 2018, 00:00 UTC and (b) OH oxidation rate coefficients at the same time.

percentage point, pp). The differences between simulations with CAMS and CLaMS global OH data are ~ 3 pp. The simulation with regional CAMS OH data for the location of the eruption has ~ 4 pp difference compared with the global CAMS data. Overall, the inter-annual and regional differences of the OH datasets have a small influence on the amount of OH oxidation (less than 5 pp in this case), which suggests that using a monthly mean zonal mean climatology is a reasonable approach for modeling the OH loss of SO_2 in the UT/LS region.

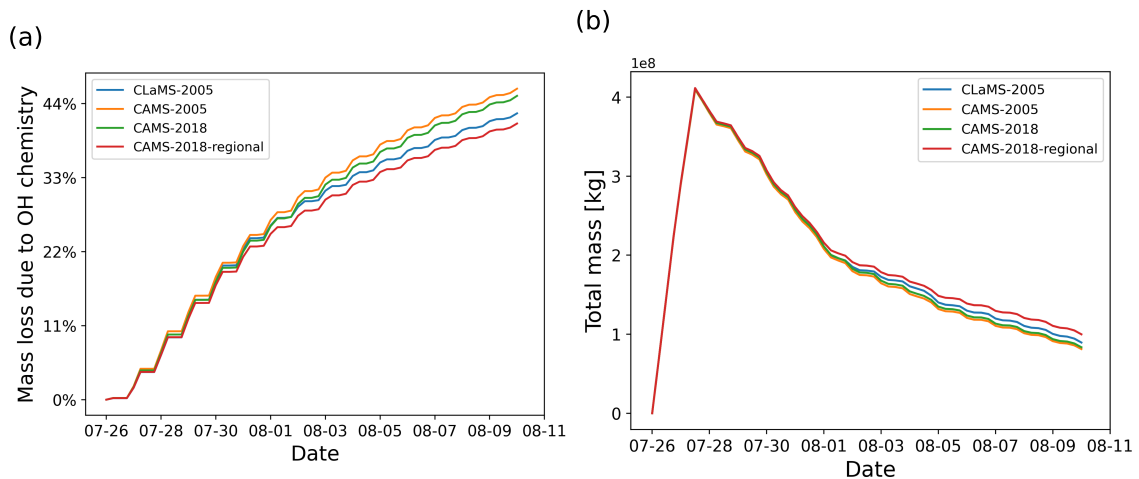


Figure 4.7: SO_2 mass loss relative to total mass (in percent) due to the OH chemistry module (a) and total mass curves (b) for simulations with different OH datasets, including CLaMS data in 2005, CAMS data in 2005 and 2018, and CAMS regional data in 2018 (see text for details).

4.2.4 Sensitivity tests on wet deposition

In the Ambae case study, the wet removal in clouds plays an important role in depleting SO_2 since the main plume passes through a cloud region. As introduced in Sect. 2.2.1, in-cloud wet deposition is handled as a rain-out process, which depends on the partition ratio of SO_2 in the cloud droplets and the precipitation rate. The partition ratio of SO_2 in liquid phase is defined with an effective Henry's law constant, depending on the assumed pH value. Here, we conducted a series of simulations to test the sensitivity to pH values in the range of 3 to 5, along with a comparison with the NAME wet deposition scheme (Webster and Thomson, 2014). As expected, higher cloud pH values lead to stronger wet deposition. The simulation with wet deposition according to the NAME scheme shows a similar deposition to the baseline simulation with the equilibrium scheme at pH 4 to 4.5. The difference between the two schemes is further reflected in the sensitivity to convection, which will be discussed in Sect. 4.2.5

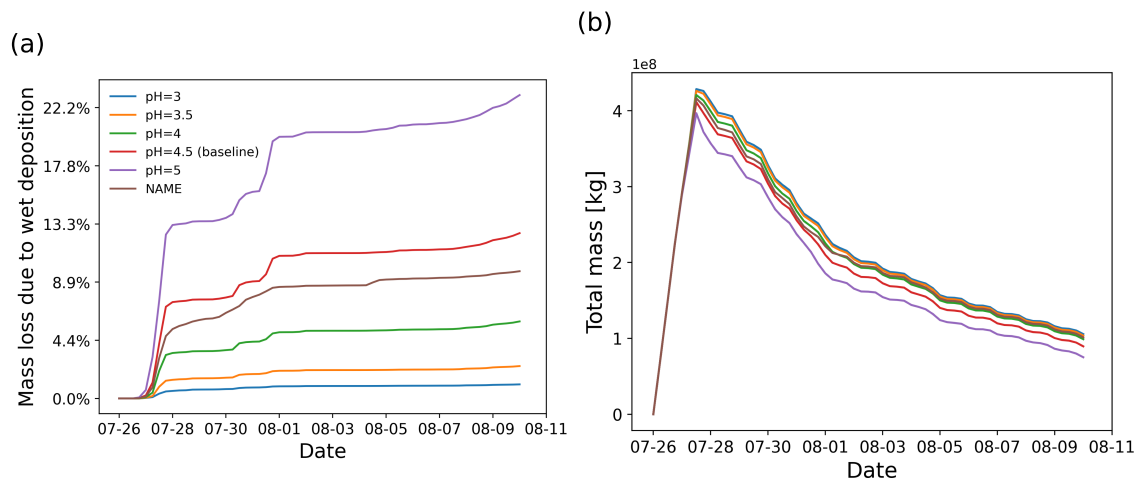


Figure 4.8: SO_2 mass loss relative to total mass (in percent) due to the wet deposition module (a) and total mass curves (b), derived from simulations with different pH values in the wet deposition module and comparing with the wet deposition scheme of the NAME model.

The retention ratio represents the solute species in the ice phase versus that in the liquid hydrometeor. The retention coefficient may vary depending on temperature, pH, ventilation rate, accretion rate, and impact velocity (Stuart and Jacobson, 2006). Laboratory studies on the retention ratio of SO_2 suggest a range from 1% to 60% (Iribarne et al., 1983; Lamb and Blumenstein, 1987; Iribarne et al., 1990). As introduced in Sect. 2.2.1, a retention coefficient dependent on temperature is applied to model the differences of wet deposition in ice and liquid clouds. Figure 4.9 shows the SO_2 mass loss curves of simulations given different retention ratios in the range of 0.01 to 1. In this case, most of the wet deposition occurs in ice clouds leading to a strong

dependency on the retention ratio.

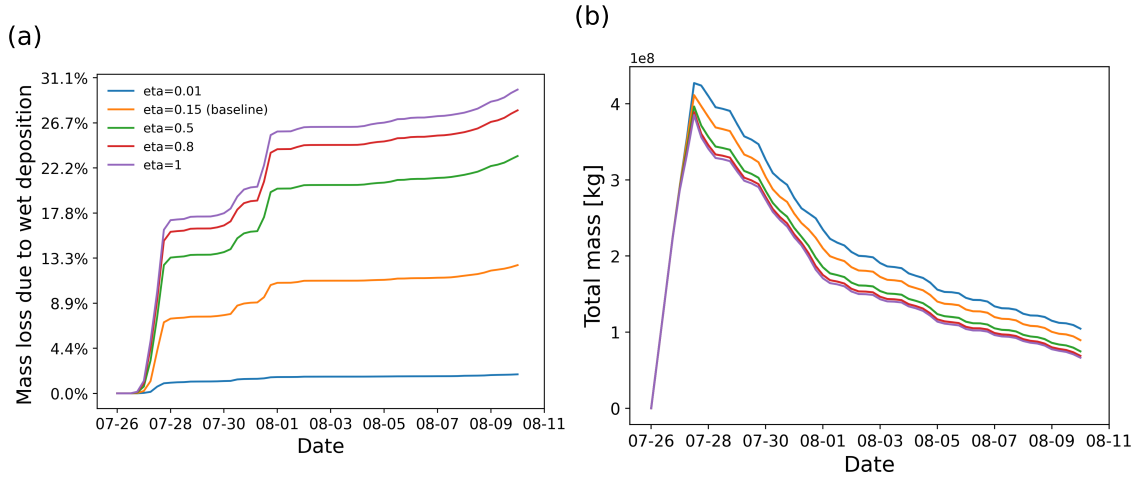


Figure 4.9: SO₂ mass loss relative to the total mass (in percent) due the wet deposition module(a) and total mass burden evolution (b), derived from different simulations with different retention ratios settings in the wet deposition module.

4.2.5 Impact of the extreme convection parameterization

Due to better spatio-temporal resolution, the ERA5 meteorological data provide more accurate information than ERA-Interim to resolve mesoscale features (Hoffmann et al., 2019). However, convective up- and downdrafts are still underrepresented in the ERA5 data. In MPTRAC, the extreme convection parameterization is applied to represent the effects of unresolved convection in the meteorological input data. In convective columns, the convection module will randomly redistribute the air parcels between the surface and the equilibrium level, if CAPE exceeds a given threshold CAPE₀. As shown in Fig. 4.5, the SO₂ plume released by the Ambae volcanic eruption was transported to a high CAPE region which makes it a valuable case to study the potential effects of unresolved convection. In this section, the effects of parameterized convection for different thresholds CAPE₀ will be discussed.

Figure 4.10 shows the vertical distributions of the SO₂ mass of the Ambae plume for different thresholds CAPE₀ from 0 to 2000 J kg⁻¹. The case of CAPE₀ being zero represents the extreme case in which convection occurs everywhere below the equilibrium level where CAPE is present. For CAPE₀ larger than 1000 J kg⁻¹, the parameterized convection is restricted to represent moderate to strong convective events only. There is almost no additional convection for CAPE₀ larger than 2000 J kg⁻¹ compared to the case without parameterized convection. When applying a larger CAPE₀, more air parcels will be transported to altitudes below the equilibrium level (~14 km).

Figure 4.11 shows the impact of parameterized convection on mass loss in the SO_2 transport simulations for the Ambae case. The largest sensitivity is found for the H_2O_2 oxidation, while OH oxidation and wet deposition show little difference. This is because some air parcels are transported to heights below 14 km where the H_2O_2 oxidation is most active. The H_2O_2 chemistry is much more sensitive to height than the OH chemistry and wet deposition at altitudes where convection occurs (see Sect. 4.2.2). Regarding the mass evolution, the effect of the convection module enhances the depletion of SO_2 below the cloud top. At the end of the simulation, most of the remaining SO_2 is above the cloud top where the convection module has no effect.

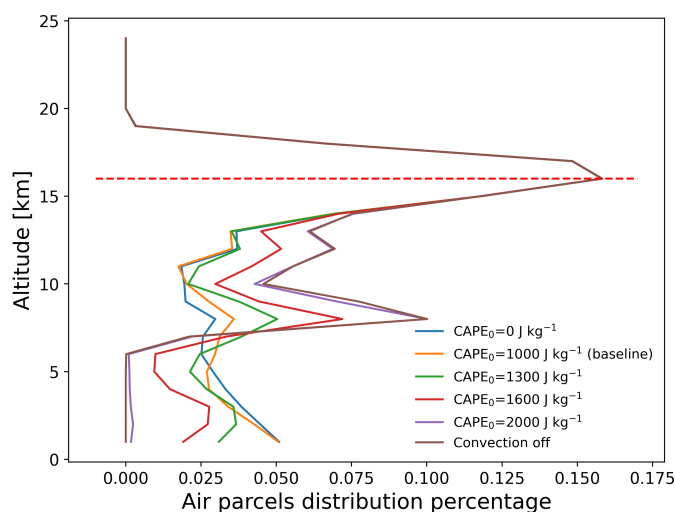


Figure 4.10: Vertical distribution of total SO_2 mass of the air parcels on 1 August 2018, 00:00 UTC from simulations with different CAPE thresholds. The red dashed line indicates the ERA5 thermal tropopause height over the Ambae region (Hoffmann and Spang, 2022).

4.3 Discussion

We present recent improvements of the chemical and physical modules in the Lagrangian transport model MPTRAC for simulating the dispersion and depletion of SO_2 from volcanic eruptions. The improved modules include gas phase OH oxidation, aqueous phase H_2O_2 oxidation, wet deposition, and parameterized convection. In a case study, the modules are applied for simulations of the SO_2 plume evolution of the Ambae eruption in July 2018. We present a baseline simulation, in which the modeled mass evolution shows a good match with TROPOMI satellite observations.

In our simulations, the implementation of wet deposition and H_2O_2 oxidation significantly decreased the lifetime of SO_2 in clouds. Gas phase oxidation by OH, aqueous phase oxidation by H_2O_2 , and wet deposition remove about 45%, 14%, and 21% of the total SO_2 mass burden, re-

4.3. Discussion

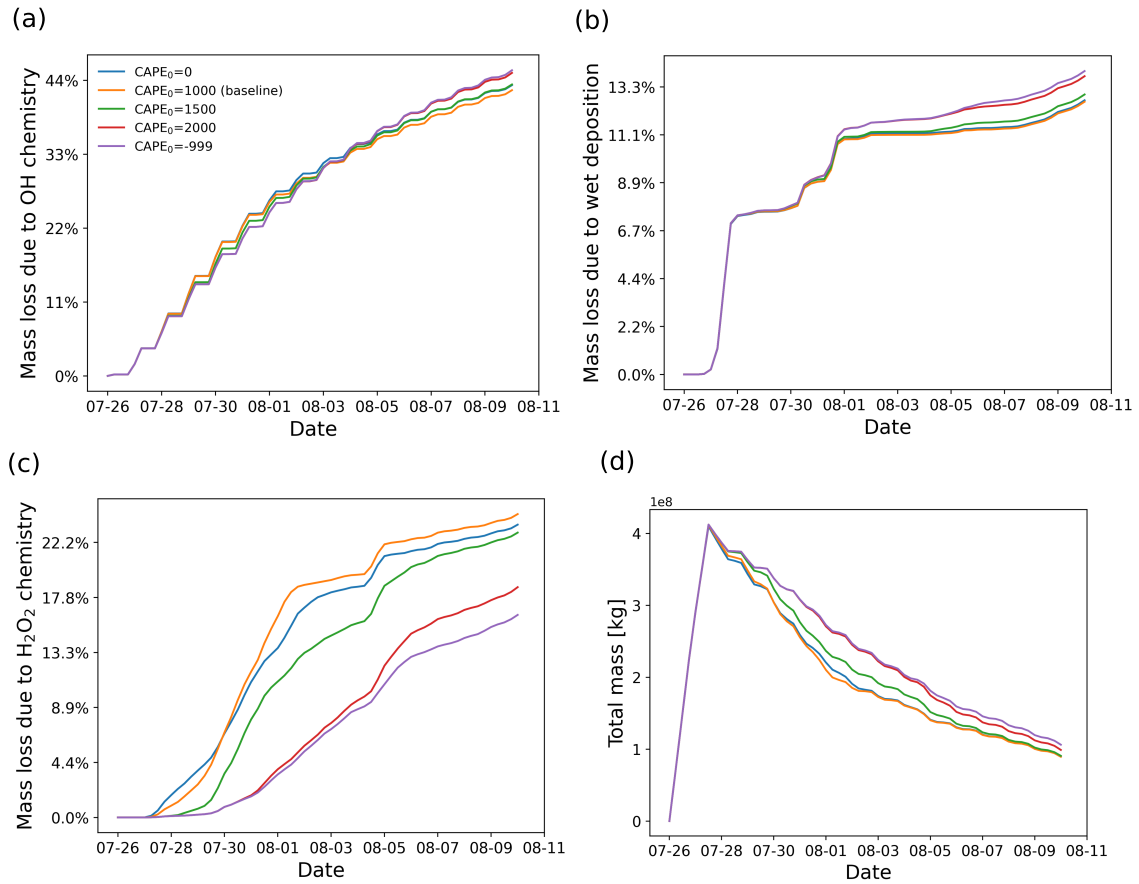


Figure 4.11: Same as Fig. 4.3, but derived from simulations with different CAPE thresholds in the convection module.

spectively, over a simulation time period of 15 days. Based on the baseline simulation, a series of sensitivity tests was conducted by tuning various control parameters of the modules to better understand the impacts of the chemical and physical processes on SO₂ dispersion. Initially, we tested the sensitivity on the assumed injection height of the SO₂ plume. The SO₂ plume undergoes much faster depletion below 14 km in clouds than in the dry atmosphere because rain-out processes and aqueous phase oxidation are bound to the presence of clouds. Variations of cloud distributions and vertical wind shear lead to rather different amount of wet deposition and aqueous phase oxidation for different injection heights.

For the OH chemistry module, different OH monthly mean zonal mean concentration datasets have been tested. It was found that the differences in mass loss between different OH datasets (CAM5 versus CLaMS, regional versus global, and year 2005 versus 2018) are limited (less than 5 pp of the total mass). Using a monthly mean zonal mean climatology of OH for simulating SO₂ mass loss over time is considered a suitable approach for transport simulations covering the UT/LS region. For wet deposition, an analytic solution derived for the rain-out process ac-

According to Henry's law is considered in clouds. The assumed pH value of the effective Henry's Law constant for SO_2 has a strong effect on the amount of wet removal of SO_2 . Compared with the wet deposition scheme with a scavenging coefficient formula applied in the UK Met Office's NAME model, our simulation at an assumed pH value of 4.5 yields a similar level of wet deposition. The impact of the retention ratio of the soluble gas in ice clouds is also discussed. Due to the low temperatures in the UT/LS region, most of the regions affected by the Ambae eruption are covered with ice clouds. Therefore, the amount of wet deposition strongly depends on the assumed retention ratio. For H_2O_2 chemistry in the aqueous phase, the impact of cloud cover has been tested. By tuning the CAPE threshold used in the extreme convection parameterization, the vertical distribution of the SO_2 plume might be strongly altered, which in turn will impact the depletion of SO_2 . It is found that aqueous phase oxidation via H_2O_2 is mostly influenced, whereas wet deposition and OH oxidation are not so sensitive to the vertical redistribution of the air parcels due to the parameterized convection.

In this study, we improved the Lagrangian transport simulations of volcanic SO_2 with MPTRAC by implementing more realistic physical and chemical process representation instead of using an exponential decay law with a fixed lifetime as in our previous studies. However, the refinements on the modeled loss processes lead to a high sensitivity to the release vertical profile and cloud abundance. The backward trajectory method developed to estimate time- and height-resolved SO_2 emissions with MPTRAC (Hoffmann et al., 2016; Wu et al., 2017) is currently incapable of taking into account the additional complexity of the revised chemistry and wet deposition parameterizations. In future work, we plan to implement a more advanced inverse modeling techniques in MPTRAC to reconstruct the initial SO_2 injections of volcanic eruptions, which can take the model improvements described here into account.

The representation of volcanic SO_2 depletion in different atmospheric conditions above and below the cloud top in the current MPTRAC scheme considers first-order loss processes to estimate rate coefficients and lifetimes. In reality, the chemical processes affecting the lifetime of volcanic SO_2 may be more complicated. Large-scale emissions of volcanic SO_2 into the atmosphere will reduce the abundance of atmospheric oxides. The scattering and reduction of solar radiation by ash and other aerosol particles will reduce the photochemical regeneration of the oxides. The linear simplification in this explicit scheme may lead to overestimation of the SO_2 chemical decomposition. In the next section, we will discuss the difference between the two chemistry schemes for volcanic SO_2 decay. The simplified explicit scheme and the implicit scheme will be compared and analyzed.

Chapter 5

Case study of sulfur dioxide depletion from the Raikoke eruption with the implicit chemistry scheme

The main objective of this case study is to introduce and assess a newly developed chemistry scheme with an implicit chemistry solver in the MPTRAC model, which improves global chemistry-transport simulations of volcanic SO₂ and allows for estimating the volcanic emission sources. We propose a small chemical mechanism with 12 species and 31 reactions to model the production and loss of OH, HO₂ and H₂O₂ in the UT/LS region, including reactions among O(¹D), O(³P), H, OH, HO₂, O₃ and H₂O, together with reactions of SO₂ with OH in the gas phase and oxidation with H₂O₂ in the aqueous phase. The aim is to model the dynamic OH and H₂O₂ fields as SO₂ oxidants to more realistically simulate and better represent the chemical lifetime of volcanic SO₂ in the UT/LS region. The chemical solver was built using the Kinetic Preprocessor (KPP) software package (Damian et al., 2002; Sandu and Sander, 2006). The KPP software provides a framework to automatically generate a Rosenbrock integrator for solving the stiff ordinary differential equations with specification of a chemical mechanism, including the chemical equations, species, and rate coefficients.

In this case study, we conducted simulations of the June 2019 Raikoke volcanic eruption to compare and verify the modeled lifetime of the SO₂ emissions with TROPOspheric Monitoring Instrument (TROPOMI) satellite measurements. The Raikoke (48.17°N, 152.15°E) eruption was a notable event that has been discussed in the literature to some larger extent. The eruption on 21-22 June was characterized by a series of explosive events that emitted SO₂ and volcanic ash into the lower stratosphere, impacting the stratospheric aerosol layer (Gorkavyi et al., 2021; Kloss et al., 2021). Cai et al. (2022) used MPTRAC to estimate the SO₂ emissions and to investigate the effects of the injection height and time and of the diffusion parameters. With an estimated amount

of (1.5 ± 0.2) Tg of SO_2 , the eruption was notable for being the largest SO_2 injection into the upper troposphere and lower stratosphere since the 2011 Nabro eruption (Cai et al., 2022). de Leeuw et al. (2021) discuss the transport and chemical evolution of SO_2 emissions resulting from the 2019 Raikoke eruption, offering a comprehensive comparison between NAME model simulations and TROPOMI observations.

5.1 Model initialization

In an earlier study, Cai et al. (2022) investigated the time- and height-resolved SO_2 injection parameters of the 2019 Raikoke eruption based on a backward-trajectory approach and SO_2 retrievals from TROPOMI observations. In this work, we used the same estimates of the SO_2 injections as Cai et al. (2022) to initialize the release of air parcels in the transport simulations. A total SO_2 mass of 1.6 Tg was distributed over 10^6 air parcels. The main injection peak occurs between June 21 and 22, 2019, at altitudes between 5 and 15 km. The vertical profile of the SO_2 injection rates is shown in Fig. 5.1. Two numerical experiments were conducted with MPTRAC to compare the results of the linear explicit and non-linear implicit chemistry solutions. Here, the simplified explicit approximation scheme considering the gas phase oxidation and aqueous phase oxidation with climatological background OH and H_2O_2 fields are similar to the Ambae case study in the Chapter 4. The KPP implicit solution considers the same reactions of SO_2 , but the OH and H_2O_2 fields are modeled with the chemical mechanism listed in Table 2.1.

The simulated SO_2 plume evolution with the KPP implicit chemistry scheme is compared with TROPOMI observations in Figs. 5.2 and 5.3. From these comparisons, it is found that the MPTRAC model captures the overall distribution and movement of the volcanic SO_2 plume well during the first 10 days. Both the TROPOMI retrievals and the MPTRAC simulations show that the SO_2 plume continuously spreads over a larger area, with significant eastward motion and following the cyclonic flows. Similar to the studies of Cai et al. (2022) and de Leeuw et al. (2021), the model results begin to lose the ability to capture some structural features of the observed SO_2 distributions and show a stronger diffusion effect due to the limited resolution of the meteorological data after the first few days, but the overall propagation direction and the dispersion regions still remain consistent. In this study, we will focus on the analysis of the volcanic SO_2 mass evolution and chemical lifetime based on this baseline simulation.

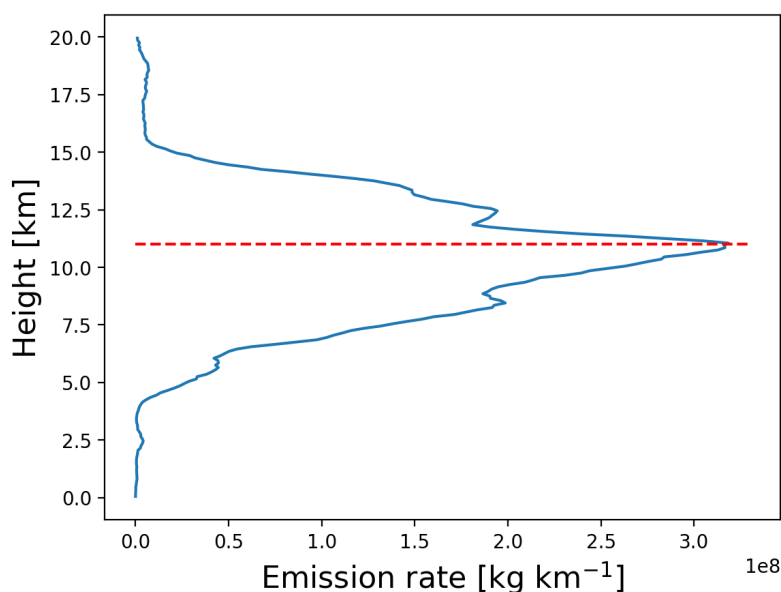


Figure 5.1: Vertical profile of SO₂ injections of the Raikoke eruption as estimated by Cai et al. (2022). The red line represents the tropopause height at the location of the volcano.

5.2 Results

5.2.1 Sulfur dioxide chemical lifetime analysis

The time evolution of the total SO₂ mass burden of the 2019 Raikoke eruption from the MPTRAC simulations and TROPOMI observations is shown in Fig. 5.4. The total mass burdens from the model and the observations were obtained by integrating the SO₂ column densities on a $0.1^\circ \times 0.1^\circ$ horizontal grid. For comparison with the satellite data, the grid output of the model was sampled with a lower detection limit of 0.35 DU and weighted by the mean kernel function of the TROPOMI observations to reduce the impact of noise and other uncertainties and to account for the vertical sensitivity of the measurements. The SO₂ lifetime modeled with the implicit KPP solution is about 1.6 times longer than that of the simplified explicit approximation. This can be seen from the vertical profile of the e-folding lifetime in Fig. 5.5.

The lifetime profile obtained with the KPP implicit solution indicates that the SO₂ has much longer lifetimes at higher altitudes. The lifetime is typically within a few hours to several days below 5 km of altitude, while it exceeds 10 to 100 days above 5 km of altitude. Due to the frequent presence of clouds in the lower and middle troposphere, SO₂ is taken up into the liquid phase and decays rapidly due to cloud phase oxidation with H₂O₂ and wet deposition, leading to the shorter lifetime compared with the stratosphere. The vertical lifetime profile of the implicit KPP scheme shows a peak in the stratosphere that is not found in the explicit scheme. This is attributed

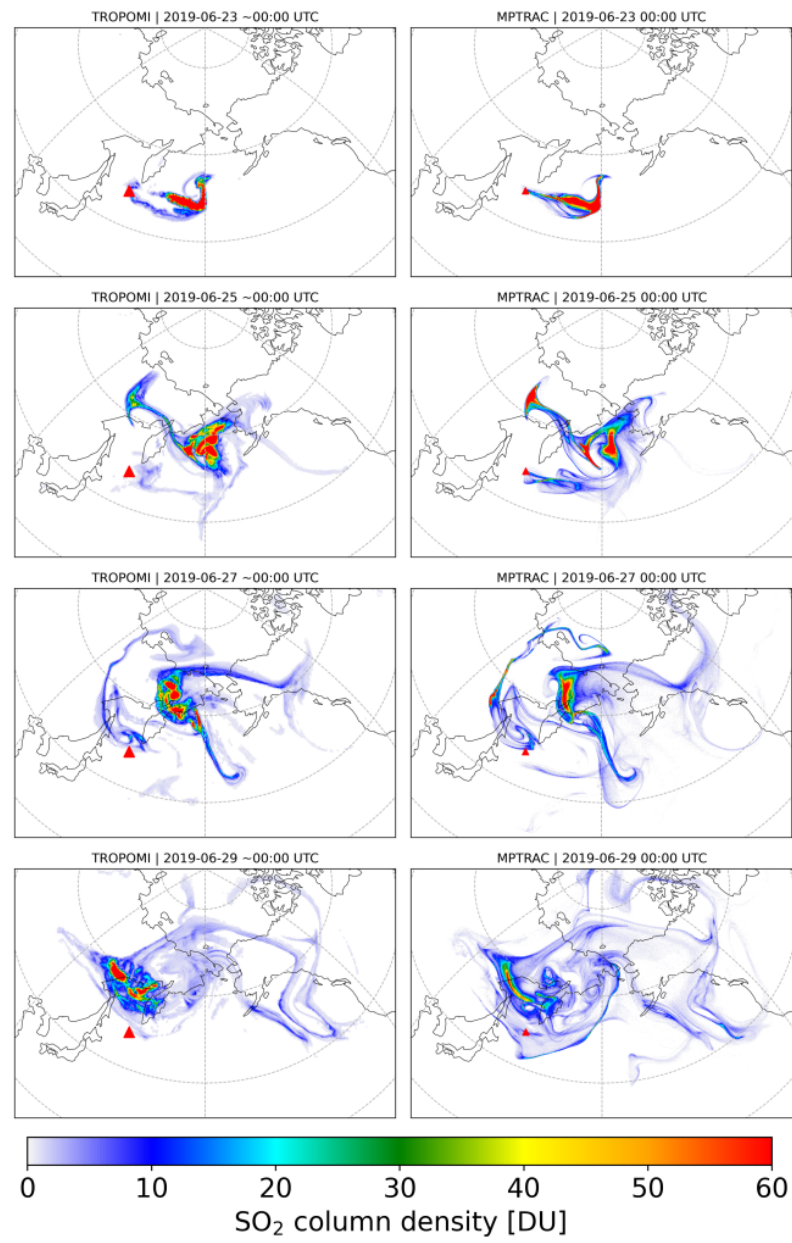


Figure 5.2: Evolution of SO₂ total column density distributions from 23 June 2019 to 30 June 2019 from the MPTRAC simulation with implicit chemistry scheme (right column) and TROPOMI satellite observations (left column). The red triangle marks the location of the Raikoke volcano.

5.2. Results

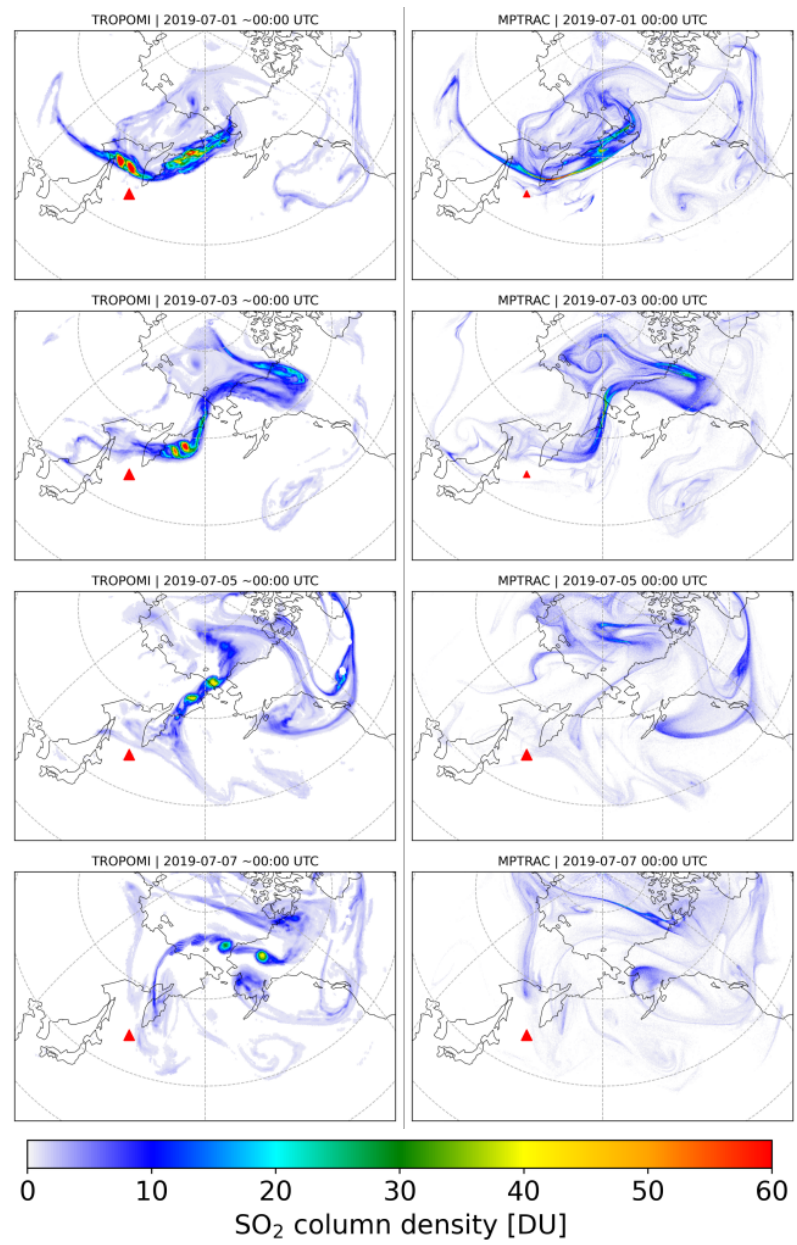


Figure 5.3: Same as Fig. 5.2, but from 1 July 2019 to 7 July 2019.

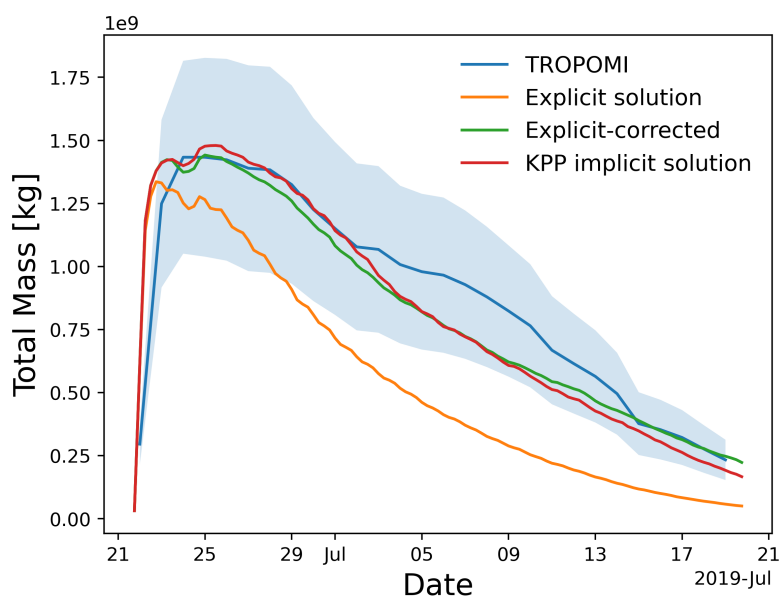


Figure 5.4: Temporal evolution of the SO_2 total mass burden of the 2019 Raikoke eruption from TROPOMI measurements (blue curve, shading shows uncertainty range) and MPTRAC simulations with explicit solution (orange curve), simplified explicit solution with correction (green curve), and KPP implicit solution (red curve).

to a reduction of the OH concentration within the SO_2 plume, which is captured by the implicit chemistry scheme but not by the explicit scheme, which uses a constant OH climatology.

5.2.2 Correction for the simplified explicit scheme

From Figs. 5.4 and 5.5, it can be seen that the simplified explicit approximation overestimates the SO_2 decay rate by $\sim 60\%$ compared to the TROPOMI observations, whereas the implicit KPP solution agrees well with the TROPOMI observations. Hence, there is also a $\sim 60\%$ difference between the explicit and KPP solution. This overestimation in the explicit scheme is likely due to changes in OH and other radicals resulting from the SO_2 injection itself, which are not accounted for in the climatology. To account for that, we perform a SO_2 dependent correction to the OH climatology. Essentially, the simplification of the explicit scheme applies a linear approximation to describe the non-linear oxidation processes. To compare the differences in lifetime of the two schemes, we performed another simulation without SO_2 injections to estimate the undisturbed background levels of OH and H_2O_2 and compare them with the situation in the SO_2 plumes. Figure 5.6 shows the ratio of the OH and H_2O_2 concentrations in the SO_2 plume versus the background oxidant concentrations as a function of SO_2 VMR. The ratio decreases as the abundance of SO_2 increases, which means that the depletion of the oxidants is faster than their production. In highly-

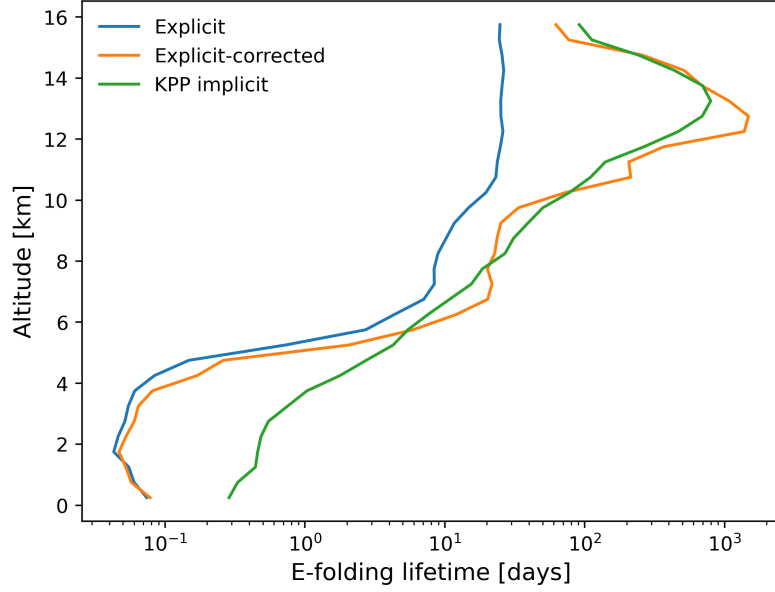


Figure 5.5: Vertical profiles of the average SO_2 e-folding lifetime of MPTRAC simulations with explicit solution (green curve), explicit solution with correction (orange curve) and KPP implicit solution (blue curve) during 25 June to 4 July.

concentrated SO_2 regions the oxidants are almost completely depleted.

Note that the data points shown in Fig. 5.6 are filtered using a Z-score threshold, because there are factors other than the chemical reactions that will affect the SO_2 distributions such as diffusion, convection, wet deposition, etc., causing the data not to be statistically reliable. After filtering outliers with low Z-scores, a correction formula to estimate OH concentrations in the plume from OH background levels and the SO_2 concentration can be obtained by regression,

$$[\text{OH}] = 4.72 \times 10^{-8} [\text{SO}_2]^{-0.83} \times [\text{OH}]_{\text{background}}. \quad (5.1)$$

Similarly, the correction formula for H_2O_2 is

$$[\text{H}_2\text{O}_2] = 3.13 \times 10^{-6} [\text{SO}_2]^{-0.57} \times [\text{H}_2\text{O}_2]_{\text{background}}. \quad (5.2)$$

By applying the corrections to the climatological OH and H_2O_2 data to account for their removal in the SO_2 plume, a simulation with the simplified explicit approximation with correction can be conducted. Figure 5.5 shows that above 10 km of altitude, the correction for the simplified explicit solution shifts the simulated lifetime closer to the KPP implicit solution. The correction reduces the amount of the oxidants when SO_2 is highly abundant in the volcanic plume. The mass evolution simulated by the corrected explicit solution is therefore in better agreement with

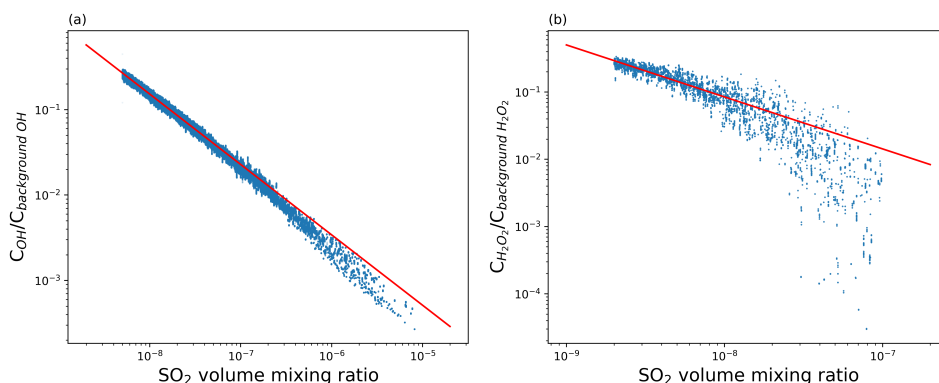


Figure 5.6: Ratio of OH concentration in dry atmosphere (a) and H_2O_2 concentration in cloud regions (b) in the Raikoke SO_2 plume versus background levels as a function of the SO_2 VMR. Each data point represents a single air parcel. The red curves represent the regression formulas given in Eqs. (5.1) and (5.2).

the TROPOMI measurements and the KPP implicit solution (Fig. 5.4). These results reflect the fact that the chemical degradation of volcanic SO_2 is a non-linear process, which means that it should not simply be treated as pseudo-first-order reaction. The correction of the OH and H_2O_2 concentrations applied to the explicit solution improves the representation of SO_2 decay in the transport simulations, with almost no additional computational overhead.

5.2.3 Evaluation of the simulated OH field

The hydroxyl radical (OH) is an important oxidant in atmospheric chemistry, controlling the chemical decomposition of various species. For chemistry-transport simulations of volcanic SO_2 in the UT/LS region, oxidation via OH is the main factor of mass decay in the gas phase. In order to simulate the OH background conditions during the Raikoke case study without any enhanced levels of volcanic SO_2 abundance with the chemical mechanism introduced in Sect. 2.3, we distributed a total of 1 million air parcels between 9 to 17 km altitude. The fourth generation Copernicus Atmosphere Monitoring Service (CAMS) global reanalysis data (Inness et al., 2019) were then used to compare with the OH field obtained with the implicit chemistry scheme implemented in MPTRAC. The CAMS reanalysis combines model data with observations using data assimilation techniques, providing a global distribution of atmospheric species.

Figure 5.7 shows a comparison of OH zonal mean distributions at different pressure levels from CAMS, MPTRAC, and the CLaMS zonal mean climatology Pommrich et al. (2014). Both the CAMS reanalysis data and the CLaMS climatological data have been evaluated by comparison with in-situ measurements in Liu et al. (2023). Furthermore, Fig. 5.8 shows the global CAMS and

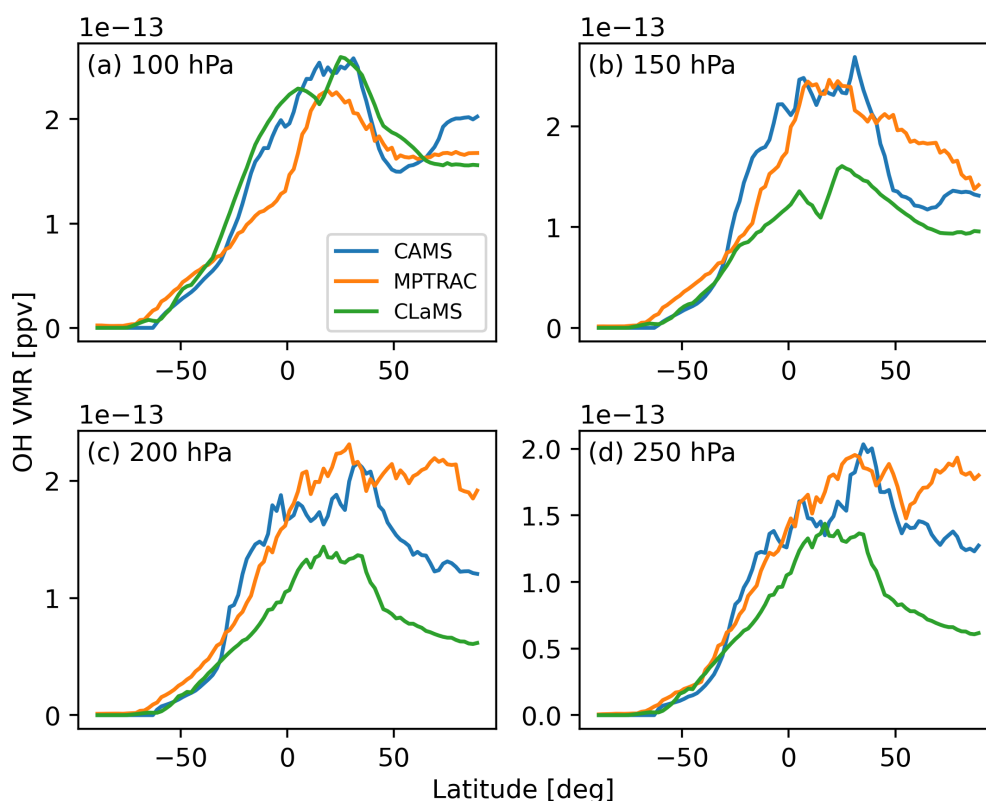


Figure 5.7: Zonal mean distributions of the OH field obtained from the CAMS reanalysis (blue curve), climatological data from the CLaMS model (green curve) and the MPTRAC simulation (orange curve) at pressure levels of 100 hPa (a), 150 hPa (b), 200 hPa (c) and 250 hPa (d) on 1 July 2019, 00:00 UTC.

MPTRAC OH fields at pressure levels of ~ 100 hPa, ~ 150 hPa, ~ 200 hPa and ~ 250 hPa on 1 July 2019, 00:00 UTC. The OH fields obtained by MPTRAC show some similar distributions with respect to the solar zenith angle dependence as CAMS, which is due to the strong correlation between OH production and solar radiation. The OH fields simulated by the different models are at the same magnitude. The MPTRAC chemistry modeling can simulate the production and loss of the short-lived OH radical in the UT/LS region at reasonable accuracy, which is essential for modeling of the SO_2 lifetime .

5.2.4 Selection of the chemistry time step

In MPTRAC, a fixed time step is applied for numerical integration of the trajectories and in most other modules. Based on previous studies (Röbner et al., 2018; Clemens et al., 2024), a time step of 180 s was selected for calculating trajectories with the midpoint method and considering the spatio-temporal resolution of the ERA5 reanalysis data. This choice of the time step provides a

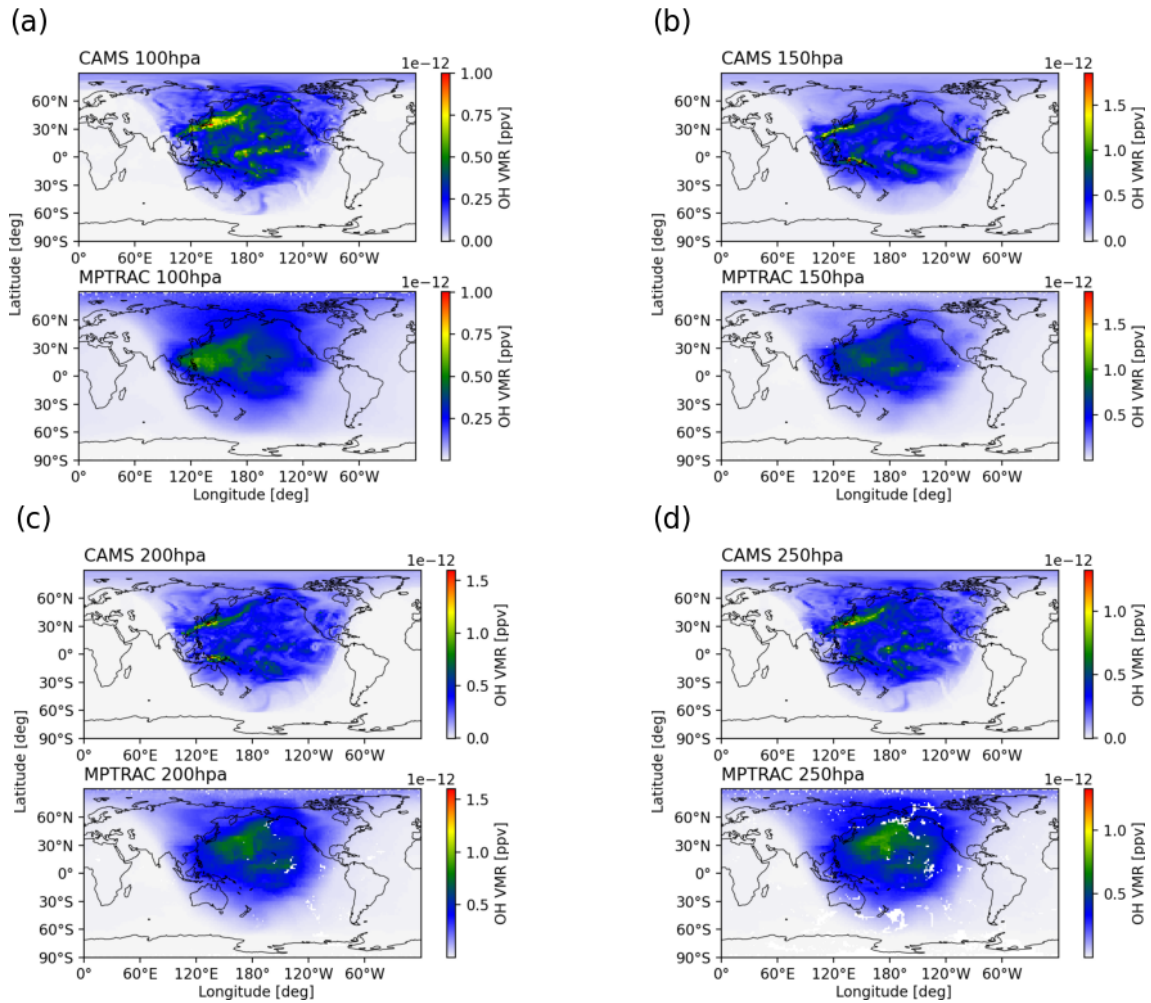


Figure 5.8: Global OH fields obtained from the CAMS reanalysis (top) and MPTRAC simulations (bottom) at pressure levels of 100 hPa (a), 150 hPa (b), 200 hPa (c) and 250 hPa (d) on 1 July 2019, 00:00 UTC.

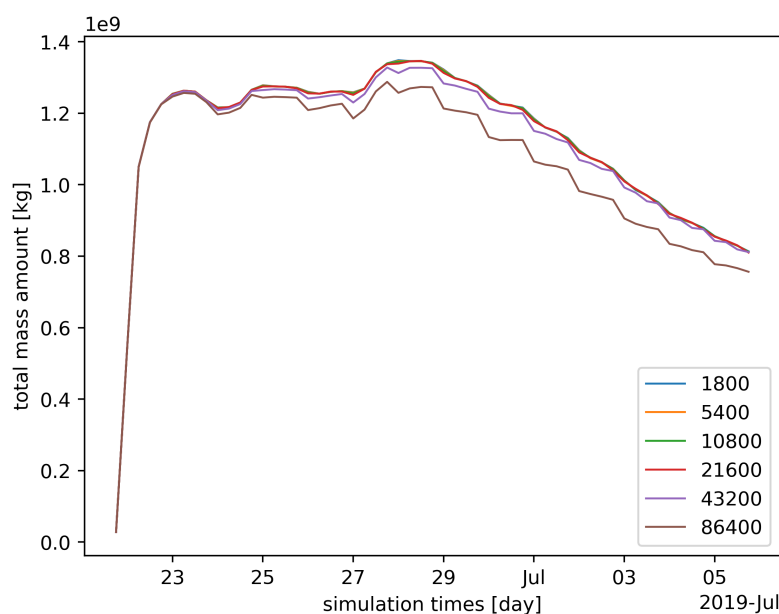


Figure 5.9: Total mass burden evolution simulated with different chemistry time step size settings of 3600, 7200, 10800, 21600, 43200 and 86400 seconds.

reasonable trade-off in terms of accuracy and computational costs of the trajectory calculations, i. e., it is small enough to consider integration errors negligible while providing a minimum in computation time. In terms of computation effort, the time step of 180 s is acceptable for the explicit solution, but not efficient for the implicit chemistry calculations, which is particularly demanding in terms of computation.

To improve the computational efficiency, we implemented a distinct time step for the chemistry calculations. The chemistry time step is an important control parameter, as it has a significant impact on the computational efficiency. The chemistry time step size should be as large as possible without compromising the accuracy of the results. Figure 5.9 shows the SO_2 total mass time evolution obtained by different chemistry time steps. The results diverge when the time step of the chemistry solution is larger than 6 h. Therefore, we recommend using a chemistry time step of 3 to 6 h to balance the computational efficiency and accuracy of the solution for the volcanic SO_2 oxidation.

5.2.5 Assessment of computational costs

The KPP-based implicit chemistry solver implemented in MPTRAC can solve complex chemical mechanisms with flexible definition of the chemical reactions and species. In the case of the volcanic SO_2 chemistry-transport simulations, the corrected explicit solution achieves similar re-

sults with higher computational efficiency. For now, GPU offloading has been implemented using OpenACC for the simplified explicit scheme, while for the implicit scheme this is planned for the future. Figure 5.10 shows the runtime of MPTRAC simulations on the JUWELS supercomputer at the Jülich Supercomputing Centre comparing the implicit and explicit chemistry schemes using a chemistry time step of 21600 s and 180 s, respectively. The CPU simulations were conducted on a single compute node of the JUWELS Cluster (Jülich Supercomputing Centre, 2019), parallelized with 48 OpenMP threads. Each compute node of JUWELS Cluster contains 2 Intel Xeon Platinum 8168 CPUs with 24 physical cores per CPU. The GPU simulations were conducted on JUWELS Booster (Jülich Supercomputing Centre, 2021) with 2 AMD EPYC Rome 7402 CPUs and 4 NVIDIA A100 GPUs.

Regarding the chemistry, Figure 5.10a shows that the simplified explicit solution is about 5.3 times faster than the KPP implicit solution for a simulation with 1 million air parcels. Considering that file-I/O and meteorological data preprocessing also require a substantial part of the total runtime, the total runtime is reduced by $\sim 56\%$ by choosing the more efficient explicit chemistry scheme. The GPU solution of the simplified explicit chemistry scheme on JUWELS Booster reduces the total runtime by $\sim 75\%$, with the runtime required for chemistry becoming nearly negligible. As the scale of the simulation increases (i. e., for simulations with more air parcels), the advantage of the explicit solution in terms of computational efficiency becomes even more pronounced. Figure 5.10b shows that the total runtime is reduced by 92% for a simulation with 3 million air parcels. This improvement in computational efficiency is particularly relevant for large-scale chemistry transport simulations, where finding the proper trade-off between accuracy and computational costs is most critical. In the future, the KPP implicit scheme might also be equipped with GPU offloading to improve its performance (Alvanos and Christoudias, 2017; Christoudias et al., 2021).

5.3 Discussion

The Lagrangian transport model MPTRAC provides two alternative schemes to simulate SO_2 chemistry for volcanic eruptions. The explicit scheme uses monthly mean zonal climatology data of radical species to determine reaction rates and calculate mass loss as an exponential decay of SO_2 . The implicit scheme uses the Rosenbrock integrator provided by the KPP software package to calculate the multi-species chemical reaction processes. KPP can solve complex chemical mechanisms with flexible definition of chemical species, reactions, and rate coefficients. The

5.3. Discussion

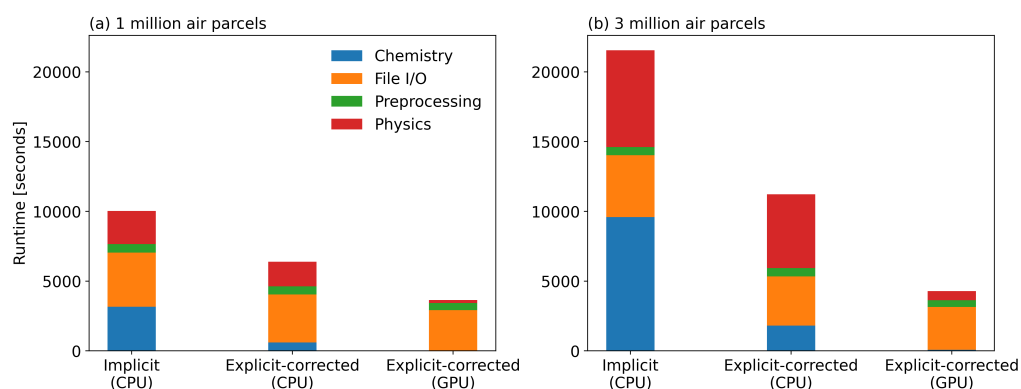


Figure 5.10: Computational costs of the Raikoke simulations with different chemistry schemes (the implicit scheme and the simplified explicit scheme with correction) on the JUWELS Cluster (CPU) and JUWELS Booster (GPU) for a simulation with 1 million air parcels on a scale of 1 million air parcels (a) and 3 million air parcels (b). The blue bar represents the runtime for the chemistry calculations, while the red bar represents the runtime for the other physical modules besides chemistry.

implicit solution allows for more complex, non-linear chemical mechanisms with dynamic reaction rates depending on the species concentrations. Here, we propose a chemical mechanism with 31 reactions and 12 species to model the production and loss of the short-lived OH radical and H_2O_2 , which are essential for the decomposition of SO_2 in the gas and aqueous phase, respectively, in the UT/LS region. The mechanism proposed here can serve as a basis for developing more complex chemical mechanisms in future studies. It could also be further optimized by evaluating the relevance of each reaction pathway to reduce the computational effort.

The OH radical is the main oxidant in the gas phase, which largely controls the decomposition of SO_2 in the UT/LS. We compared the OH radical field obtained by the proposed mechanism in MPTRAC with CAMS reanalysis data and climatological data from the CLaMS model. The OH radical field obtained by the proposed mechanism shows a clear characteristic of diurnal variation and concentrations at a similar level compared to these reference datasets. The cloud phase H_2O_2 oxidation also has a significant impact on the SO_2 decay in the lower troposphere. It must be taken into account to properly represent the loss of tropospheric SO_2 over time, especially for other volcanic eruptions, such as those happening in the tropics with lower peak emission heights (Liu et al., 2023).

By applying the proposed chemical mechanisms in the implicit and explicit chemical solution to the case study of the June 2019 Raikoke eruption, the mass burden evolution and the vertical distribution of the lifetime are discussed. The implicit solution with the numerical integrator generated by KPP shows good agreement with the TROPOMI high-resolution satellite measurements with respect to the SO_2 total mass burden evolution. However, the explicit solution using a first-order

simplification shows an overestimation of the SO₂ decay rate by 60% compared to the implicit solution. This overestimation is due to using OH and H₂O₂ climatological background fields without considering enhanced levels of SO₂. By comparing the OH and H₂O₂ concentrations in the SO₂ plume with the background values, we obtained the correction formula $y = ax^b$ by regression for OH and H₂O₂. The correction formula is used to adjust the oxidant concentrations interpolated from the prescribed climatology data. This correction formula imposes a non-linear behavior on the chemical degradation of SO₂ and significantly improves the SO₂ lifetime representation in the UT/LS in the simulations with the explicit chemistry scheme. We tested the correction also for another volcanic eruption case, i. e., the July 2018 Ambae eruption (Liu et al., 2023), where it yields a comparable total lifetime of SO₂ to that predicted by the KPP implicit solution.

The proposed simplified explicit solution with correction provides realistic chemical lifetime modeling compared to the implicit solution and achieves more than 5 times higher computational efficiency in our example. For the trade-off between computational efficiency and simulation accuracy, the simplified explicit solution with correction is believed to have the capability to be applied in the future large-scale application requiring high computational effort, such as inverse modeling for emission reconstruction. The backward trajectory approach used in our previous studies of volcanic SO₂ plume did not consider realistic chemical lifetime modeling. We are currently developing inverse modeling for source estimation, including support for nonlinear chemical mechanisms. The implications between lifetime modeling and source reconstruction are also being investigated and discussed in the next chapter.

Chapter 6

Inverse source estimation of volcanic sulfur dioxide with a particle filter

In this chapter, we develop a particle filter based inverse source estimation approach, which allows consideration of the SO₂ sink modeling in MPTRAC, especially the non-linear chemical change that depends on the SO₂ concentration itself introduced in Chapter 5. In the previous chapter, we found that using the implicit chemistry scheme with complex chemical mechanisms can lead to more accurate predictions of volcanic SO₂ lifetimes. The SO₂ lifetimes exhibit significant variability with altitude, typically ranging from a few hours to several days below 5 km, while extending to 10 to 100 days above this altitude. This mainly results from the wet deposition and aqueous phase H₂O₂ reaction in the presence of clouds. It is conceivable that the emission reconstruction plays a crucial role in influencing the total residence time of volcanic SO₂.

In previous works of our group, the backward trajectory approach has been used to estimate volcanic SO₂ emissions in several case studies using the MPTRAC model. Notable examples among others include the Nabro eruption (Hoffmann et al., 2016), the Sarychev eruption (Wu et al., 2017), and the Raikoke eruption (Cai et al., 2022). The main idea of these studies was to release air parcels in vertical columns over the satellite footprints with SO₂ detections. Trajectories were then computed in backward direction and traced back to the location of the volcano or not. The backward trajectory method can often well capture the shape of a volcanic plume, but the approach cannot accurately capture the non-linear mass evolution processes of SO₂ and may misidentify the main release peak. Specifically, this approach may lead to overestimation of SO₂ concentrations at higher altitudes, where SO₂ has a longer lifetime, and underestimation at lower altitudes, where the SO₂ lifetime is shorter. Processes such as oxidation, wet deposition, and mixing of air introduce non-linearities that influence the abundance of SO₂ over time. Consequently,

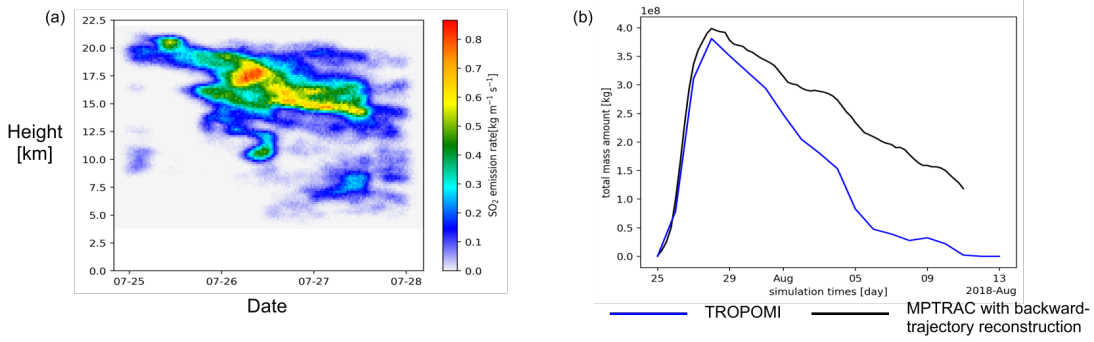


Figure 6.1: (a) The SO₂ emissions reconstructed using the backward trajectory method. (b) The resulting SO₂ mass evolution simulated with the initialization of SO₂ emissions as shown in (a).

ignoring these processes can distort the estimated emission profiles.

We choose the Ambae eruption in July 2018 and the Raikoke eruption in June 2019 as case studies. Figure 6.1a shows the time- and altitude-resolved emissions reconstructed using the backward trajectory method. The primary release peak is concentrated between altitudes of 15 to 20 km. Due to the longer residence time of SO₂ at higher altitudes, the backward trajectory method tends to overestimate the reconstructed emissions within this altitude range. This overestimation occurs because the method does not fully account for the slower chemical decay of SO₂ at higher altitudes, leading to an inflated estimate of the emissions that contributed to the observed SO₂ concentrations. Using the reconstructed emissions as initialization for the model, the resulting mass evolution is shown in Fig. 6.1b, which shows an overestimation of the total residence time of SO₂ compared to TROPOMI observations.

6.1 Particle filter algorithm

The background introduction and reviews of inverse modeling and particle filter has been given in Sect. 1.3. A flowchart of the inverse modeling and simulation system using a particle filter as proposed in this study is shown in Fig. 6.2. We use a parameter vector $x_k = \{h_k, t_k, m_k\}$, $k = 1, \dots, N$, with $h_i \in [h_l, h_u]$, $t_i \in [t_l, t_u]$, $m_i \in [m_l, m_u]$, to represent the possible source state of the simulated SO₂ plume, with minimum and maximum bounds for each parameter. Here, h denotes the release height, t denotes the release time, and m corresponds to the total release mass. For each sample, the unit simulation k is initialized by generating air parcels distributed according to a Gaussian distribution $M(x_k)$ centered on the release height h_k and release time t_k with a total mass m_k . After completing each forward simulation with the sample release parameters, including trajectory calculations and chemical/physical processes, the likelihood function $p(\mathbf{y}|\mathbf{x}_i)$

6.1. Particle filter algorithm

is calculated with the simulated SO₂ column densities (denoted as $H(\mathbf{x})$) and corresponding observations (denoted as \mathbf{y}), formulated with Gaussian assumption (van Leeuwen, 2009),

$$p(\mathbf{y}|\mathbf{x}_i) = \exp\left\{-\frac{1}{2}[\mathbf{y} - H(\mathbf{x}_i)]^T \mathbf{R}^{-1}[\mathbf{y} - H(\mathbf{x}_i)]\right\}. \quad (6.1)$$

The importance weight w_i is given by normalizing the likelihood,

$$w_i = \frac{p(\mathbf{y}|\mathbf{x}_i)}{\sum_{j=1}^N p(\mathbf{y}|\mathbf{x}^{(j)})}. \quad (6.2)$$

Here, $H(\mathbf{x})$ and \mathbf{y} are represented in terms of $1^\circ \times 1^\circ$ grid box column density values. The matrix \mathbf{R} denotes the error covariance of the observations and model results. A larger error implies a looser fit between the observations and the model results, while a smaller error forces the particles to match the observations more closely. Larger errors lead to more similar weights across particles, making the weight distribution flatter and reducing the ability to distinguish between particles. In contrast, smaller errors concentrate the weights on a few particles, which can lead to filter degeneracy, which may cause a loss of particle diversity and result in biased estimates. To quantify the overall standard deviation that combines the errors in the model and observations, we calculate the observation variance within each grid and scale it by a specific factor to represent the total errors. This factor has different optimal values in different cases and needs to be tuned to obtain a good performance of the filter. In the Ambae case, it is set to 1×10^3 while in the Raikoke case, the observed plume spreading time is longer and therefore the factor is set much larger to 1×10^6 .

To avoid the situation where a small number of samples occupy most of the weights, leading to a too small effective sample size and too little statistical information in the ensemble, which is known as filter degeneracy, resampling needs to be introduced. The idea of resampling is to replace some low-weight particles (samples) with high-weight perturbed particles to approximate the posterior probabilistic density function (PDF). In this case we utilize a residual resampling method, proposed by Liu and Chen (1998).

The particle filter algorithm works as follows:

1. Sample parameter vector $\mathbf{x}_k^{(j)} = \{h_k, t_k, m_k\}$, $k = 1, \dots, N$, where $h_i \in [h_l, h_u]$, $t_i \in [t_l, t_u]$, $m_i \in [m_l, m_u]$, from a uniform distribution, where j denotes the sampling step and k denotes the sample (particle) index.
2. Run the unit simulations forward in time with the sample parameters to output the SO₂

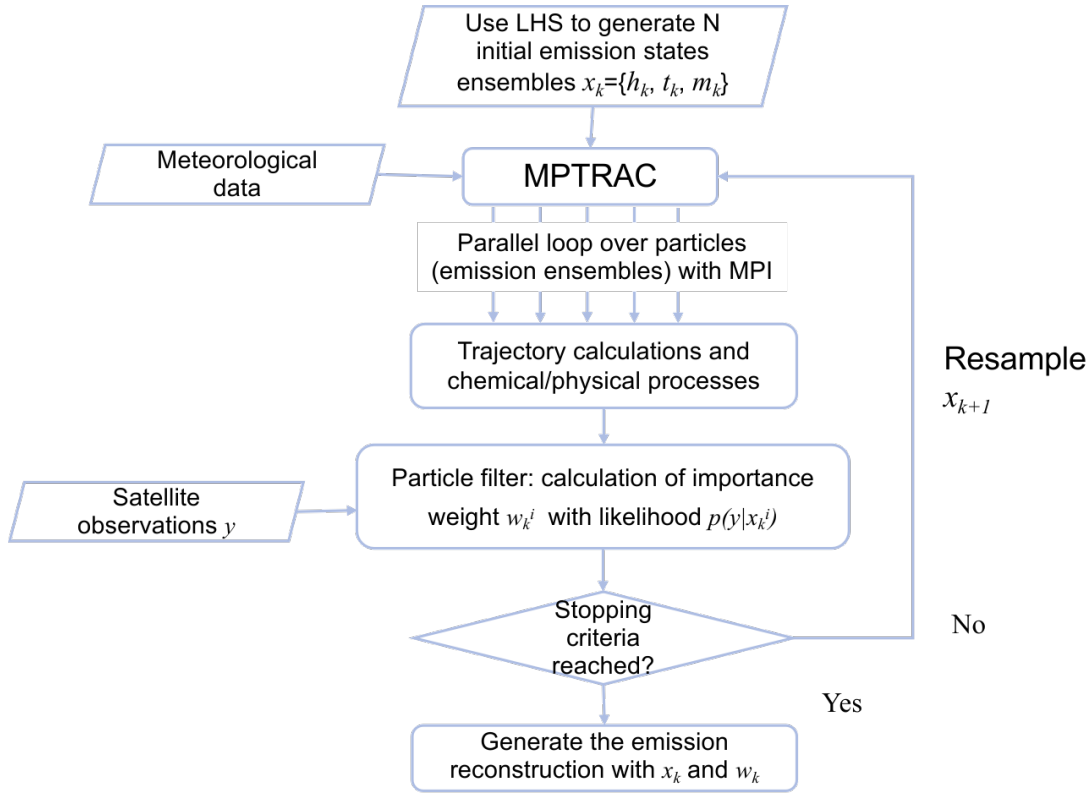


Figure 6.2: Flow chart of the proposed inverse modeling and simulation system to reconstruct the SO_2 release parameters and emission rates.

column density and calculate the likelihood function with Eq. (6.1). Here $H(x)$ represents the Lagrangian transport simulation and y denotes the satellite observations. Calculate the importance weights according to Eq. (6.2).

3. Resampling: Use the residual resampling method to replace low-weight particles with perturbed high-weight particles. Increase j by 1 and repeat steps 2 and 3 until converged. The effective sample sizes (ESS) serve as the convergence condition,

$$ESS = \frac{1}{\sum_{i=1}^N w_i^2}. \quad (6.3)$$

The iteration ends when ESS is larger than a given threshold or stabilized.

After the resampling step reaches convergence, each ensemble emission is weighted by the normalized likelihood with their importance weight w_i . Thus the final reconstruction of emissions is computed by combining all the particles according to their weight,

$$M = \sum_{i=1}^N w_i M(x_i). \quad (6.4)$$

6.2 Ambae case study

6.2.1 Simulation setup

We used the particle filter algorithm described above to conduct the inverse estimation of SO₂ emissions and the final forward simulations based on the estimated emission data for the Ambae case. For the forward simulations, the corrected explicit chemistry scheme and wet deposition scheme, introduced in Sect. 5.2.2 and 2.2.1, is utilized to model the sinks of the volcanic SO₂ plume. To generate the ensemble efficiently and ensure comprehensive coverage of the parametric space with orthogonality, we use Latin Hypercube Sampling (LHS) (Iman and Conover, 1980) to generate $N = 300$ parameter vectors $\mathbf{x}_k = \{h_k, t_k, m_k\}$ from a uniform distribution. The release height (h_k) range is 4~20 km, the release time (t_k) duration is from 25 July 2018, 00:00 UTC to 28 July 2018, 00:00 UTC, and the total mass (m_k) range is 0.2~0.6 Tg. As for meteorological input data, we utilized the ERA-5 reanalysis is used.

6.2.2 Particle filter versus backward trajectory method

Figure 6.3 shows the importance weight distributions of each step during the importance resampling iterations. During this process, the particles with low importance weights are replaced by perturbed particles with higher importance weights. As the iteration progresses, the particle distribution becomes increasingly concentrated into two distinct clusters, one at an altitude of 15 to 20 km and the other at 5 to 8 km. This is further illustrated in Fig. 6.4, which shows the vertical profiles of emission rates at each sample step of the particle filter. The peak emissions occur in the lower altitude range (~5 to 8 km), as the simulation indicates that particles released at higher altitudes would remain in the atmosphere for a longer duration than observed, leading to a lower likelihood and importance weight.

In case of the Ambae eruption in July 2018, there are two possible release peaks in the vertical direction. The weight distribution of these two release peaks will determine the total residence time of SO₂. Greater weight in the higher release peak corresponds to a longer total residence time in the atmosphere. Compared to the reconstruction of emissions by the backward trajectory approach (Fig. 6.1a), the reconstruction by the particle filter approach assigns a higher fraction of emissions to the release peak around 5~8 km altitude (Fig. 6.5).

The particle filter approach approximates the posterior PDF using Eq. (6.1), which accounts for the differences between SO₂ column density as simulated and observed, whereas the backward trajectory method is primarily concerned with ensuring that the model predicts the shape of

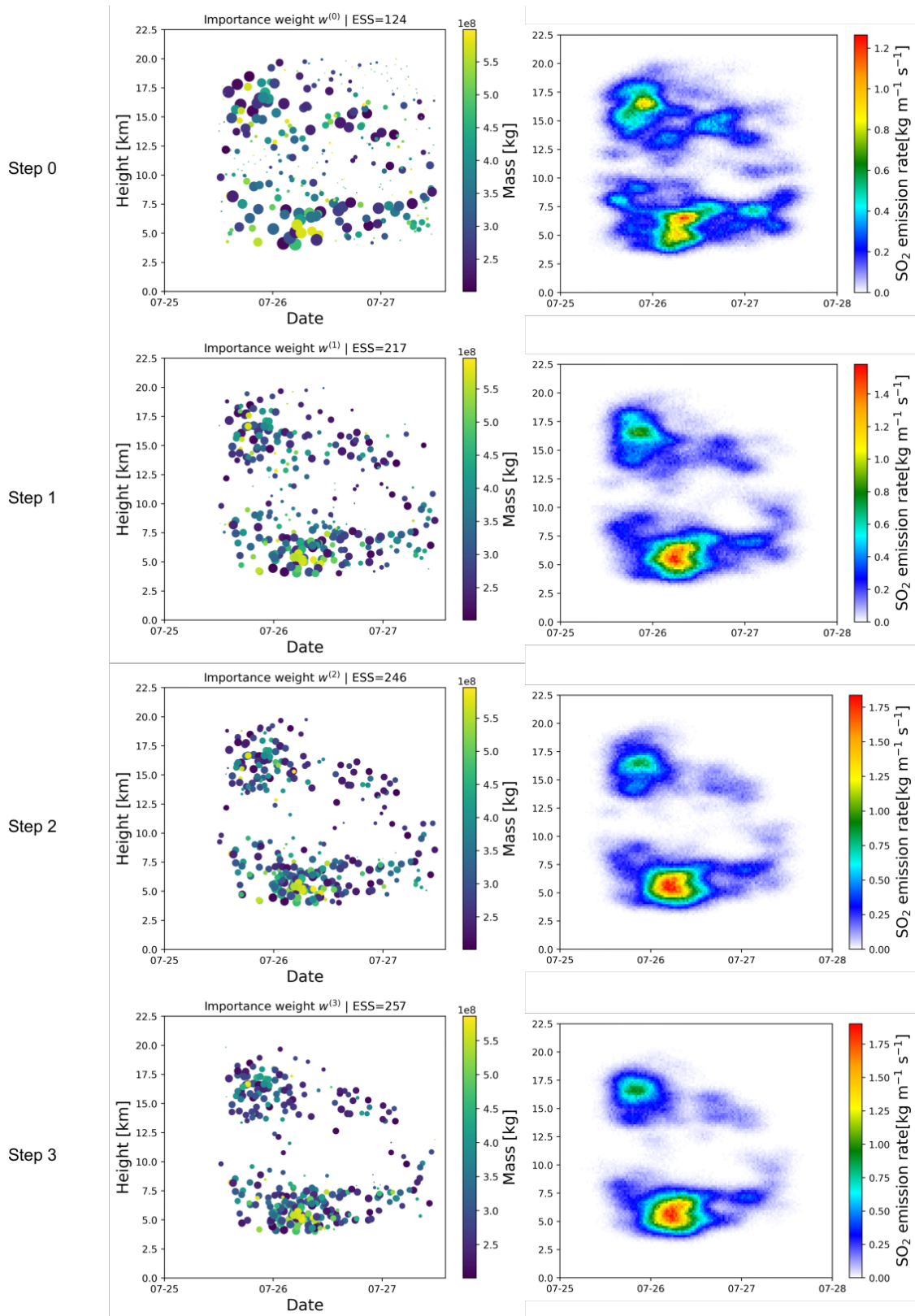


Figure 6.3: The importance weight distribution (left column) and the respective reconstruction of emissions (right column) for the Ambae eruption in July 2018. The point size represents the importance weight of the sample.

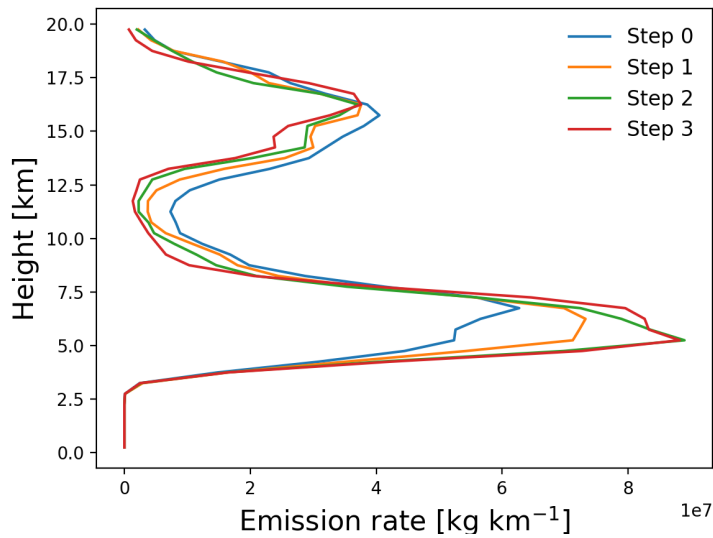


Figure 6.4: Vertical profiles of emission rates at different steps of the inverse modeling process for the Ambae eruption in July 2018.

the volcanic SO_2 plume. This different treatment of the target leads to the discrepancies in the estimated height distributions of the emissions, and also leads to different total residence times of SO_2 . As shown in Fig. 6.6, regarding the total mass evolution, the simulation initialized with the particle filter approach aligns more closely with the TROPOMI data after August 31, compared with the backward trajectory approach, which indicates that it is reasonable to attribute more release to the lower release peak. The backward trajectory approach locates emissions at mid-level altitudes and tends to overestimate the total mass after the peak.

Figure 6.7 compares the plume extent from TROPOMI observations and MPTRAC simulations using source emissions derived from the particle filter (PF) and backward trajectory (BT) method. Although the main release peak of emissions in the two source estimation schemes is located at different heights, the overall plume extent over time does not show a significant divergence. By comparing the figure panels which correspond to different time steps (July 27 to August 7, 2018), the TROPOMI data shows that the plume spreads eastward from the Ambae eruption site. Both methods simulate an eastward dispersal of the SO_2 plume, closely following the observations captured by TROPOMI. The MPTRAC-PF approach, which uses the particle filter for source estimation, appears to provide a closer match to the observed plume structure in both extent and SO_2 density over the same period. The MPTRAC-PF approach tends to show a more diffuse and gradually spreading plume, while the MPTRAC-BW approach results in a more concentrated plume in the initial stages. The results demonstrate the alignment between the observed plume

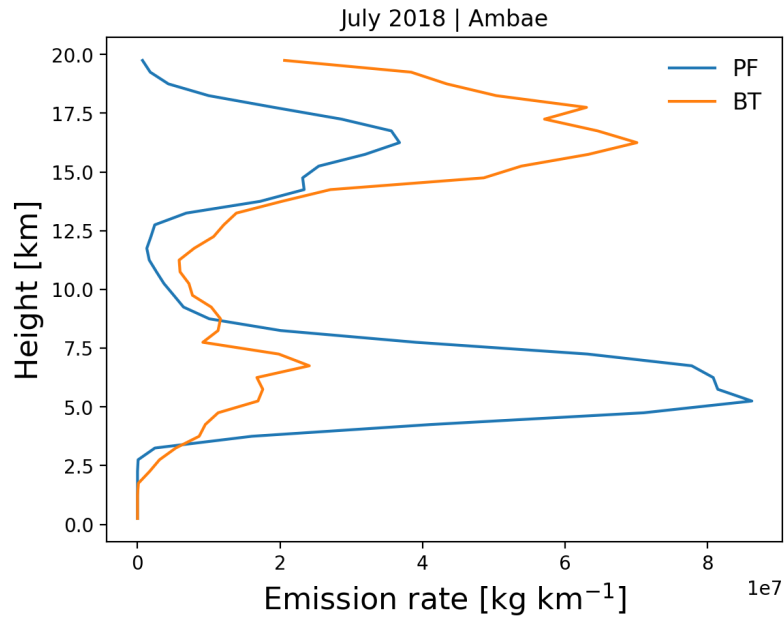


Figure 6.5: Vertical profiles of emission rates for the Ambae eruption in July 2018, estimated with the particle filter (PF) approach (blue curve) and backward trajectory (BT) approach (orange curve).

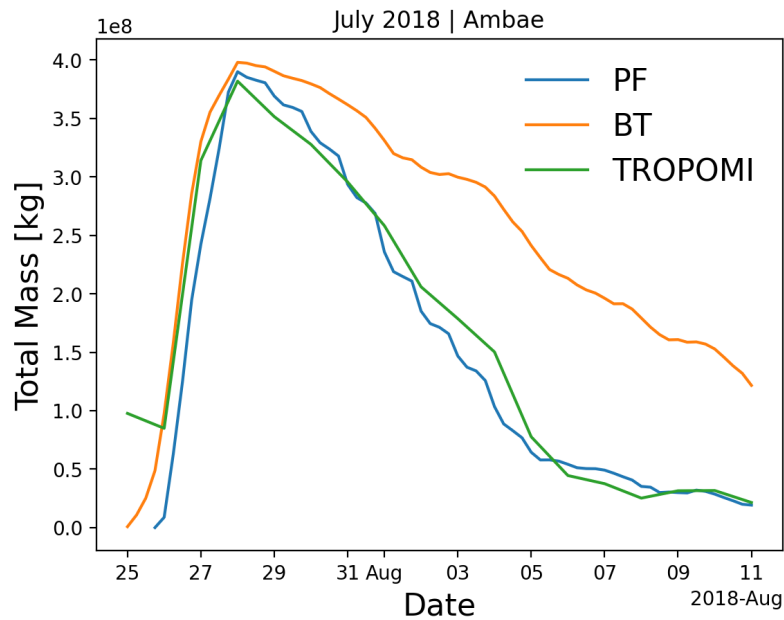


Figure 6.6: Temporal evolution of the SO_2 total mass for the Ambae eruption in July 2018 from TROPOMI measurements (green curve) and MPTRAC simulations with initial release of emissions estimated with the particle filter approach (blue curve) and the backward trajectory approach (orange curve).

behavior and the model outputs, highlighting the performance of the particle filter approach in estimating source emissions.

6.2.3 Sensitivity of reconstructed emissions to sink modeling

The inverse reconstruction of emissions with the particle filter enhances the source estimation by allowing the integration of complex, non-linear sink modeling. This capability is crucial for accurate reconstruction of emission profiles, as it enables the model to account for variable and dynamic atmospheric processes that affect the removal and transformation of emissions across different altitudes and regions. In this section, we perform a control experiment to compare the effects of different sink modeling methods on the reconstructed emissions. Specifically, the results of using a constant decay rate with an e-folding lifetime of 4 days are contrasted with a more complex approach that includes chemical reactions and wet deposition which gives rise to the vertical lifetime variability, as introduced in the previous chapter.

The reconstructed emission profiles are shown in Fig. 6.8. It is found that when using the constant lifetime without vertical variability, the two release peaks (altitudes of 13~18 km and 3~8 km) have almost equal weight. A constant lifetime model does not differentiate between the removal efficiencies at different altitudes, treating emissions at different levels similarly. In the approach that incorporates complex chemical reactions and wet removal processes, the shorter lifetime of emissions at lower altitudes leads to a higher weighting of these emissions, which is more consistent with the relatively short residence time presented by the TROPOMI observations.

6.3 Raikoke case study

6.3.1 Simulation setup

In this section, the particle filter is used for source estimation of the Raikoke eruption in June 2019. 300 parameter vectors $\mathbf{x}_k = \{h_k, t_k, m_k\}$ sampled from a uniform distribution are generated with LHS. The release height (h_k) range is 6~18 km, the release time (t_k) duration is from 21 June 2019, 12:00 UTC to 25 July 2019, 12:00 UTC, and the total mass (m_k) range is 0.5~2 Tg. As for meteorological input data, we utilized the ERA-Interim reanalysis due to its lower memory requirements and better computational efficiency.

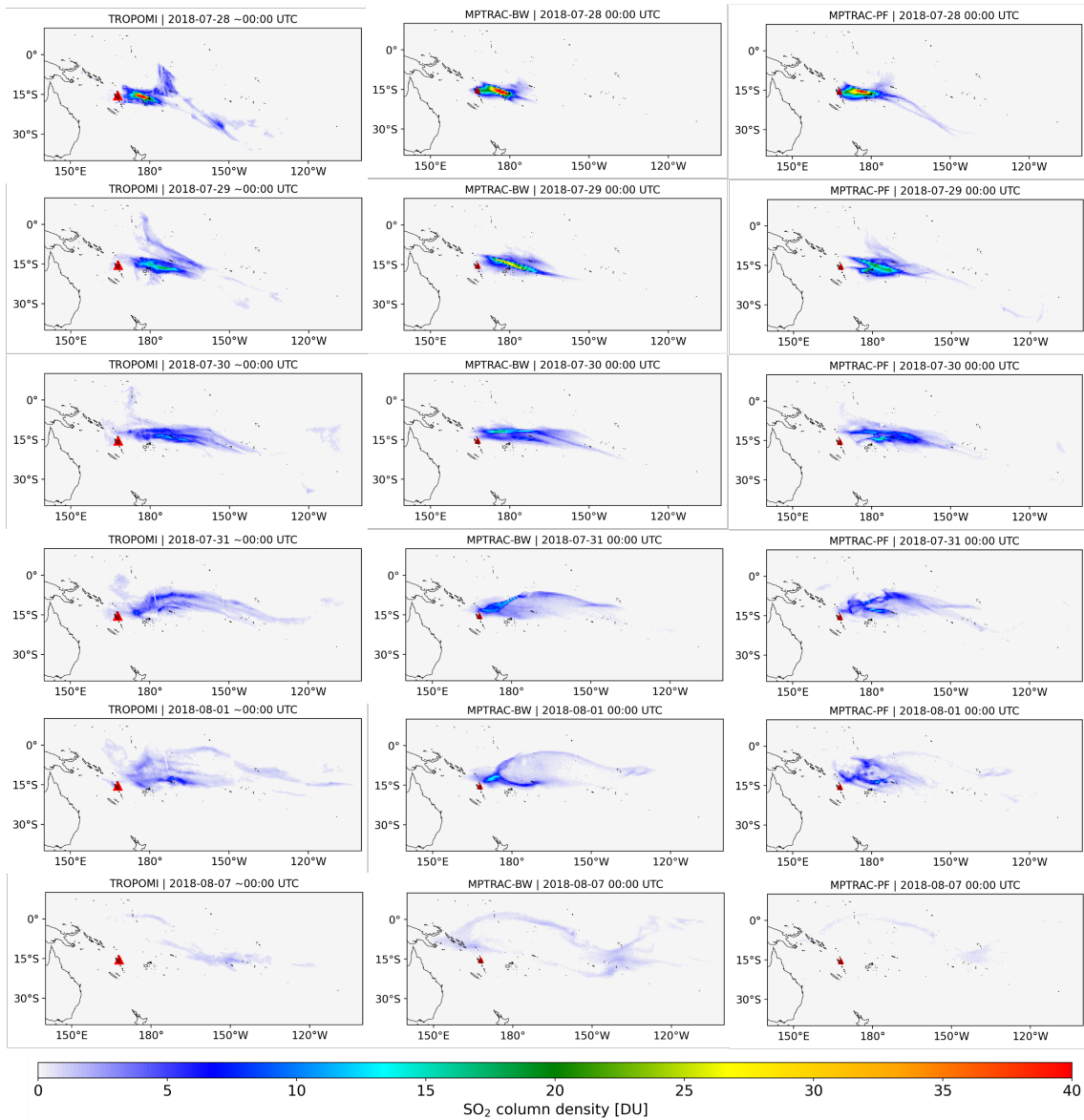


Figure 6.7: SO₂ column density from TROPOMI observations (left column) and MPTRAC simulations using source emissions derived from the backward trajectory (BT, middle column) method and particle filter (PF, right column), respectively.

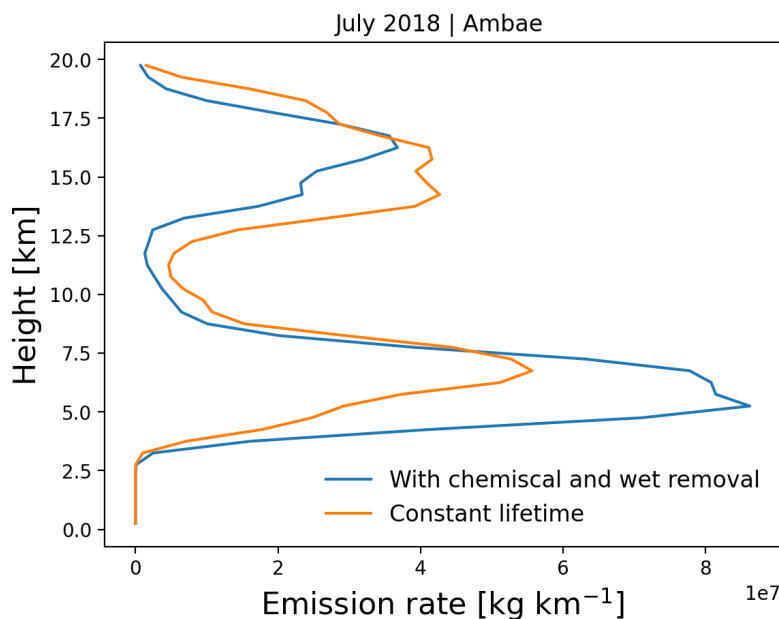


Figure 6.8: Vertical profiles of emission rates for the Ambae eruption in July 2018, estimated with chemistry and wet deposition modeling (blue curve) and with constant lifetime (orange curve).

6.3.2 Results

In chapter 5, the reconstruction of the emissions using the backward trajectory approach showed good consistency of the mass evolution and lifetime prediction compared to TROPOMI observations. In this section, we compare the reconstruction of the emissions using the proposed particle filter algorithm with the emissions derived with the backward trajectory method. The importance weight distributions in the parameter space and the reconstruction of the emissions are shown in Fig. 6.9.

Figure 6.10 and Fig. 6.11a show the altitude- and time-resolved emissions and vertical emission rate profiles for comparison. In this case, the reconstructions of the emissions have only one release peak located at about 8 to 12 km on June 21, 2019. The reconstructions using the two schemes show similar results, and the total residence time also turns out to be the same, as shown in Fig. 6.11b. These results indicate that when only a single emission peak exists, both the backward trajectory and the particle filter approaches can accurately identify the main release time and height distribution.

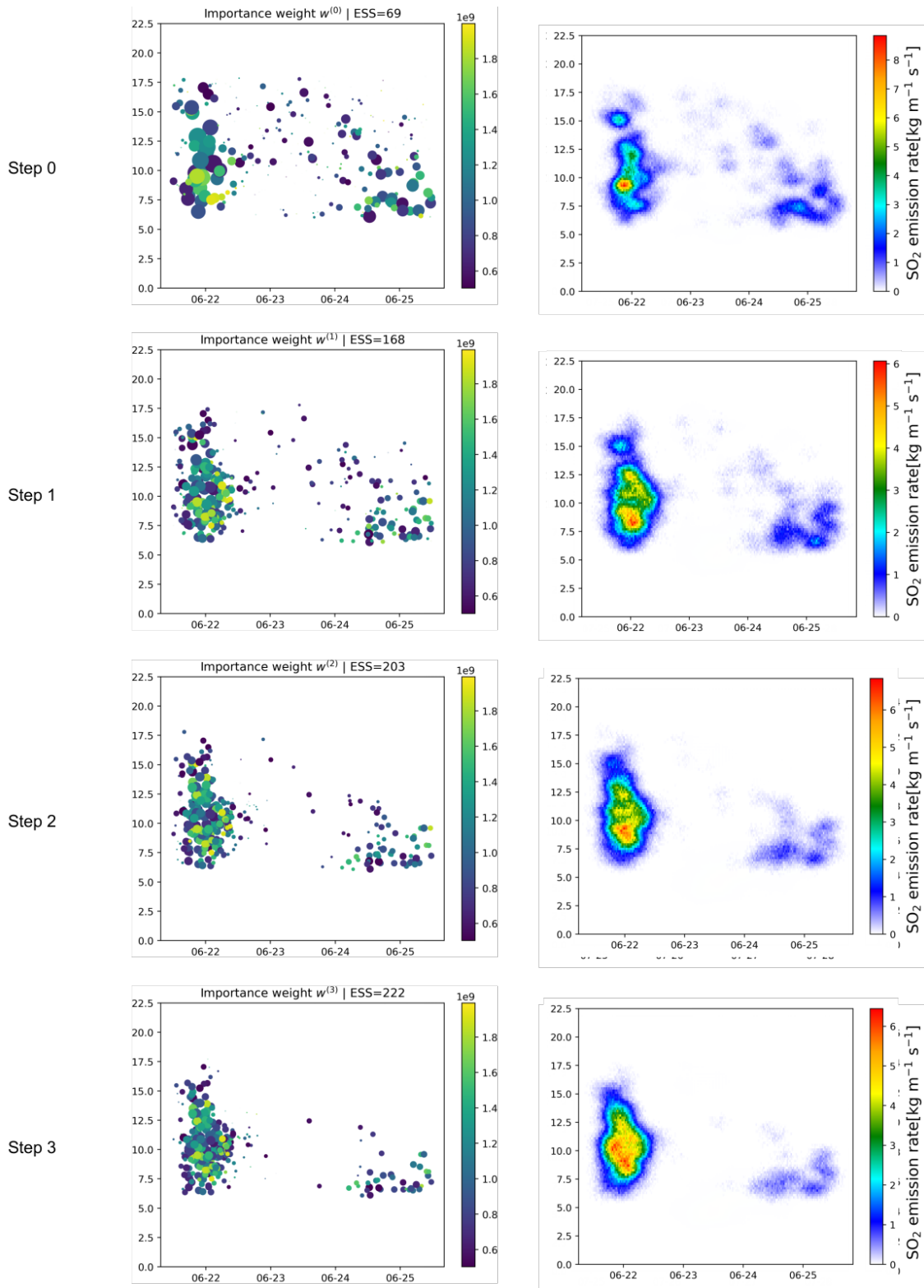


Figure 6.9: The importance weight distribution (left column) and the respective reconstruction of emissions (right column) for the Raikoke eruption in June 2019. The point size represents the importance weight of the sample.

6.3. Raikoke case study

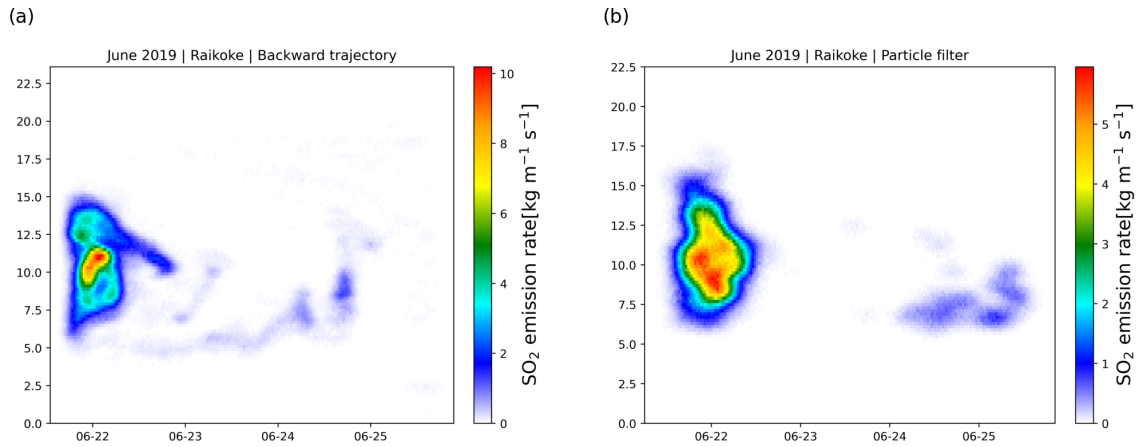


Figure 6.10: Altitude- and time- dependent emission rates of the Raikoke eruption in June 2019, reconstructed by the backward trajectory approach (a) and the particle filter approach (b).

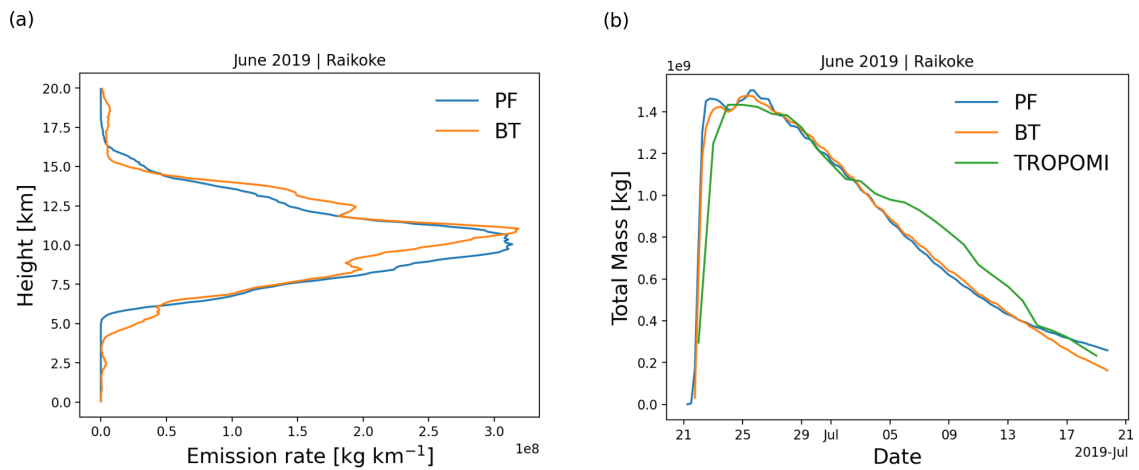


Figure 6.11: (a) Vertical profiles of emission rates estimated with the particle filter (PF) approach (blue curve) and backward trajectory (BT) approach (orange curve). (b) Temporal evolution of the SO_2 total mass from TROPOMI measurements (green curve) and MPTRAC simulations with initial release estimated with the particle filter approach (blue curve) and the backward trajectory approach (orange curve) for the Raikoke eruption in June 2019.

6.4 Discussion

In this chapter, we developed and applied an inverse modeling approach using a particle filter to reconstruct volcanic SO₂ emissions. The filter is constructed by employing a set of particles to represent the posterior distribution of the unknown source parameters of release time, release height and total release mass. The sampled particles x_k for $k = 1, \dots, N$ are transformed to $H(x_k)$ by simultaneously performing a series of forward simulations with the initial emissions constructed by the source parameters. The importance weights of the particles are formulated based on the likelihood function, which quantifies the agreement between the simulated and observed data. This particle filter approach effectively accounts for non-linear chemical processes in the model, providing an improved representation of the total residence time of SO₂ compared to the backward trajectory method. The particle filter framework enables a time- and altitude-resolved estimation of volcanic emissions, which is crucial for improving the accuracy of long-range transport models and subsequent environmental impact assessments.

The inverse modeling method was applied to two significant volcanic case studies: the 2018 Ambae eruption and the 2019 Raikoke eruption. Both case studies provided valuable insights into the complex relationship between chemical sink processes, such as OH oxidation and wet deposition, and the accuracy of the reconstructed emissions. The results showed that the particle filter method is highly sensitive to how these sink processes are represented in the forward model, highlighting the need for accurate chemistry modeling in inverse source estimation.

The comparison of the particle filter approach with traditional backward trajectory methods also yielded important insights. While backward trajectory methods are simpler and computationally less intensive, they often fail to account for the non-linear chemical decay processes that significantly influence SO₂ transport. In case when there are multiple release peaks, the backward trajectory tends to assign higher potential weight to the peaks at higher altitudes, since at higher altitudes the SO₂ residence time is longer and is more detectable and more sensitive to satellite instruments. By contrast, the particle filter approach, which incorporates these processes when conducting the forward simulation to formulate the posterior PDF distributions, consistently produces more accurate and detailed emission reconstructions, particularly in cases where the SO₂ plume undergoes significant chemical transformation.

Despite the advantages of the particle filter method, there remain some limitations that warrant further investigation. For example, the method assumes that the forward model used to simulate the transport and decay of SO₂ is reasonably accurate. Any significant bias or error in the forward model, such as inaccuracies in the meteorological input data or simplifications in the chemistry

6.4. Discussion

schemes, could propagate through the inversion and affect the final emission estimates. In this work, the error is formulated as the standard errors of the observations scaled by a assumed factor, which serves as a control parameter. This factor must be fine-tuned to obtain optimal results. However, the sensitivity of the emission reconstruction to variations in this parameter requires further testing in future work to better understand its influence on model performance and accuracy. Future work should also focus on refining the chemistry and physical processes within MPTRAC to minimize these uncertainties.

Another challenge is the computational cost associated with the particle filter approach. While the method provides a high degree of accuracy, the large number of particles required for reliable emission reconstructions can be computationally expensive, particularly for high-resolution simulations. In this work, we used a total particle size of 300, utilizing MPI parallelization to perform 300 forward simulations simultaneously with distribution memory. The scale of the model is significantly limited by memory as each forward simulation requires the input of meteorological data. In our tests on the JUWELS supercomputer, only 6 forward simulations could be run on a single node, requiring 50 nodes for each step. This limitation can be addressed in future work by optimizing the code to adopt a share memory approach, allowing meteorological data to be loaded once and used across all simulations. In this way, large scale applications on GPU will be possible.

Chapter 7

Summary

This thesis presents significant advancements in the Lagrangian transport model MPTRAC (Massive-Parallel Trajectory Calculations) for simulating the transport and chemical transformation of reactive trace gases in the atmosphere, with a focus on the long-lived tracers and volcanic sulfur dioxide (SO_2). Accurate modeling of atmospheric pollutants is critical for understanding their transport and environmental impacts, and for developing effective policies to mitigate their effects on human health and climate. The research develops and implements enhanced chemistry schemes in MPTRAC to improve the accuracy of simulating these processes.

This work involves the development of the chemistry schemes in MPTRAC, including the explicit and implicit chemistry schemes. The explicit chemistry scheme is designed to handle first-order reactions, making it computationally efficient for large-scale, long-term simulations. The study of the long-lived tracer simulations, including nitrous oxide (N_2O), CFC-11, and CFC-12, uses the explicit chemistry scheme to model the photolysis and O^1D oxidation. The simulated long-lived tracer distributions over a multi-year period are validated against satellite observations from the SPARC Data Initiative and MIPAS satellite measurements. The comparison shows that the MPTRAC model, equipped with the new chemistry and mixing schemes, can effectively reproduce the observed global patterns of these tracers. The mixing module, implemented by adding a relaxation term with a control parameter, is found to have a good effect on smoothing the large deviation among the neighboring air parcels.

In addition to the long-lived tracer simulations, the thesis focuses on the complex chemical interactions involved in volcanic SO_2 transport and depletion, which are applied to two case studies: the 2018 Ambae volcanic eruption in the South Pacific and the 2019 Raikoke eruption in the mid-latitudes. These case studies are critical for understanding the variability in SO_2 lifetime, which

depends strongly on atmospheric conditions, such as altitude, temperature, and the presence of clouds. The Ambae eruption injected a large amount of SO₂ into the tropical upper troposphere and lower stratosphere (UT/LS), where wet deposition played a dominant role in removing SO₂ from the atmosphere. The model's simulations show that the SO₂ lifetime was relatively short due to strong wet deposition processes in the tropical environment. In contrast, the Raikoke eruption, which injected SO₂ into the mid-latitude lower stratosphere, had a much longer SO₂ lifetime. The comparison between these two eruptions highlights the importance of accurately representing both gas-phase and aqueous-phase reactions in modeling SO₂ depletion.

Incorporating the developed chemistry schemes, this thesis develops a novel inverse modeling approach using a particle filter algorithm. This method allows for the reconstruction of time- and altitude-resolved SO₂ emissions from satellite observations by accounting for the non-linear chemical decay of SO₂. The particle filter approach is applied to both the Ambae and Raikoke eruptions, demonstrating its ability to improve emission source estimation, compared to traditional backward trajectory methods. Especially for the Ambae eruption case, the particle filter tends to assign a greater weight to the lower altitude release, resulting in a more consistent total residence time with observations.

In summary, this thesis makes significant contributions to the field of atmospheric transport modeling by extending the capabilities of the MPTRAC model to simulate both long-lived and reactive trace gases. The successful validation of long-lived tracers such as N₂O and CFCs establishes a reliable basis for further applications of the model, while the integration of advanced chemistry schemes for volcanic SO₂ transport and depletion allows for more accurate predictions of pollutant behavior in the atmosphere. The development of an inverse modeling approach for source reconstruction further strengthens the applicability of the model to real-world scenarios, such as volcanic eruptions, where timely and accurate predictions of pollutant dispersion are critical for public safety and environmental protection.

From this work, the MPTRAC model obtained significantly improved capabilities for Lagrangian chemistry modeling on current and upcoming HPC systems, opening many opportunities for future studies and applications. Future research could focus on extending the application of the chemistry schemes to other reactive trace gases, improving the computational efficiency of the implicit chemistry scheme, and incorporating real-time observational data for more accurate and immediate predictions during atmospheric pollution events. The broader implications of this research lie in its potential to improve decision making for climate policy and emergency response in the face of natural disasters and industrial pollution.

Appendix A

Validation of OH fields with diurnal variability

A monthly mean zonal mean OH climatology with diurnal corrections according to Eq. (2.19) is used as input to calculate the decomposition of SO₂ due to OH oxidation. For validation of the OH data, we extracted OH values from MPTRAC as a function of the solar zenith angle and compared them with in-situ measurement data provided by the NASA Earth Science Project Office (ESPO, 2022). Here, we present comparisons for April (Fig. A.1) and October (Fig. A.2) containing in-situ measurements of campaigns SUCCESS-DC8, SONEX-DC8, POLARIS-ER2, and MAESA-ER2, covering altitudes ranging from 5 to 21 km. For the stratosphere, a comparison with OH data from MLS is shown in Fig A.3. It is found that CLaMS OH data better represent the measured OH concentrations than the CAMS reanalysis in the stratosphere. For the troposphere, the OH data from CLaMS and CAMS both match the measurements well.

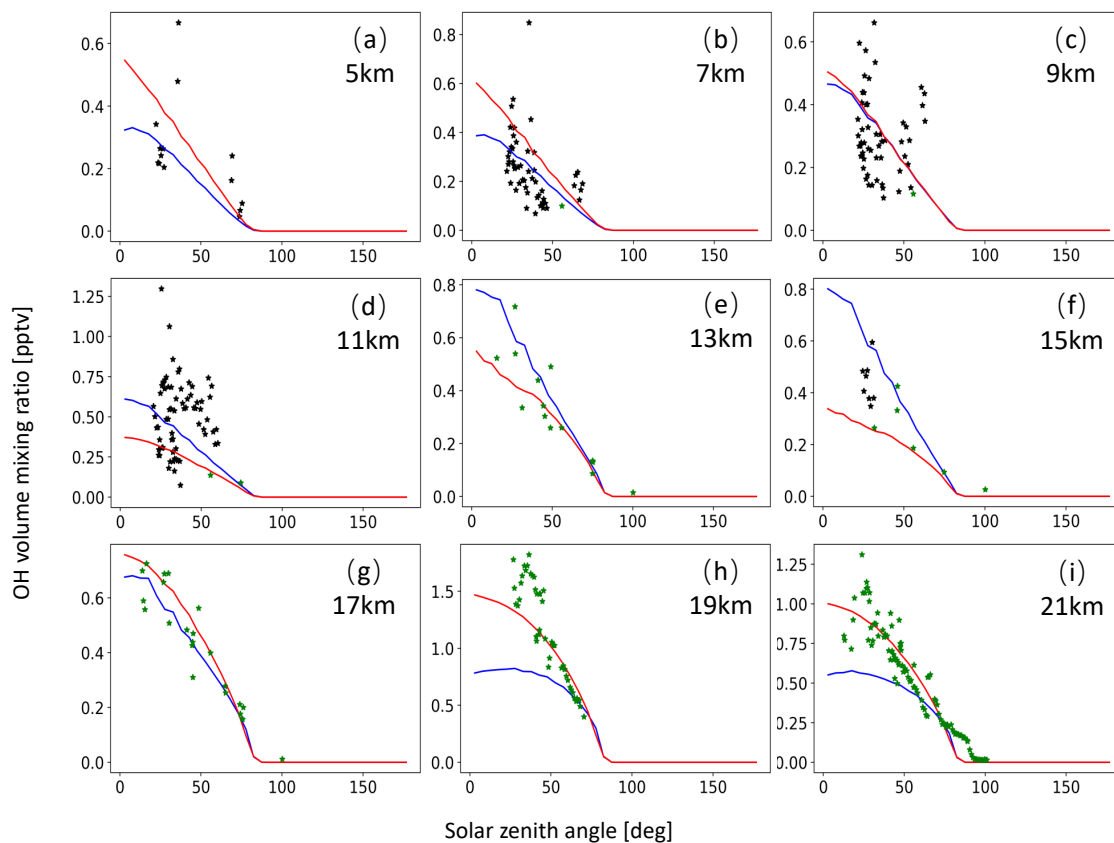


Figure A.1: OH volume mixing ratios used for MPTRAC based on predefined monthly mean zonal mean data for the CLaMS model (red curve) and the CAMS reanalysis (blue curve) as well as OH in-situ measurements from the campaigns SUCCESS-DC8 (black points) and POLARIS-ER2 (green points). The time period being covered is the month of April. Plots in (a) to (i) refer to altitudes of 5, 7, 9, 11, 13, 15, 17, 19, and 21 km, respectively.

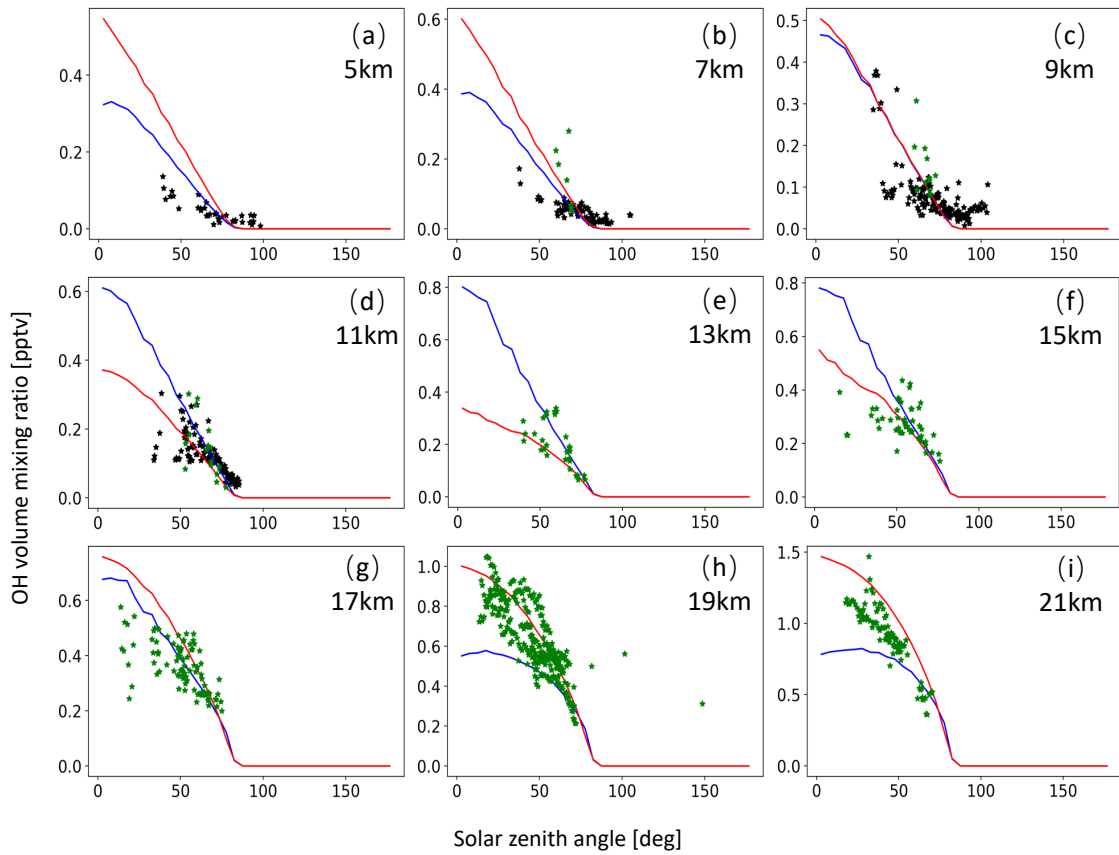


Figure A.2: Same as Fig. A.1 but for SONEX-DC8 (black points) and MAESA-ER2 (green points) measurements in October.

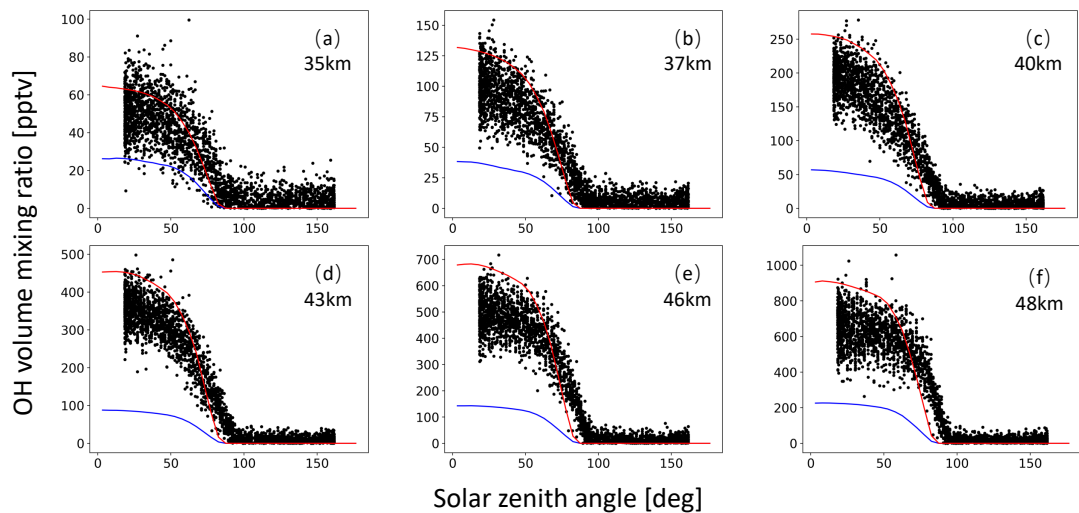


Figure A.3: Global average OH volume mixing ratios used in MPTRAC based on predefined monthly mean zonal mean data for the CLaMS model (red curve) and the CAMS reanalysis (blue curve) as well as MLS satellite measurements (black points). The time period being covered is May. Plots in (a) to (f) refer to altitudes of 35, 37, 40, 43, 46, and 48 km, respectively.

List of Figures

1.1	Diagram of the inverse modeling strategy.	10
1.2	Diagram for illustration of particle filter cited from Doucet et al. (2001). The diagram illustrates the process of particle resampling, propagation, and weight update in particle filtering. It shows how particles evolve over time, with resampling based on weights and how the distribution is represented by the particles.	14
2.1	Simplified flow chart of the Massive-Parallel Trajectory Calculations (MPTRAC) Lagrangian chemistry-transport model.	25
3.1	Global mean vertical VMR profiles of the long-lived tracer N ₂ O (a), CFC-11 (b), CFC-12 (c) in spin-up steps of 1, 5, 10 and 12.	31
3.2	Vertical VMR profiles of the MPTRAC simulations for N ₂ O (panels a, b, c), CFC-11 (panels d, e, f), and CFC-12 (panels g, h, i) in May 2011 for three latitude ranges: -20 to 20, 20 to 65, and 65 to 90 degrees, with different meteorological data from ERA5 (blue curves) and ERA-Interim (orange curves) reanalyses, compared with measurements from MIPAS (green curves) and ACE-FTS (red curves).	33
3.3	Vertical VMR profile of the long-lived tracer N ₂ O (a), CFC-11 (b), CFC-12 (c) in spin-up steps of 1, 5, 10 and 12.	33
3.4	Vertical VMR profiles of the MPTRAC simulations for N ₂ O (panels a, b, c), CFC-11 (panels d, e, f), and CFC-12 (panels g, h, i) for three latitude ranges: -20 to 20, 20 to 65, and 65 to 90 degrees, with different photolysis rate modeled by CLaMS (blue curves) and TUV (orange curves), compared with measurements from MIPAS (green curves) and ACE-FTS (red curves).	34

3.5	Comparison of simulated and observed VMR of N ₂ O at the 600±25 K potential temperature surface in the Antarctic region on December 9, 2011. Panel (a) and (b) shows the simulated distribution without and with mixing processes. Panel (c) shows the observed distribution of the MIPAS measurement.	35
3.6	Vertical standard deviation profiles of the MPTRAC simulations for CFC-11 for five latitude ranges in May, 2011: -90 to -65 (a), -65 to -20 (b), -20 to 20 (c), 20 to 65 (d), and 65 to 90 (e) degrees, with different parameter <i>d</i> controlling the mixing degree, compared with measurements from MIPAS data (purple curves).	36
3.7	Comparison of MIPAS satellite-observed (first row) and MPTRAC model-simulated (second row) N ₂ O distributions at different potential temperature levels of 400, 500, 600 and 700 K.	37
3.8	Comparison of MIPAS satellite-observed (first row) and MPTRAC model-simulated (second row) CFC-12 distributions at different potential temperature levels of 400, 500, 600 and 700 K.	38
3.9	Comparison of MIPAS satellite-observed (first row) and MPTRAC model-simulated (second row) CFC-11 distributions at different potential temperature levels of 400, 500, 600 and 700 K.	38
3.10	Contours of the MPTRAC-simulated and MIPAS-observed monthly mean long-lived tracer concentration distributions in 2011. The contour line value is the concentration in unit of 1×10^{-10} ppv. The black curves represent the MIPAS data and the color curves represent the MPTRAC simulated data.	39
4.1	Observed (TROPOMI) and simulated (MPTRAC) SO ₂ total mass curve (a) and mass loss (b) of the July 2018 Ambae eruption as a function of time. The blue shading represents the total error of the TROPOMI observations, combining random and systematic error components.	45
4.2	Evolution of the Ambae SO ₂ plume in AIRS SO ₂ observations (a) as well as column densities from TROPOMI observations (b) and MPTRAC simulation (c). The time of the satellite observations shown here was restricted to ±3 h around 00:00 UTC. The black triangle shows the location of Ambae island. MPTRAC simulation results have been sampled on the TROPOMI footprints.	46
4.3	SO ₂ mass loss relative to the total mass (in percent) due to OH chemistry (a), wet deposition (b), and H ₂ O ₂ chemistry (c) as well as total mass curves (d) derived from simulations with different release heights centered at 11, 13, 15, 17 and 19 km.	47

4.4	Background images represent the distributions of ERA5 cloud top height on 31 July 2018, 00:00 UTC. Dots represent air parcels released at altitudes of (a) 11 km, (b) 13 km, (c) 15 km, and (d) 17 km. A yellow dot indicates that the air parcel is below the cloud top height, triggering the wet deposition module, while a blue dot represents the opposite.	48
4.5	Same as Fig. 4.4, but background images represent the distribution of ERA5 CAPE values on 31 July 2018, 00:00 UTC. Yellow dots indicate air parcels below the equilibrium level and local CAPE values larger than 1000 J kg^{-1} , triggering the convection module, while blue dots represent the opposite.	49
4.6	Vertical profiles of (a) OH concentrations over the tropics retrieved from CLaMS and CAMS climatology data, respectively, on 26 July 2018, 00:00 UTC and (b) OH oxidation rate coefficients at the same time.	50
4.7	SO ₂ mass loss relative to total mass (in percent) due to the OH chemistry module (a) and total mass curves (b) for simulations with different OH datasets, including CLaMS data in 2005, CAMS data in 2005 and 2018, and CAMS regional data in 2018 (see text for details).	50
4.8	SO ₂ mass loss relative to total mass (in percent) due to the wet deposition module (a) and total mass curves (b), derived from simulations with different pH values in the wet deposition module and comparing with the wet deposition scheme of the NAME model.	51
4.9	SO ₂ mass loss relative to the total mass (in percent) due the wet deposition module(a) and total mass burden evolution (b), derived from different simulations with different retention ratios settings in the wet deposition module.	52
4.10	Vertical distribution of total SO ₂ mass of the air parcels on 1 August 2018, 00:00 UTC from simulations with different CAPE thresholds. The red dashed line indicates the ERA5 thermal tropopause height over the Ambae region (Hoffmann and Spang, 2022).	53
4.11	Same as Fig. 4.3, but derived from simulations with different CAPE thresholds in the convection module.	54
5.1	Vertical profile of SO ₂ injections of the Raikoke eruption as estimated by Cai et al. (2022). The red line represents the tropopause height at the location of the volcano.	58

5.2	Evolution of SO ₂ total column density distributions from 23 June 2019 to 30 June 2019 from the MPTRAC simulation with implicit chemistry scheme (right column) and TROPOMI satellite observations (left column). The red triangle marks the location of the Raikoke volcano.	59
5.3	Same as Fig. 5.2, but from 1 July 2019 to 7 July 2019.	60
5.4	Temporal evolution of the SO ₂ total mass burden of the 2019 Raikoke eruption from TROPOMI measurements (blue curve, shading shows uncertainty range) and MPTRAC simulations with explicit solution (orange curve), simplified explicit solution with correction (green curve), and KPP implicit solution (red curve).	61
5.5	Vertical profiles of the average SO ₂ e-folding lifetime of MPTRAC simulations with explicit solution (green curve), explicit solution with correction (orange curve) and KPP implicit solution (blue curve) during 25 June to 4 July.	62
5.6	Ratio of OH concentration in dry atmosphere (a) and H ₂ O ₂ concentration in cloud regions (b) in the Raikoke SO ₂ plume versus background levels as a function of the SO ₂ VMR. Each data point represents a single air parcel. The red curves represent the regression formulas given in Eqs. (5.1) and (5.2).	63
5.7	Zonal mean distributions of the OH field obtained from the CAMS reanalysis (blue curve), climatological data from the CLaMS model (green curve) and the MPTRAC simulation (orange curve) at pressure levels of 100 hPa (a), 150 hPa (b), 200 hPa (c) and 250 hPa (d) on 1 July 2019, 00:00 UTC.	64
5.8	Global OH fields obtained from the CAMS reanalysis (top) and MPTRAC simulations (bottom) at pressure levels of 100 hPa (a), 150 hPa (b), 200 hPa (c) and 250 hPa (d) on 1 July 2019, 00:00 UTC.	65
5.9	Total mass burden evolution simulated with different chemistry time step size settings of 3600, 7200, 10800, 21600, 43200 and 86400 seconds.	66
5.10	Computational costs of the Raikoke simulations with different chemistry schemes (the implicit scheme and the simplified explicit scheme with correction) on the JUWELS Cluster (CPU) and JUWELS Booster (GPU) for a simulation with 1 million air parcels on a scale of 1 million air parcels (a) and 3 million air parcels (b). The blue bar represents the runtime for the chemistry calculations, while the red bar represents the runtime for the other physical modules besides chemistry.	68

6.1	(a) The SO ₂ emissions reconstructed using the backward trajectory method. (b) The resulting SO ₂ mass evolution simulated with the initialization of SO ₂ emissions as shown in (a).	71
6.2	Flow chart of the proposed inverse modeling and simulation system to reconstruct the SO ₂ release parameters and emission rates.	73
6.3	The importance weight distribution (left column) and the respective reconstruction of emissions (right column) for the Ambae eruption in July 2018. The point size represents the importance weight of the sample.	75
6.4	Vertical profiles of emission rates at different steps of the inverse modeling process for the Ambae eruption in July 2018.	76
6.5	Vertical profiles of emission rates for the Ambae eruption in July 2018, estimated with the particle filter (PF) approach (blue curve) and backward trajectory (BW) approach (orange curve).	77
6.6	Temporal evolution of the SO ₂ total mass for the Ambae eruption in July 2018 from TROPOMI measurements (green curve) and MPTRAC simulations with initial release of emissions estimated with the particle filter approach (blue curve) and the backward trajectory approach (orange curve).	77
6.7	SO ₂ column density from TROPOMI observations (left column) and MPTRAC simulations using source emissions derived from the backward trajectory (BT, middle column) method and particle filter (PF, right column), respectively.	79
6.8	Vertical profiles of emission rates for the Ambae eruption in July 2018, estimated with chemistry and wet deposition modeling (blue curve) and with constant lifetime (orange curve).	80
6.9	The importance weight distribution (left column) and the respective reconstruction of emissions (right column) for the Raikoke eruption in June 2019. The point size represents the importance weight of the sample.	81
6.10	Altitude- and time- dependent emission rates of the Raikoke eruption in June 2019, reconstructed by the backward trajectory approach (a) and the particle filter approach (b).	82

6.11 (a) Vertical profiles of emission rates estimated with the particle filter (PF) approach (blue curve) and backward trajectory (BW) approach (orange curve). (b) Temporal evolution of the SO ₂ total mass from TROPOMI measurements (green curve) and MPTRAC simulations with initial release estimated with the particle filter approach (blue curve) and the backward trajectory approach (orange curve) for the Raikoke eruption in June 2019.	82
A.1 OH volume mixing ratios used for MPTRAC based on predefined monthly mean zonal mean data for the CLaMS model (red curve) and the CAMS reanalysis (blue curve) as well as OH in-situ measurements from the campaigns SUCCESS-DC8 (black points) and POLARIS-ER2 (green points). The time period being covered is the month of April. Plots in (a) to (i) refer to altitudes of 5, 7, 9, 11, 13, 15, 17, 19, and 21 km, respectively.	88
A.2 Same as Fig. A.1 but for SONEX-DC8 (black points) and MAESA-ER2 (green points) measurements in October.	89
A.3 Global average OH volume mixing ratios used in MPTRAC based on predefined monthly mean zonal mean data for the CLaMS model (red curve) and the CAMS reanalysis (blue curve) as well as MLS satellite measurements (black points). The time period being covered is May. Plots in (a) to (f) refer to altitudes of 35, 37, 40, 43, 46, and 48 km, respectively.	89

List of Tables

2.1	Proposed chemistry scheme for volcanic SO ₂ oxidation in the UT/LS region. . . .	26
-----	---	----

Bibliography

- Alvanos, M. and Christoudias, T.: GPU-accelerated atmospheric chemical kinetics in the ECHAM/MESSy (EMAC) Earth system model (version 2.52), *Geoscientific Model Development*, 10, 3679–3693, doi: 10.5194/gmd-10-3679-2017, 2017.
- Aumann, H., Chahine, M., Gautier, C., Goldberg, M., Kalnay, E., McMillin, L., Revercomb, H., Rosenkranz, P., Smith, W., Staelin, D., Strow, L., and Susskind, J.: AIRS/AMSU/HSB on the Aqua mission: design, science objectives, data products, and processing systems, *IEEE Transactions on Geoscience and Remote Sensing*, 41, 253–264, doi: 10.1109/TGRS.2002.808356, 2003.
- Becker, G., Grooß, J.-U., McKenna, D. S., and Müller, R.: Stratospheric photolysis frequencies: Impact of an improved numerical solution of the radiative transfer equation, *Journal of Atmospheric Chemistry*, 37, 217–229, doi: 10.1023/A:1006468926530, 2000.
- Berglen, T. F., Berntsen, T. K., Isaksen, I. S. A., and Sundet, J. K.: A global model of the coupled sulfur/oxidant chemistry in the troposphere: The sulfur cycle, *Journal of Geophysical Research: Atmospheres*, 109, doi: <https://doi.org/10.1029/2003JD003948>, 2004.
- Brenot, H., Theys, N., Clarisse, L., van Geffen, J., van Gent, J., van Roozendaal, M., van der A, R., Hurtmans, D., Coheur, P. F., Clerbaux, C., Valks, P., Hedelt, P., Prata, F., Rason, O., Sievers, K., and Zehner, C.: Support to Aviation Control Service (SACS): an online service for near-real-time satellite monitoring of volcanic plumes, *Natural Hazards and Earth System Sciences*, 14, 1099–1123, doi: 10.5194/nhess-14-1099-2014, 2014.
- Brunner, D.: Atmospheric Chemistry in Lagrangian Models—Overview, chap. 19, pp. 224–234, American Geophysical Union (AGU), doi: <https://doi.org/10.1029/2012GM001431>, 2012.
- Burkholder, J. B., Sander, S. P., J. Abbatt, J. R. B., Cappa, C., Crounse, J. D., Dibble, T. S., Huie, R. E., Kolb, C. E., Kurylo, M. J., Orkin, V. L., Percival, C. J., Wilmouth, D. M., and Wine, P. H.:

- Chemical kinetics and photochemical data for use in atmospheric studies: evaluation number 19, Tech. rep., Jet Propulsion Laboratory, Pasadena, URL <http://jpldataeval.jpl.nasa.gov/>, 2020.
- Cai, Z., Griessbach, S., and Hoffmann, L.: Improved estimation of volcanic SO₂ injections from satellite retrievals and Lagrangian transport simulations: the 2019 Raikoke eruption, *Atmospheric Chemistry and Physics*, 22, 6787–6809, doi: 10.5194/acp-22-6787-2022, 2022.
- Capponi, A., Harvey, N. J., Dacre, H. F., Beven, K., Saint, C., Wells, C., and James, M. R.: Refining an ensemble of volcanic ash forecasts using satellite retrievals: Raikoke 2019, *Atmospheric Chemistry and Physics*, 22, 6115–6134, doi: 10.5194/acp-22-6115-2022, 2022.
- Carn, S., Clarisse, L., and Prata, A.: Multi-decadal satellite measurements of global volcanic degassing, *Journal of Volcanology and Geothermal Research*, 311, 99–134, doi: <https://doi.org/10.1016/j.jvolgeores.2016.01.002>, 2016.
- Chipperfield, M. P., Liang, Q., Strahan, S. E., Morgenstern, O., Dhomse, S. S., Abraham, N. L., Archibald, A. T., Bekki, S., Braesicke, P., Genova, G. D., Fleming, E. L., Hardiman, S. C., Iachetti, D., Jackman, C. H., Kinnison, D. E., Marchand, M., Pitari, G. M., Pyle, J. A., Rozanov, E. V., Stenke, A., and Tummon, F.: Multimodel estimates of atmospheric lifetimes of long-lived ozone-depleting substances: Present and future, *Journal of Geophysical Research: Atmospheres*, 119, 2555 – 2573, URL <https://api.semanticscholar.org/CorpusID:45828308>, 2014.
- Chopin, N.: A Sequential Particle Filter Method for Static Models, *Biometrika*, 89, 539–551, URL <http://www.jstor.org/stable/4140600>, 2002.
- Christoudias, T., Kirfel, T., Kerkweg, A., Taraborrelli, D., Moulard, G.-E., Raffin, E., Azizi, V., Oord, G. v. d., and Werkhoven, B. v.: GPU Optimizations for Atmospheric Chemical Kinetics, in: *The International Conference on High Performance Computing in Asia-Pacific Region, HPCAsia '21*, p. 136–138, Association for Computing Machinery, New York, NY, USA, doi: 10.1145/3432261.3439863, 2021.
- Clemens, J., Ploeger, F., Konopka, P., Portmann, R., Sprenger, M., and Wernli, H.: Characterization of transport from the Asian summer monsoon anticyclone into the UTLS via shedding of low potential vorticity cutoffs, *Atmospheric Chemistry and Physics*, 22, 3841–3860, doi: 10.5194/acp-22-3841-2022, 2022.

- Clemens, J., Hoffmann, L., Vogel, B., Griebbach, S., and Thomas, N.: Implementation and evaluation of diabatic advection in the Lagrangian transport model MPTRAC 2.6, *Geoscientific Model Development*, 17, 4467–4493, doi: 10.5194/gmd-17-4467-2024, 2024.
- Collins, W., Johnson, C., and Derwent, R.: Tropospheric Ozone in a Global-Scale Three-Dimensional Lagrangian Model and Its Response to NO_x Emission Controls, *Journal of Atmospheric Chemistry*, 26, 223–274, doi: 10.1023/A:1005836531979, 1997.
- Damian, V., Sandu, A., Damian, M., Potra, F., and Carmichael, G. R.: The kinetic preprocessor KPP—a software environment for solving chemical kinetics, *Computers Chemical Engineering*, 26, 1567–1579, doi: 10.1016/S0098-1354(02)00128-X, 2002.
- de Leeuw, J., Schmidt, A., Witham, C. S., Theys, N., Taylor, I. A., Grainger, R. G., Pope, R. J., Haywood, J., Osborne, M., and Kristiansen, N. I.: The 2019 Raikoke volcanic eruption – Part 1: Dispersion model simulations and satellite retrievals of volcanic sulfur dioxide, *Atmospheric Chemistry and Physics*, 21, 10 851–10 879, doi: 10.5194/acp-21-10851-2021, 2021.
- Dee, D. P., Uppala, S. M., Simmons, A. J., Berrisford, P., Poli, P., Kobayashi, S., Andrae, U., Balmaseda, M. A., Balsamo, G., Bauer, P., Bechtold, P., Beljaars, A. C. M., van de Berg, L., Bidlot, J., Bormann, N., Delsol, C., Dragani, R., Fuentes, M., Geer, A. J., Haimberger, L., Healy, S. B., Hersbach, H., Hólm, E. V., Isaksen, L., Kållberg, P., Köhler, M., Matricardi, M., McNally, A. P., Monge-Sanz, B. M., Morcrette, J.-J., Park, B.-K., Peubey, C., de Rosnay, P., Tavolato, C., Thépaut, J.-N., and Vitart, F.: The ERA-Interim reanalysis: configuration and performance of the data assimilation system, *Quarterly Journal of the Royal Meteorological Society*, 137, 553–597, doi: 10.1002/qj.828, 2011.
- Delmelle, P., Stix, J., Baxter, P., Garcia-Alvarez, J., and Barquero, J.: Atmospheric dispersion, environmental effects and potential health hazard associated with the low-altitude gas plume of Masaya volcano, Nicaragua, *Bulletin of Volcanology*, 64, 423–434, doi: 10.1007/s00445-002-0221-6, 2002.
- Doucet, A., de Freitas, N., and Gordon, N.: An Introduction to Sequential Monte Carlo Methods, pp. 3–14, Springer New York, New York, NY, doi: 10.1007/978-1-4757-3437-9_1, 2001.
- Draxler, R. and Hess, G.: An overview of the HYSPLIT_4 modelling system for trajectories, dispersion and deposition, *Australian meteorological magazine*, 47, 295–308, 1998.

- Dutton, G., Hall, B., Dlugokencky, E., Lan, X., Madronich, M., Nance, J., and Petersen, K.: Combined Atmospheric Nitrous Oxide Dry Air Mole Fractions from the NOAA GML Halocarbons Sampling Network, 1977-2024, Version: 2024-02-21, doi: <https://doi.org/10.15138/GMZ7-2Q16>, 2024a.
- Dutton, G., Hall, B., Montzka, S., Nance, J., Clingan, S., and Petersen, K.: Combined Atmospheric Chlorofluorocarbon-11 Dry Air Mole Fractions from the NOAA GML Halocarbons Sampling Network, 1977-2024, Version: 2024-02-22, doi: <https://doi.org/10.15138/BVQ6-2S69>, 2024b.
- Dutton, G., Hall, B., Montzka, S., Nance, J., Clingan, S., and Petersen, K.: Combined Atmospheric Chlorofluorocarbon-12 Dry Air Mole Fractions from the NOAA GML Halocarbons Sampling Network, 1977-2024, Version: 2024-03-07, doi: <https://doi.org/10.15138/PJ63-H440>, 2024c.
- Eatough, D., Caka, F., and Farber, R.: The Conversion of SO₂ to Sulfate in the Atmosphere, *Israel Journal of Chemistry*, 34, 301–314, doi: <https://doi.org/10.1002/ijch.199400034>, 1994.
- Eckhardt, S., Prata, A. J., Seibert, P., Stebel, K., and Stohl, A.: Estimation of the vertical profile of sulfur dioxide injection into the atmosphere by a volcanic eruption using satellite column measurements and inverse transport modeling, *Atmospheric Chemistry and Physics*, 8, 3881–3897, doi: [10.5194/acp-8-3881-2008](https://doi.org/10.5194/acp-8-3881-2008), 2008.
- Elperin, T., Fominykh, A., and Krasovitev, B.: Precipitation scavenging of gaseous pollutants having arbitrary solubility in inhomogeneous atmosphere, *Meteorology and Atmospheric Physics*, 127, 205–216, doi: [10.1007/s00703-014-0358-9](https://doi.org/10.1007/s00703-014-0358-9), 2015.
- ESPO: ESPO data archive, URL <https://espoarchive.nasa.gov/archive/browse/>, 2022.
- Fischer, H., Birk, M., Blom, C., Carli, B., Carlotti, M., von Clarmann, T., Delbouille, L., Dudhia, A., Ehret, D., Endemann, M., Flaud, J. M., Gessner, R., Kleinert, A., Koopman, R., Langen, J., López-Puertas, M., Mosner, P., Nett, H., Oelhaf, H., Perron, G., Remedios, J., Ridolfi, M., Stiller, G., and Zander, R.: MIPAS: an instrument for atmospheric and climate research, *Atmospheric Chemistry and Physics*, 8, 2151–2188, doi: [10.5194/acp-8-2151-2008](https://doi.org/10.5194/acp-8-2151-2008), 2008.
- Franke, P., Lange, A. C., and Elbern, H.: Particle-filter-based volcanic ash emission inversion applied to a hypothetical sub-Plinian Eyjafjallajökull eruption using the Ensemble for Stochastic Integration of Atmospheric Simulations (ESIAS-chem) version 1.0, *Geoscientific Model Development*, 15, 1037–1060, doi: [10.5194/gmd-15-1037-2022](https://doi.org/10.5194/gmd-15-1037-2022), 2022.

- Garrett, T. J., Avey, L., Palmer, P. I., Stohl, A., Neuman, J. A., Brock, C. A., Ryerson, T. B., and Holloway, J. S.: Quantifying wet scavenging processes in aircraft observations of nitric acid and cloud condensation nuclei, *Journal of Geophysical Research: Atmospheres*, 111, doi: 10.1029/2006JD007416, 2006.
- Gerbig, C.: Applications of Lagrangian Modeling: Greenhouse Gases—Overview, chap. 13, pp. 144–148, American Geophysical Union (AGU), doi: <https://doi.org/10.1029/2012GM001420>, 2012.
- Gerbig, C., Lin, J. C., Wofsy, S. C., Daube, B. C., Andrews, A. E., Stephens, B. B., Bakwin, P. S., and Grainger, C. A.: Toward constraining regional-scale fluxes of CO₂ with atmospheric observations over a continent: 2. Analysis of COBRA data using a receptor-oriented framework, *Journal of Geophysical Research: Atmospheres*, 108, doi: <https://doi.org/10.1029/2003JD003770>, 2003.
- Gordon, N. J., Salmond, D., and Smith, A. F. M.: Novel approach to nonlinear/non-Gaussian Bayesian state estimation, URL <https://api.semanticscholar.org/CorpusID:12644877>, 1993.
- Gorkavyi, N., Krotkov, N. A., Li, C., Lait, L. R., Colarco, P. R., Carn, S. A., DeLand, M. T., Newman, P. A., Schoeberl, M. R., Taha, G., Torres, O., Vasilkov, A. P., and Joiner, J.: Tracking Aerosols and SO₂ Clouds From the Raikoke Eruption: 3D View From Satellite Observations, *Atmospheric Measurement Techniques*, doi: 10.5194/amt-14-7545-2021, 2021.
- Groß, J.-U., Konopka, P., and Müller, R.: Ozone Chemistry during the 2002 Antarctic Vortex Split, *J. Atmos. Sci.*, 62, 860–870, 2005.
- Hansell, A. and Oppenheimer, C.: Health hazards from volcanic gases: A systematic literature review, *Archives of Environmental Occupational Health*, 59, 628–639, doi: 10.1080/00039890409602947, 2004.
- Harvey, N. J., Dacre, H. F., Saint, C., Prata, A. T., Webster, H. N., and Grainger, R. G.: Quantifying the impact of meteorological uncertainty on emission estimates and the risk to aviation using source inversion for the Raikoke 2019 eruption, *Atmospheric Chemistry and Physics*, 22, 8529–8545, doi: 10.5194/acp-22-8529-2022, 2022.
- Hegglin, M. I., Tegtmeier, S., Anderson, J., Bourassa, A. E., Brohede, S., Degenstein, D., Froidevaux, L., Funke, B., Gille, J., Kasai, Y., Kyrölä, E. T., Lumpe, J., Murtagh, D., Neu, J. L., Pérot,

- K., Remsberg, E. E., Rozanov, A., Toohey, M., Urban, J., von Clarmann, T., Walker, K. A., Wang, H.-J., Arosio, C., Damadeo, R., Fuller, R. A., Lingenfelser, G., McLinden, C., Pendlebury, D., Roth, C., Ryan, N. J., Sioris, C., Smith, L., and Weigel, K.: Overview and update of the SPARC Data Initiative: comparison of stratospheric composition measurements from satellite limb sounders, *Earth System Science Data*, 13, 1855–1903, doi: 10.5194/essd-13-1855-2021, 2021.
- Heng, Y., Hoffmann, L., Griessbach, S., Roessler, T., and Stein, O.: Inverse transport modeling of volcanic sulfur dioxide emissions using large-scale simulations, *Geoscientific Model Development*, 9, 1627–1645, doi: {10.5194/gmd-9-1627-2016}, 2016.
- Henze, D. K., Hakami, A., and Seinfeld, J. H.: Development of the adjoint of GEOS-Chem, *Atmospheric Chemistry and Physics*, 7, 2413–2433, doi: 10.5194/acp-7-2413-2007, 2007.
- Hersbach, H., Bell, B., Berrisford, P., Hirahara, S., Horányi, A., Muñoz-Sabater, J., Nicolas, J., Peubey, C., Radu, R., Schepers, D., Simmons, A., Soci, C., Abdalla, S., Abellan, X., Balsamo, G., Bechtold, P., Biavati, G., Bidlot, J., Bonavita, M., De Chiara, G., Dahlgren, P., Dee, D., Diamantakis, M., Dragani, R., Flemming, J., Forbes, R., Fuentes, M., Geer, A., Haimberger, L., Healy, S., Hogan, R. J., Hólm, E., Janisková, M., Keeley, S., Laloyaux, P., Lopez, P., Lupu, C., Radnoti, G., de Rosnay, P., Rozum, I., Vamborg, F., Villaume, S., and Thépaut, J.-N.: The ERA5 global reanalysis, *Quarterly Journal of the Royal Meteorological Society*, 146, 1999–2049, doi: 10.1002/qj.3803, 2020.
- Hoffmann, L. and Spang, R.: An assessment of tropopause characteristics of the ERA5 and ERA-Interim meteorological reanalyses, *Atmospheric Chemistry and Physics*, 22, 4019–4046, doi: 10.5194/acp-22-4019-2022, 2022.
- Hoffmann, L., Griessbach, S., and Meyer, C. I.: Volcanic emissions from AIRS observations: detection methods, case study, and statistical analysis, in: *Remote Sensing of Clouds and the Atmosphere XIX; and Optics in Atmospheric Propagation and Adaptive Systems XVII*, edited by Comerón, A., Kassianov, E. I., Schäfer, K., Picard, R. H., Stein, K., and Gonglewski, J. D., vol. 9242, p. 924214, International Society for Optics and Photonics, SPIE, doi: 10.1117/12.2066326, 2014.
- Hoffmann, L., Baumeister, P. F., Cai, Z., Clemens, J., Griessbach, S., Günther, G., Heng, Y., Liu, M., Haghghi Mood, K., Stein, O., Thomas, N., Vogel, B., Wu, X., and Zou, L.: Massive-Parallel Trajectory Calculations version 2.2 (MPTRAC-2.2): Lagrangian transport simulations

- on graphics processing units (GPUs), *Geoscientific Model Development*, 15, 2731–2762, doi: 10.5194/gmd-15-2731-2022, 2022.
- Hoffmann, L., Konopka, P., Clemens, J., and Vogel, B.: Lagrangian transport simulations using the extreme convection parameterization: an assessment for the ECMWF reanalyses, *Atmospheric Chemistry and Physics*, 23, 7589–7609, doi: 10.5194/acp-23-7589-2023, 2023.
- Hoffmann, L., Haghghi Mood, K., Herten, A., Hrywniak, M., Kraus, J., Clemens, J., and Liu, M.: Accelerating Lagrangian transport simulations on graphics processing units: performance optimizations of Massive-Parallel Trajectory Calculations (MPTRAC) v2.6, *Geoscientific Model Development*, 17, 4077–4094, doi: 10.5194/gmd-17-4077-2024, 2024.
- Hoffmann, L., Roessler, T., Griessbach, S., Heng, Y., and Stein, O.: Lagrangian transport simulations of volcanic sulfur dioxide emissions: Impact of meteorological data products, *Journal of Geophysical Research: Atmospheres*, 121, 4651–4673, doi: {10.1002/2015JD023749}, 2016.
- Hoffmann, L., Guenther, G., Li, D., Stein, O., Wu, X., Griessbach, S., Heng, Y., Konopka, P., Mueller, R., Vogel, B., and Wright, J. S.: From ERA-Interim to ERA5: the considerable impact of ECMWF's next-generation reanalysis on Lagrangian transport simulations, *Atmospheric Chemistry and Physics*, 19, 3097–3124, doi: {10.5194/acp-19-3097-2019}, 2019.
- Höpfner, M., Boone, C. D., Funke, B., Glatthor, N., Grabowski, U., Günther, A., Kellmann, S., Kiefer, M., Linden, A., Lossow, S., Pumphrey, H. C., Read, W. G., Roiger, A., Stiller, G., Schlager, H., von Clarmann, T., and Wissmüller, K.: Sulfur dioxide (SO₂) from MIPAS in the upper troposphere and lower stratosphere 2002–2012, *Atmospheric Chemistry and Physics*, 15, 7017–7037, doi: 10.5194/acp-15-7017-2015, 2015.
- Hoppe, C. M., Hoffmann, L., Konopka, P., Groöß, J.-U., Ploeger, F., Günther, G., Jöckel, P., and Müller, R.: The implementation of the CLaMS Lagrangian transport core into the chemistry climate model EMAC 2.40.1: application on age of air and transport of long-lived trace species, *Geoscientific Model Development*, 7, 2639–2651, doi: 10.5194/gmd-7-2639-2014, 2014.
- Hutchinson, M., Oh, H., and Chen, W.-H.: A review of source term estimation methods for atmospheric dispersion events using static or mobile sensors, *Information Fusion*, 36, 130–148, doi: <https://doi.org/10.1016/j.inffus.2016.11.010>, 2017.
- Iman, R. L. and Conover, W.: Small sample sensitivity analysis techniques for computer mod-

- els.with an application to risk assessment, *Communications in Statistics - Theory and Methods*, 9, 1749–1842, doi: 10.1080/03610928008827996, 1980.
- Inness, A., Ades, M., Agusti-Panareda, A., Barre, J., Benedictow, A., Blechschmidt, A.-M., Dominguez, J. J., Engelen, R., Eskes, H., Flemming, J., Huijnen, V., Jones, L., Kipling, Z., Massart, S., Parrington, M., Pench, V.-H., Razinger, M., Remy, S., Schulz, M., and Suttie, M.: The CAMS reanalysis of atmospheric composition, *Atmospheric Chemistry and Physics*, 19, 3515–3556, doi: 10.5194/acp-19-3515-2019, 2019.
- Iribarne, J., Barrie, L., and Iribarne, A.: Effect of freezing on sulfur dioxide dissolved in supercooled droplets, *Atmospheric Environment (1967)*, 17, 1047–1050, doi: [https://doi.org/10.1016/0004-6981\(83\)90287-1](https://doi.org/10.1016/0004-6981(83)90287-1), 1983.
- Iribarne, J., Pyshnov, T., and Naik, B.: The effect of freezing on the composition of supercooled droplets—II. Retention of S(IV), *Atmospheric Environment. Part A. General Topics*, 24, 389–398, doi: [https://doi.org/10.1016/0960-1686\(90\)90119-8](https://doi.org/10.1016/0960-1686(90)90119-8), 1990.
- Jülich Supercomputing Centre: JUWELS: Modular Tier-0/1 Supercomputer at the Jülich Supercomputing Centre, *J. Large-scale Res. Facilities*, 5, A135, doi: 10.17815/jlsrf-5-171, 2019.
- Jülich Supercomputing Centre: JUWELS Cluster and Booster: Exascale Pathfinder with Modular Supercomputing Architecture at Jülich Supercomputing Centre, *J. Large-scale Res. Facilities*, 7, A183, doi: 10.17815/jlsrf-7-183, 2021.
- Khokhar, M., Frankenberg, C., Van Roozendael, M., Beirle, S., Köhl, S., Richter, A., Platt, U., and Wagner, T.: Satellite observations of atmospheric SO₂ from volcanic eruptions during the time-period of 1996–2002, *Advances in Space Research*, 36, 879–887, doi: <https://doi.org/10.1016/j.asr.2005.04.114>, 2005.
- Kloss, C., Sellitto, P., Legras, B., Vernier, J.-P., Jegou, F., Venkat Ratnam, M., Suneel Kumar, B., Lakshmi Madhavan, B., and Berthet, G.: Impact of the 2018 Ambae Eruption on the Global Stratospheric Aerosol Layer and Climate, *Journal of Geophysical Research: Atmospheres*, 125, doi: 10.1029/2020JD032410, 2020.
- Kloss, C., Berthet, G., Sellitto, P., Ploeger, F., Taha, G., Tidiga, M., Eremenko, M., Bossolasco, A., Jégou, F., Renard, J., and Legras, B.: Stratospheric Aerosol Layer Perturbation Caused by the 2019 Raikoke and Ulawun Eruptions and Their Radiative Forcing, *Atmospheric Chemistry and Physics*, doi: 10.5194/acp-21-535-2021, 2021.

- Ko, M. K. W., Sze, N. D., and Weisenstein, D. K.: Use of satellite data to constrain the model-calculated atmospheric lifetime for N₂O - Implications for other trace gases, *Journal of Geophysical Research*, 96, 7547–7552, URL <https://api.semanticscholar.org/CorpusID:128681170>, 1991.
- Koch, D., Jacob, D., Tegen, I., Rind, D., and Chin, M.: Tropospheric sulfur simulation and sulfate direct radiative forcing in the Goddard Institute for Space Studies general circulation model, *Journal of Geophysical Research: Atmospheres*, 104, 23 799–23 822, doi: <https://doi.org/10.1029/1999JD900248>, 1999.
- Konopka, P., Ploeger, F., and Müller, R.: Entropy-Based and Static Stability–Based Lagrangian Model Grids, chap. 10, pp. 99–110, American Geophysical Union (AGU), doi: <https://doi.org/10.1029/2012GM001253>, 2012.
- Krippner, J. and Venzke, E.: Global Volcanism Program, 2019. Report on Ambae (Vanuatu), URL <https://doi.org/10.5479/si.GVP.BGVN201902-257030>, 2019.
- Kristiansen, N. I., Stohl, A., Prata, A. J., Richter, A., Eckhardt, S., Seibert, P., Hoffmann, A., Ritter, C., Bitar, L., Duck, T. J., and Stebel, K.: Remote sensing and inverse transport modeling of the Kasatochi eruption sulfur dioxide cloud, *Journal of Geophysical Research: Atmospheres*, 115, doi: <https://doi.org/10.1029/2009JD013286>, 2010.
- Kristiansen, N. I., Stohl, A., Prata, A. J., Bukowiecki, N., Dacre, H., Eckhardt, S., Henne, S., Hort, M. C., Johnson, B. T., Marengo, F., Neininger, B., Reitebuch, O., Seibert, P., Thomson, D. J., Webster, H. N., and Weinzierl, B.: Performance assessment of a volcanic ash transport model mini-ensemble used for inverse modeling of the 2010 Eyjafjallajökull eruption, *Journal of Geophysical Research: Atmospheres*, 117, doi: <https://doi.org/10.1029/2011JD016844>, 2012.
- Kristiansen, N. I., Prata, A. J., Stohl, A., and Carn, S. A.: Stratospheric volcanic ash emissions from the 13 February 2014 Kelut eruption, *Geophysical Research Letters*, 42, 588–596, doi: <https://doi.org/10.1002/2014GL062307>, 2015.
- Kristiansen, N. I., Witham, C., and Beckett, F.: Quantifying the Hazard From Volcanic Sulphur Dioxide to Aircraft Occupants, doi: [10.21203/rs.3.rs-2397636/v1](https://doi.org/10.21203/rs.3.rs-2397636/v1), 2023.
- Lamb, D. and Blumenstein, R.: Measurement of the entrapment of sulfur dioxide by rime ice, *Atmospheric Environment* (1967), 21, 1765–1772, doi: [https://doi.org/10.1016/0004-6981\(87\)90116-8](https://doi.org/10.1016/0004-6981(87)90116-8), 1987.

- Lary, D. J. and Pyle, J. A.: Diffuse radiation, twilight, and photochemistry — I, *Journal of Atmospheric Chemistry*, 13, 373–392, URL <https://api.semanticscholar.org/CorpusID:55982442>, 1991.
- Levine, S. and Schwartz, S.: In-cloud and below-cloud scavenging of Nitric acid vapor, *Atmospheric Environment*, 16, 1725–1734, doi: [https://doi.org/10.1016/0004-6981\(82\)90266-9](https://doi.org/10.1016/0004-6981(82)90266-9), 1982.
- Liao, Y., Deng, X., Huang, M., Liu, M., Yi, J., and Hoffmann, L.: Tracking Carbon Dioxide with Lagrangian Transport Simulations: Case Study of Canadian Forest Fires in May 2021, *Atmosphere*, 15, doi: [10.3390/atmos15040429](https://doi.org/10.3390/atmos15040429), 2024.
- Liu, J. S. and Chen, R.: Sequential Monte Carlo Methods for Dynamic Systems, *Journal of the American Statistical Association*, 93, 1032–1044, doi: [10.1080/01621459.1998.10473765](https://doi.org/10.1080/01621459.1998.10473765), 1998.
- Liu, M., Huang, Y., Hoffmann, L., Huang, C., Chen, P., and Heng, Y.: High-Resolution Source Estimation of Volcanic Sulfur Dioxide Emissions Using Large-Scale Transport Simulations, in: *Computational Science – ICCS 2020*, edited by Krzhizhanovskaya, V. V., Závodszky, G., Lees, M. H., Dongarra, J. J., Sloot, P. M. A., Brissos, S., and Teixeira, J., pp. 60–73, Springer International Publishing, doi: [10.1007/978-3-030-50420-5_5](https://doi.org/10.1007/978-3-030-50420-5_5), 2020.
- Liu, M., Hoffmann, L., Griessbach, S., Cai, Z., Heng, Y., and Wu, X.: Improved representation of volcanic sulfur dioxide depletion in Lagrangian transport simulations: a case study with MPTRAC v2.4, *Geoscientific Model Development*, 16, 5197–5217, doi: [10.5194/gmd-16-5197-2023](https://doi.org/10.5194/gmd-16-5197-2023), 2023.
- Liu, M., Hoffmann, L., Grooß, J.-U., Cai, Z., Grießbach, S., and Heng, Y.: Technical note: A comparative study of chemistry schemes for volcanic sulfur dioxide in Lagrangian transport simulations: a case study of the 2019 Raikoke eruption, *EGUsphere*, 2024, 1–25, doi: [10.5194/egusphere-2024-2596](https://doi.org/10.5194/egusphere-2024-2596), 2024.
- Maaß, F., Elias, H., and Wannowius, K. J.: Kinetics of the oxidation of hydrogen sulfite by hydrogen peroxide in aqueous solution:: ionic strength effects and temperature dependence, *Atmospheric Environment*, 33, 4413–4419, doi: [https://doi.org/10.1016/S1352-2310\(99\)00212-5](https://doi.org/10.1016/S1352-2310(99)00212-5), 1999.
- Madronich, S.: Photodissociation in the atmosphere: 1. Actinic flux and the effects of ground reflections and clouds, *Journal of Geophysical Research: Atmospheres*, 92, 9740–9752, 1987.

- Malinina, E., Rozanov, A., Niemeier, U., Wallis, S., Arosio, C., Wrana, F., Timmreck, C., von Savigny, C., and Burrows, J. P.: Changes in stratospheric aerosol extinction coefficient after the 2018 Ambae eruption as seen by OMPS-LP and MAECHAM5-HAM, *Atmospheric Chemistry and Physics*, 21, 14 871–14 891, doi: 10.5194/acp-21-14871-2021, 2021.
- Martin, A.: Estimated washout coefficients for sulphur dioxide, nitric oxide, nitrogen dioxide and ozone, *Atmospheric Environment*, 18, 1955–1961, doi: [https://doi.org/10.1016/0004-6981\(84\)90373-1](https://doi.org/10.1016/0004-6981(84)90373-1), cACGP Symposium on Tropospheric Chemistry With Emphasis on Sulphur and Nitrogen Cycles and the Chemistry of Clouds and Precipitation, 1984.
- Maul, P.: Preliminary estimates of the washout coefficient for sulphur dioxide using data from an east midlands ground level monitoring network, *Atmospheric Environment*, 12, 2515–2517, doi: [https://doi.org/10.1016/0004-6981\(78\)90298-6](https://doi.org/10.1016/0004-6981(78)90298-6), 1978.
- McGonigle, A. J. S., Delmelle, P., Oppenheimer, C., Tsanev, V. I., Delfosse, T., Williams-Jones, G., Horton, K., and Mather, T. A.: SO₂ depletion in tropospheric volcanic plumes, *Geophysical Research Letters*, 31, doi: <https://doi.org/10.1029/2004GL019990>, 2004.
- McKenna, D. S., Konopka, P., Groöß, J.-U., Günther, G., Müller, R., Spang, R., Offermann, D., and Orsolini, Y.: A new Chemical Lagrangian Model of the Stratosphere (CLaMS) 1. Formulation of advection and mixing, *Journal of Geophysical Research: Atmospheres*, 107, ACH 15–1–ACH 15–15, doi: <https://doi.org/10.1029/2000JD000114>, 2002.
- Minschwaner, K., Manney, G. L., Wang, S. H., and Harwood, R. S.: Hydroxyl in the stratosphere and mesosphere - Part 1: Diurnal variability, *Atmospheric Chemistry and Physics*, 11, 955–962, doi: 10.5194/acp-11-955-2011, 2011.
- Moussallam, Y., Rose-Koga, E. F., Koga, K. T., Medard, E., Bani, P., Devidal, J.-L., and Tari, D.: Fast ascent rate during the 2017-2018 Plinian eruption of Ambae (Aoba) volcano: a petrological investigation, *Contrib. to Mineral. Petrol.*, 174, doi: 10.1007/s00410-019-1625-z, 2019.
- Pardini, F., Burton, M., de' Michieli Vitturi, M., Corradini, S., Salerno, G., Merucci, L., and Di Grazia, G.: Retrieval and intercomparison of volcanic SO₂ injection height and eruption time from satellite maps and ground-based observations, *Journal of Volcanology and Geothermal Research*, 331, 79–91, doi: <https://doi.org/10.1016/j.jvolgeores.2016.12.008>, 2017.
- Pattantyus, A. K., Businger, S., and Howell, S. G.: Review of sulfur dioxide to sulfate aerosol

- chemistry at Kilauea Volcano, Hawai'i, *Atmospheric Environment*, 185, 262–271, doi: 10.1016/j.atmosenv.2018.04.055, 2018.
- Pisso, I., Sollum, E., Grythe, H., Kristiansen, I. N., Cassiani, M., Eckhardt, S., Arnold, D., Morton, D., Thompson, R. L., Zwaftink, C. D. G., Evangeliou, N., Sodemann, H., Haimberger, L., Henne, S., Brunner, D., Burkhardt, J. F., Fouilloux, A., Brioude, J., Philipp, A., Seibert, P., and Stohl, A.: The Lagrangian particle dispersion model FLEXPART version 10.4, *Geoscientific Model Development*, 12, 4955–4997, doi: 10.5194/gmd-12-4955-2019, 2019.
- Ploeger, F., Diallo, M., Charlesworth, E., Konopka, P., Legras, B., Laube, J. C., Grooß, J.-U., Günther, G., Engel, A., and Riese, M.: The stratospheric Brewer–Dobson circulation inferred from age of air in the ERA5 reanalysis, *Atmospheric Chemistry and Physics*, 21, 8393–8412, doi: 10.5194/acp-21-8393-2021, 2021.
- Pommrich, R., Müller, R., Grooß, J.-U., Konopka, P., Ploeger, F., Vogel, B., Tao, M., Hoppe, C. M., Günther, G., Spelten, N., Hoffmann, L., Pumphrey, H.-C., Viciani, S., D'Amato, F., Volk, C. M., Hoor, P., Schlager, H., and Riese, M.: Tropical troposphere to stratosphere transport of carbon monoxide and long-lived trace species in the Chemical Lagrangian Model of the Stratosphere (CLaMS), *Geoscientific Model Development*, 7, 2895–2916, doi: 10.5194/gmd-7-2895-2014, 2014.
- Prather, M. J., Hsu, J., DeLuca, N. M., Jackman, C. H., Oman, L. D., Douglass, A. R., Fleming, E. L., Strahan, S. E., Steenrod, S. D., Søvde, O. A., Isaksen, I. S. A., Froidevaux, L., and Funke, B.: Measuring and modeling the lifetime of nitrous oxide including its variability, *Journal of Geophysical Research: Atmospheres*, 120, 5693–5705, doi: <https://doi.org/10.1002/2015JD023267>, 2015.
- Ravishankara, A. R., Daniel, J. S., and Portmann, R. W.: Nitrous Oxide (N₂O): The Dominant Ozone-Depleting Substance Emitted in the 21st Century, *Science*, 326, 123–125, doi: 10.1126/science.1176985, 2009.
- Redington, A., Derwent, R., Witham, C., and Manning, A.: Sensitivity of modelled sulphate and nitrate aerosol to cloud, pH and ammonia emissions, *Atmospheric Environment*, 43, 3227–3234, doi: <https://doi.org/10.1016/j.atmosenv.2009.03.041>, 2009.
- Rieger, V. S., Mertens, M., and Grewe, V.: An advanced method of contributing emissions to short-lived chemical species (OH and HO₂): the TAGGING 1.1 submodel

- based on the Modular Earth Submodel System (MESSy 2.53), *Geoscientific Model Development*, 11, 2049–2066, doi: 10.5194/gmd-11-2049-2018, 2018.
- Robock, A.: Volcanic eruptions and climate, *Reviews of Geophysics*, 38, 191–219, doi: 10.1029/1998RG000054, 2000.
- Rolph, G., Draxler, R., and Depena, R.: Modeling Sulfur Concentrations and Depositions in the United-States During Anatex, *Atmospheric Environment*, 26, 73–93, doi: 10.1016/0960-1686(92)90262-J, 1992.
- Röbber, T., Stein, O., Heng, Y., Baumeister, P., and Hoffmann, L.: Trajectory errors of different numerical integration schemes diagnosed with the MPTRAC advection module driven by ECMWF operational analyses, *Geoscientific Model Development*, 11, 575–592, doi: 10.5194/gmd-11-575-2018, 2018.
- SACS: Support to Aviation Control Service, URL <https://sacs.aeronomie.be>, 2022.
- Sander, R.: Compilation of Henry's law constants (version 4.0) for water as solvent, *Atmospheric Chemistry and Physics*, 15, 4399–4981, doi: 10.5194/acp-15-4399-2015, 2015.
- Sander, R., Baumgaertner, A., Cabrera-Perez, D., Frank, F., Gromov, S., Grooß, J.-U., Harder, H., Huijnen, V., Jöckel, P., Karydis, V. A., Niemeyer, K. E., Pozzer, A., Riede, H., Schultz, M. G., Taraborrelli, D., and Tauer, S.: The community atmospheric chemistry box model CAABA/MECCA-4.0, *Geoscientific Model Development*, 12, 1365–1385, doi: 10.5194/gmd-12-1365-2019, 2019.
- Sandu, A. and Sander, R.: Technical note: Simulating chemical systems in Fortran90 and Matlab with the Kinetic PreProcessor KPP-2.1, *Atmospheric Chemistry and Physics*, 6, 187–195, doi: 10.5194/acp-6-187-2006, 2006.
- Schaefer, J. T.: The Critical Success Index as an Indicator of Warning Skill, *Weather and Forecasting*, 5, 570 – 575, doi: 10.1175/1520-0434(1990)005<0570:TCSIAA>2.0.CO;2, 1990.
- Schmidt, A., Ostro, B., Carslaw, K. S., Wilson, M., Thordarson, T., Mann, G. W., and Simmons, A. J.: Excess mortality in Europe following a future Laki-style Icelandic eruption, *Proceedings of the National Academy of Sciences of the United States of America*, 108, 15 710–15 715, doi: 10.1073/pnas.1108569108, 2011.

- Seibert, P.: Inverse Modelling of Sulfur Emissions in Europe Based on Trajectories, pp. 147–154, American Geophysical Union (AGU), doi: <https://doi.org/10.1029/GM114p0147>, 2000.
- Seinfeld, J. H. and Pandis, S. N.: Atmospheric chemistry and physics: from air pollution to climate change, John Wiley & Sons, 2016.
- Singh, S. K., Sharan, M., and Issartel, J.-P.: Inverse modelling methods for identifying unknown releases in emergency scenarios: an overview, *International Journal of Environment and Pollution*, 57, 68–91, doi: 10.1504/IJEP.2015.072121, 2015.
- Slinn, W. G. N.: Rate-Limiting Aspects of In-Cloud Scavenging, *Journal of the Atmospheric Sciences*, 31, 1172 – 1173, doi: 10.1175/1520-0469(1974)031<1172:RLAIOC>2.0.CO;2, 1974.
- Solomon, S.: Stratospheric ozone depletion: A review of concepts and history, *Reviews of Geophysics*, 37, 275–316, doi: <https://doi.org/10.1029/1999RG900008>, 1999.
- Stavrakou, T., Müller, J.-F., Boersma, K. F., van der A, R. J., Kurokawa, J., Ohara, T., and Zhang, Q.: Key chemical NO_x sink uncertainties and how they influence top-down emissions of nitrogen oxides, *Atmospheric Chemistry and Physics*, 13, 9057–9082, doi: 10.5194/acp-13-9057-2013, 2013.
- Stein, A. F., Lamb, D., and Draxler, R. R.: Incorporation of detailed chemistry into a three-dimensional Lagrangian–Eulerian hybrid model: application to regional tropospheric ozone, *Atmospheric Environment*, 34, 4361–4372, doi: [https://doi.org/10.1016/S1352-2310\(00\)00204-1](https://doi.org/10.1016/S1352-2310(00)00204-1), 2000.
- Stevenson, D. S., Collins, W. J., Johnson, C. E., and Derwent, R. G.: Intercomparison and evaluation of atmospheric transport in a Lagrangian model (STOCHEM), and an Eulerian model (UM), using ²²²Rn as a short-lived tracer, *Quarterly Journal of the Royal Meteorological Society*, 124, 2477–2491, doi: <https://doi.org/10.1002/qj.49712455115>, 1998.
- Stohl, A., Forster, C., Frank, A., Seibert, P., and Wotawa, G.: Technical note: The Lagrangian particle dispersion model FLEXPART version 6.2, *Atmospheric Chemistry and Physics*, 5, 2461–2474, doi: 10.5194/acp-5-2461-2005, 2005.
- Stuart, A. L. and Jacobson, M.: A numerical model of the partitioning of trace chemical solutes during drop freezing, *Journal of Atmospheric Chemistry*, 53, 13–42, 2006.

- Tan, Z., Lu, K., Hofzumahaus, A., Fuchs, H., Bohn, B., Holland, F., Liu, Y., Rohrer, F., Shao, M., Sun, K., Wu, Y., Zeng, L., Zhang, Y., Zou, Q., Kiendler-Scharr, A., Wahner, A., and Zhang, Y.: Experimental budgets of OH, HO₂, and RO₂ radicals and implications for ozone formation in the Pearl River Delta in China 2014, *Atmospheric Chemistry and Physics*, 19, 7129–7150, doi: 10.5194/acp-19-7129-2019, 2019.
- Theys, N., De Smedt, I., Yu, H., Danckaert, T., van Gent, J., Hoermann, C., Wagner, T., Hedelt, P., Bauer, H., Romahn, F., Pedergnana, M., Loyola, D., and Van Roozendaal, M.: Sulfur dioxide retrievals from TROPOMI onboard Sentinel-5 Precursor: algorithm theoretical basis, *Atmospheric Measurement Techniques*, 10, 119–153, doi: 10.5194/amt-10-119-2017, 2017.
- Theys, N., Romahn, F., and Wagner, T.: S5P Mission Performance Centre Sulphur Dioxide Readme, URL <https://sentinel.esa.int/documents/247904/3541451/Sentinel-5P-Sulphur-Dioxide-Readme.pdf>, 2020.
- Tian, H., Xu, R., Canadell, J. G., Thompson, R. L., Winiwarter, W., Suntharalingam, P., Davidson, E. A., Ciais, P., Jackson, R. B., Janssens-Maenhout, G., et al.: A comprehensive quantification of global nitrous oxide sources and sinks, *Nature*, 586, 248–256, 2020.
- Tie, X., Madronich, S., Walters, S., Zhang, R., Rasch, P., and Collins, W.: Effect of clouds on photolysis and oxidants in the troposphere, *Journal of Geophysical Research: Atmospheres*, 108, doi: <https://doi.org/10.1029/2003JD003659>, 2003.
- van Leeuwen, P. J.: Particle Filtering in Geophysical Systems, *Monthly Weather Review*, 137, 4089 – 4114, doi: 10.1175/2009MWR2835.1, 2009.
- van Leeuwen, P. J., Künsch, H. R., Nerger, L., Potthast, R., and Reich, S.: Particle filters for high-dimensional geoscience applications: A review, *Quarterly Journal of the Royal Meteorological Society*, 145, 2335–2365, doi: <https://doi.org/10.1002/qj.3551>, 2019.
- Veefkind, J., Aben, I., McMullan, K., Förster, H., de Vries, J., Otter, G., Claas, J., Eskes, H., de Haan, J., Kleipool, Q., van Weele, M., Hasekamp, O., Hoogeveen, R., Landgraf, J., Snel, R., Tol, P., Ingmann, P., Voors, R., Kruizinga, B., Vink, R., Visser, H., and Levelt, P.: TROPOMI on the ESA Sentinel-5 Precursor: A GMES mission for global observations of the atmospheric composition for climate, air quality and ozone layer applications, *Remote Sensing of Environment*, 120, 70–83, doi: <https://doi.org/10.1016/j.rse.2011.09.027>, the Sentinel Missions - New Opportunities for Science, 2012.

- Wawrzynczak, A., Kopka, P., and Borysiewicz, M.: Sequential Monte Carlo in Bayesian Assessment of Contaminant Source Localization Based on the Sensors Concentration Measurements, in: *Parallel Processing and Applied Mathematics*, edited by Wyrzykowski, R., Dongarra, J., Karczewski, K., and Waśniewski, J., pp. 407–417, Springer Berlin Heidelberg, Berlin, Heidelberg, 2014.
- Webster, H. and Thomson, D.: The NAME wet deposition scheme, URL <https://library.metoffice.gov.uk/Portal/Default/en-GB/RecordView/Index/197129>, 2014.
- Webster, H. N. and Thomson, D. J.: Using Ensemble Meteorological Data Sets to Treat Meteorological Uncertainties in a Bayesian Volcanic Ash Inverse Modeling System: A Case Study, Grímsvötn 2011, *Journal of Geophysical Research: Atmospheres*, 127, e2022JD036469, doi: <https://doi.org/10.1029/2022JD036469>, e2022JD036469 2022JD036469, 2022.
- Wilson, J. D., Flesch, T. K., and Bourdin, P.: Ground-to-air gas emission rate inferred from measured concentration rise within a disturbed atmospheric surface layer, *Journal of Applied Meteorology and Climatology*, 49, 1818–1830, doi: [10.1175/2010jamc2427.1](https://doi.org/10.1175/2010jamc2427.1), 2010.
- Wohltmann, I. and Rex, M.: The Lagrangian chemistry and transport model ATLAS: validation of advective transport and mixing, *Geoscientific Model Development*, 2, 153–173, doi: [10.5194/gmd-2-153-2009](https://doi.org/10.5194/gmd-2-153-2009), 2009.
- Wu, X., Griessbach, S., and Hoffmann, L.: Long-range transport of volcanic aerosol from the 2010 Merapi tropical eruption to Antarctica, *Atmospheric Chemistry and Physics*, 18, 15859–15877, doi: [10.5194/acp-18-15859-2018](https://doi.org/10.5194/acp-18-15859-2018), 2018.
- Wu, X., Griessbach, S., and Hoffmann, L.: Equatorward dispersion of a high-latitude volcanic plume and its relation to the Asian summer monsoon: a case study of the Sarychev eruption in 2009, *Atmospheric Chemistry and Physics*, 17, 13439–13455, doi: [10.5194/acp-17-13439-2017](https://doi.org/10.5194/acp-17-13439-2017), 2017.
- Zou, L., Hoffmann, L., Griessbach, S., Spang, R., and Wang, L.: Empirical evidence for deep convection being a major source of stratospheric ice clouds over North America, *Atmospheric Chemistry and Physics*, 21, 10457–10475, doi: [10.5194/acp-21-10457-2021](https://doi.org/10.5194/acp-21-10457-2021), 2021.

Acknowledgments

As I complete my thesis, I would like to express my gratitude to everyone who has supported, encouraged, and guided me throughout my research journey. First and foremost, I would like to express my deepest gratitude to my supervisor, Dr. Lars Hoffmann. His insightful guidance, patience, and unwavering support have been invaluable at every stage of this project. I would also like to thank Sabine Griebach, Rolf Müller, Felix Plöger and Jens-Uwe Groß for their valuable advice and reliable help. Thanks to Farahnaz Khosrawi for proofreading the thesis and providing feedback.

I would like to thank the faculty members at the SDL Climate Science Group at the Jülich Supercomputing Centre, whose knowledge and encouragement have been instrumental in shaping my academic and personal growth. My sincere thanks go to my lab mates and friends, whose companionship and collaboration have made this challenging journey much more enjoyable and fulfilling.

Special thanks go to my family. Their unconditional support and understanding gave me a solid foundation and motivation to persevere.